**Biomechanics in microbial systems**

—by—

**Rishi Raj Trivedi**

A dissertation submitted in partial fulfillment

of the requirements for the degree of

**Doctor of Philosophy**

**(Biophysics Graduate Program)**

at the

**UNIVERSITY OF WISCONSIN-MADISON**

**2017**

Date of Final Oral Examination: May 5th, 2017

This dissertation is approved by the following members of the Final Oral Committee:

Nicholas L. Abbott, Professor, Chemical and Biological Engineering
Qiang Cui, Professor, Chemistry
Alessandro Senes, Associate Professor, Biochemistry
Saverio E. Spagnolie, Assistant Professor, Mathematics
Douglas B. Weibel, Professor, Biochemistry, Chemistry and Biomedical Engineering

*To my parents and grandparents!*

## Table of Contents

**Acknowledgements**

First, I would like to thank my advisor, Professor Doug Weibel for his constant support and exceptional guidance when needed, throughout my PhD career. Working with Doug has been a remarkable experience, and he made me realize the importance of smart hard work to do something meaningful with our life. I am grateful to him for giving me the freedom to tackle problems on my own, which has definitely made me more independent and a better scientist.

I would like to thank all of the present and former members of the Weibel lab, especially Julia, Matt, John, Ti-Yu and George, who have been great friends and colleagues, and have helped me grow scientifically as well as personally. I would especially like to thank Julia and Matt for being my buddies and best lab-mates than I could've hoped for! Thank you so much supporting me throughout the years when the work was difficult and the days were dark. How can I forget our post-lunch foosball matches together!

Working with whole genome data set could have been a nightmare without John, I am thankful to him for saving me months of data analysis. We have had many great conversations and I hope to have many more in the future. To George, you have been a great mentor and I learnt a lot from you.

I am fortunate to have terrific collaborators throughout the years, especially Dr. Peter Mushenheim who worked with me on liquid crystal projects and contributed significantly to the research presented in this thesis. I would like to thank Professor Saverio Spagnolie for helping me with mathematical modeling to better understand the hydrodynamics of motile bacteria in anisotropic medium. It has been my pleasure to closely interact with Professor Nick Abbott, his

creativity and intellectual insights have significantly improved the quality of my research. Furthermore, I would like to acknowledge my committee members, Professor Qiang Cui and Professor Alessandro Senes for their valuable comments, insight, guidance and critique. I thank the community at the Materials Research Science and Engineering Center (MRSEC) at the University of Wisconsin for supporting my professional development and research.

To all of my friends, you will never be able to understand how much I appreciate your support throughout our lives as well as accepting me for who I am. To Kiran, you have been my vicious critic and great support during tough times, I deeply respect you as a friend. To Varun, you have been the best roommate and true friend in Madison.

If it weren't for all the sacrifices and compromises that my parents made, I would not be here, today. I would like to thank my father, Ravi Prakash Trivedi, and mother, Arti Trivedi for believing in me and providing me all the love and care from such a long distance. Your support has been instrumental in the pursuit of my passion in science. I would like to thank my sister, Anushka Misra for being my rock through life and keeping me strong and positive.

Last but not the least, I want to thank Roshni, for understanding me and standing by me. You have been a yin to my yang and I look forward to spend many-many years together with you!

**Biomechanics in Microbial Systems**

Rishi Raj Trivedi

Under the supervision of Professor Douglas B. Weibel

Department of Biochemistry

At the University of Wisconsin-Madison, Madison WI

Bacteria utilize various physical, chemical, and genetic cues to colonize diverse environments. Environmental sensing mechanisms enable bacteria to adapt their behavior and physiology to cope with fluctuating conditions. Bacteria often experience large forces exerted both by their local microenvironment and from osmotic pressures as high as 25 atmospheres (~25 MPa) across the cell envelope. Bacteria have evolved a thin shell (4-20 nm) of peptidoglycan, which surrounds the cytoplasmic membrane, functioning as an 'exoskeleton' to maintain their mechanical integrity. Peptidoglycan is a macromolecular network of polysaccharides crosslinked with peptide bonds, and one of the most important targets for antibiotics. Thus, understanding its regulation and role in cell stiffness has important connotations for clinical microbiology and medicine.

Despite decades of studies on peptidoglycan, we still know very little about its structure, assembly, and regulation. The first chapter addresses this dearth by describing the application of a unique high-throughput biophysical assay (which we refer to as 'GRABS') to identify genetic modulators of bacterial stiffness using a genome-wide non-redundant transposon mutant library of the opportunistic human pathogen *Pseudomonas aeruginosa*. We discovered a diverse range

of families of proteins that influenced stiffness in *P. aeruginosa.* Our assay. We described the role of D-alanine metabolism in cell stiffness. Further, our assay revealed a potential function in cell stiffness regulation for a number of hypothetical proteins, which are interesting targets for future biochemical and biophysical studies.

In the second half of the dissertation, we explored how an anisotropic and viscoelastic liquid crystal (LC) environment changes the motility behaviors of bacterial cells. We also studied motile bacterial cells at anisotropic LC interfaces to understand the interplay of elasticity-mediated forces, bacterial flagella-derived propulsive forces, surface-induced ordering, and strain induced topological defects in LCs. We demonstrated that motile bacterial cells can transport polymer microparticles and non-motile cells unidirectionally along the far-field director in lyotropic nematic LCs over long ranges. This method of microscale transport suggests new methods for manipulating bacteria in technological contexts and reveals principles for use in design of active materials. Together, these studies cast new light on mechanisms and underlying principles that control bacteria-environment interactions.

# CHAPTER 1

## General Introduction

**Introduction to bacterial cell mechanics**

Bacteria inhabit a variety of environments, and the chemical and mechanical properties of the medium play an important role in bacterial physiology. To maintain cell shape and protect the cell from lysis, most bacteria have evolved a cell envelope that consists of one or two lipid bilayers and a cell wall. The osmotic pressure inside a bacterial cell can be as high as 25 atmospheres, thus maintenance of mechanical integrity is critical to their survival (1, 2). The cell wall is hydrated (~85% of the mass is bound water (3), stiff, viscoelastic, and is the primary load-bearing component of the cell envelope. The cell wall consists of peptidoglycan (PG), a flexible polymer that resists expansion due to turgor pressure (>1 atm; >100 kPa), thereby protecting bacteria from osmotic shock and mechanical stress (1-4).

PG is a widely-conserved material in eubacteria that has the form of a 3D polymeric network and is positioned outside of the cytoplasmic (inner) membrane (Fig. 1). Imaging bacterial structures under near-native conditions at nanometer resolution has facilitated our understanding of PG organization in bacterial cell walls. For example, atomic force microscopy (AFM) of isolated PG fragments demonstrated anisotropy in the *Escherichia coli* cell wall that arises from the arrangement of PG strands oriented orthogonal to the long axis of the rod-shaped sacculi (5), and PG orientation in *Bacillus subtilis* is similar (6). Electron cryotomography has also revealed the PG ultrastructure, wherein a single layer of linked glycan strands encircles the cell in a disorganized hoop-like fashion in isolated, intact sacculi of the *E. coli* and *Caulobacter crescentus* (7). Based on the architecture of their cell envelope, bacteria can be classified into two main cell types: 1) gram-negative cells have an inner and outer membrane and a single thin

PG layer (~4-nm thick) (8); and 2) gram-positive cells have a single cytoplasmic membrane surrounded by a thick PG layer (~30-nm thick) (9).

The PG macromolecule is a mesh consisting of polysaccharide chains cross-linked by peptide bonds. The polysaccharide chain consists of alternating units of N-acetylglucosamine (GlcNAc) and N-acetylmuramic acid (MurNAc) linked by β-1,4 glycosidic bonds. Pentapeptides are covalently attached to a lactyl moiety at the C-3 position of MurNAc (4). In Gram-negative bacteria, the pentapeptide is generally consists of L-Ala-D-Glu- *meso*-diaminopimelic acid-D-Ala-D-Ala (Fig 1). Transpeptidases form cross-linking peptide bonds between adjacent pentapeptides and decorate the polysaccharide backbone (4). The orientation of the peptide bonds makes it possible for the PG to provide mechanical stability by swelling and shrinking with changes in osmotic pressure, while the rigid glycans maintain a constant diameter (10). Peptidoglycan can be characterized as monomeric (no cross-linkage), dimeric (one cross-linkage) or trimeric (two cross-linkages) depending on the number of cross-linkages to a single peptide stem (11). The relative abundance of each cross-linkage species enables determining the crosslinking percentage of the peptidoglycan meshwork, with high degrees of crosslinking indicating greater stiffness (12).

Mechanisms for the synthesis and growth of PG are regulated in a spatial and temporal manner throughout the bacterial life cycle (13). There are three modes of bacterial cell growth: 1) elongation, during which PG is incorporated along the entire cell wall; 2) pre-septal elongation, during which enzymes for the synthesis of PG are recruited to the division ring; and 3) septation,

during which enzymes that break down PG (hydrolases and amidases) are recruited to the division plane and divide the cell (4,13).

Although PG is widely conserved across bacteria, our understanding of its chemical and physical properties is limited to studies of a small number of model organisms, making it unclear how widely spread these characteristics are across eubacteria. Previous studies have explored stiffness properties of PG, which is described by the tensile elasticity of the polymer (5, 14, 15). The Young's modulus (*E*; in units of Pa or $N/m^2$) represents the ratio between the applied stress on the material (force/area) and the resulting strain (change in length/initial length), and is analogous to the force constant describing the restoring force exerted by a stretched spring (5, 14, 15). Two primary techniques have been used to measure *E* for intact fragments of PG and the cell walls of both live and dead bacterial cells: tensile strength measurements and AFM (15-17). Tensile strength measurements require mesoscopic threads of cells encapsulated in exopolysaccharide (i.e., secreted) to be elongated to determine the Young's modulus using a load cell to determine the relationship between stress on the material and strain; an obvious disadvantage to this technique is that most bacterial strains do not form mesoscopic threads and are not compatible with this instrument (15-17).

As a more generally applicable technique, AFM has frequently been used to measure the mechanical and structural properties of the bacterial cell wall. In a typical experiment, cells are immobilized on a surface and imaged using contact or tapping mode AFM, and force curves are measured at various locations on the cell surface. Values of the Young's modulus for several gram-positive and gram-negative bacteria have been determined experimentally by AFM using

force spectroscopy or force-volume mode measurements. However, AFM poses several technical challenges, including large standard deviation in modulus measurements, measurements are limited to probe diameter and do not capture local cell-wall deformations that are larger than the probe diameter (18, 19).

We previously developed a new microscopy-based technique, CLAMP (Cell Length Analysis of Mechanical Properties) to determine bacterial cell stiffness using microscopy-based growth of single cells embedded in agarose hydrogels of tunable mechanical stiffness (20). Using CLAMP, we observed a decrease in bacterial growth concurrent with increasing gel stiffness, which enabled us to estimate Young's modulus of the cell wall ($E_{\text{cell}}$) by matching growth rates in polymers of varying stiffness with a theoretical framework of a finite-element model of the growth of an elastic shell to predict the deformation of thin-shell polymers (21).

To overcome the throughput limitation of the microscopy-based CLAMP method, we developed a mechanical genomics assay, General Regulators Affecting Bacterial Stiffness (GRABS), that enables comparisons of the growth rates of cells in liquid media and cells embedded in agarose gels from measurements of light absorption at $\lambda$=595 nm in 96-well plates using a standard microplate reader (22). This strategy enabled us to rapidly screen a diverse collection of mutants, including genome-wide knockout libraries and point mutations for changes that specifically affect cell growth embedded in agarose and indicate alterations in cell mechanics.

Until recently, PG was considered the primary load-bearing material and cell shape determinant in eubacteria (5). PG is absent in eukaryotes and cytoskeletal proteins such as actin oppose

external loads, define cell shape, and contribute to its mechanical properties (23). It was discovered that the prokaryotic actin homolog, MreB is responsible for determining the rod-shape of bacilli by controlling the incorporation of newly synthesized glycan monomers (24-27). This observation cemented the current view that proteins can play a significant role in determining cell shape and the cell wall strength indirectly by synthesizing, incorporating, and recycling PG building blocks.

In the first part of my thesis, I use the GRABS assay to quantify the individual effects of non-essential proteins on the mechanical properties of the Gram-negative bacterium *Pseudomonas aeruginosa,* a clinically relevant opportunistic pathogen (28). By screening a non-redundant transposon library of gene knockouts in *P. aeruginosa* strain PA14, we identified 42 candidate proteins that alter cell mechanics (29). We demonstrate that deletion of the D-Ala dehydrogenase gene, *dadA* reduces cell stiffness through accumulation of D-Ala. Our experiments show that *P. aeruginosa* Δ*dadA* cells have a stiffness that is 18% lower than *P. aeruginosa* PA14 wild type cells. When we measured the GRABS score of *P. aeruginosa* PA14 wild type and Δ*dadA* transposon mutants in growth media supplemented with D-Ala—that is actively transported into cells—we observed that values of cell stiffness were correlated to D-Ala concentration; higher D-Ala concentrations decreased the GRABS score, characteristic of a reduction in cell stiffness. We describe the interesting connection between regulation of intracellular D-Ala concentration and cell stiffness and discuss applications for future antimicrobial chemotherapies.

Our work demonstrates that bacterial cell stiffness is a property of both the cell wall and broader cell physiology and lays the groundwork for future systematic studies of mechano-regulation in *P. aeruginosa.*

**Introduction to bacterial behavior in anisotropic environments**

Bacteria are exposed to a wide range of physical microenvironments with different properties that can impact their motility and viability (30). Many of these habitats have uniform physical properties; i.e. they are isotropic in nature, and suspended non-motile bacterial cells display a characteristic Brownian motion, as the viscoelastic properties of the liquid are same in all directions. While many bacteria commonly inhabit isotropic microenvironments, some specialized bacteria including *Staphylococcus aureus*, *Neisseria gonorrhoeae*, β-hemolytic strains of *Streptococcus*, *Mycobacterium tuberculosis*, and *Pseudomonas aeruginosa* are known to colonize anisotropic environments such as collagen, cellulose, chitin, synovial fluid, the matrix of extracellular polymeric substances associated with bacterial biofilms, and insect exoskeletons, which show direction-dependent optical, mechanical, and diffusion properties (31-34). To date, the study of bacterial motility has been largely confined to the analysis of cells dispersed in isotropic environments while cell behavior within environments exhibiting anisotropic viscoelastic properties (such as those described above) remains relatively unexplored. To understand the behavior of the bacteria in anisotropic media, we created synthetic liquid crystal (LC) based microenvironments that have direction-dependent physical properties that are manipulated easily and with high precision.

Liquid crystals (LC) are a thermodynamic stable phase possessing properties between liquids and solids. LCs are characterized by long-range orientational and positional order without the existence of a three-dimensional crystal lattice; mesogens in the LC phase flow like in liquid but retain some degree of alignment (Fig. 2). LCs encompass a state of soft matter in which properties are typically anisotropic (35). Unlike isotropic liquids, LCs exhibit elasticity that

enables energy to be stored at rest in strained states, and they form topological defects in confined systems. LCs can be divided into two broad categories: thermotropic and lyotropic. Thermotropics consist of small organic molecules that exhibit temperature dependent phase behaviors and are commonly used in liquid crystal display (LCD) technologies. Lyotropics are amphiphilic mesogens that can be dissolved in water and exhibit phase behavior dictated by both temperature and concentration. Depending upon the amount of order in the material, both thermotropic and lyotropic chromonic LCs can form nematic phase LCs, which are characterized by molecules that have a long-range direction of alignment defined as the director. Nematic LCs have anisotropic viscoelastic properties that can be influenced by surface-induced ordering of the mesogens and strain in the LC. Nematic LCs can be differentiated based on their optical properties (birefriengence) and by dielectric and diamagnetic anisotropy (35-37).

Recent studies of micrometer-sized synthetic particles (e.g., polystyrene or silica) have revealed that the anisotropic viscoelasticity of LCs can generate direction-dependent inter-particle forces that form complex, self-assembled structures (38-41). Although the self-organization of 'passive' colloids in LCs has been well characterized, much less is known about the behaviors of 'active' particles (7, 8) that propel themselves within LCs (42, 43). Smalyukh *et al*. suspended the rod-shaped bacterium *Pseudomonas aeruginosa* within a matrix of concentrated, directionally aligned DNA that exhibits nematic LC-like properties and reported alignment of the long axis of *P. aeruginosa* cells parallel to the LC director, as well as biased motility of the bacteria in this direction (44). The authors also reported that the bacterial surface appears to anchor LCs tangentially. Thus, the authors claim that the anisotropic alignment and motility of the *P.*

*aeruginosa* cells result from a drive to minimize elastic distortions within the nematic-like DNA matrix.

Recently, Kumar *et al.* reported an investigation of the motility of *Escherichia coli* cells in a lyotropic LC solution of disodium chromoglycate (DSCG) (Fig. 2). This particular LC was chosen due to its low toxicity to cells and microorganisms. They found that *E. coli* cells exhibited motility indicative of a Brownian motion when suspended within the isotropic phase of the LC; within the nematic LC phase, the bacterial cells instead moved uniformly in a direction parallel to the nematic director (45). The authors suggested that the anisotropic motion of the bacteria in the nematic LC phase arises due to elastic interactions with the LC.

However, the mechanism by which the anisotropy of these LC environments influences dynamic behaviors of bacteria remains poorly understood beyond observations of anisotropic orientation and motion. We extend these studies by characterizing the behavior of *Proteus mirabilis* cells within aqueous DSCG (15 wt%) in aqueous motility buffer. *P. mirabilis* is a gram-negative, rod-shaped gamma-proteobacterium that is commonly associated with urinary tract infections and the biofouling of catheters. *P. mirabilis* differentiates into elongated ‘swarmer’ cells with high densities of flagella, enabling it to retain motility in environments with high viscoelasticity.

In the second part of the thesis, I address key issues such as the influence of elastic and motive forces on the self-organization of bacteria, both within the bulk of a LC and at interfaces formed between nematic and isotropic phases (46). I also explore how the presence of topological defects in LCs can influence the dynamic behaviors of bacteria and how interactions of motile

bacteria with regions of LC that undergo spatial variation in orientation can guide complex cellular trajectories. The interplay of flagella-derived propulsive forces and LC elasticity forces gives rise to preferential motion of the bacteria adsorbed to the nematic-isotropic interface and also leads to formation of reversible linear assemblies of cells (47). I observed that bacteria escape their association with the nematic-isotropic interface using flagella-derived forces and that escape events, particularly in the case when cells exit into the bulk nematic phase, occur preferentially at topological defects at the interface. Based on these results, I demonstrate that by altering the geometry of the nematic-isotropic interface, the ability of bacteria to escape adsorption can be limited. It is likely that this approach could provide the basis of a novel method to locally concentrate cells. Finally, my observations provide unique insight into the manner in which elastic forces may influence the dynamics and organization of bacteria at interfaces between isotropic and anisotropic biological microenvironments.

The fundamental insights developed in these studies suggest methods and approaches for the manipulation of bacteria in ways that are not possible in isotropic fluids and I describe the controlled transport and delivery of microscale objects by motile bacteria suspended in nematic LC phases of DSCG (48).

**Fig. 1**

**Organization of the cell envelope in bacteria.**

A) A cartoon depicting the structure of the bacterial cell wall in gram-positive and gram-negative bacteria. B) Differences in peptidoglycan structural organization and composition of gram-positive and gram-negative bacteria.

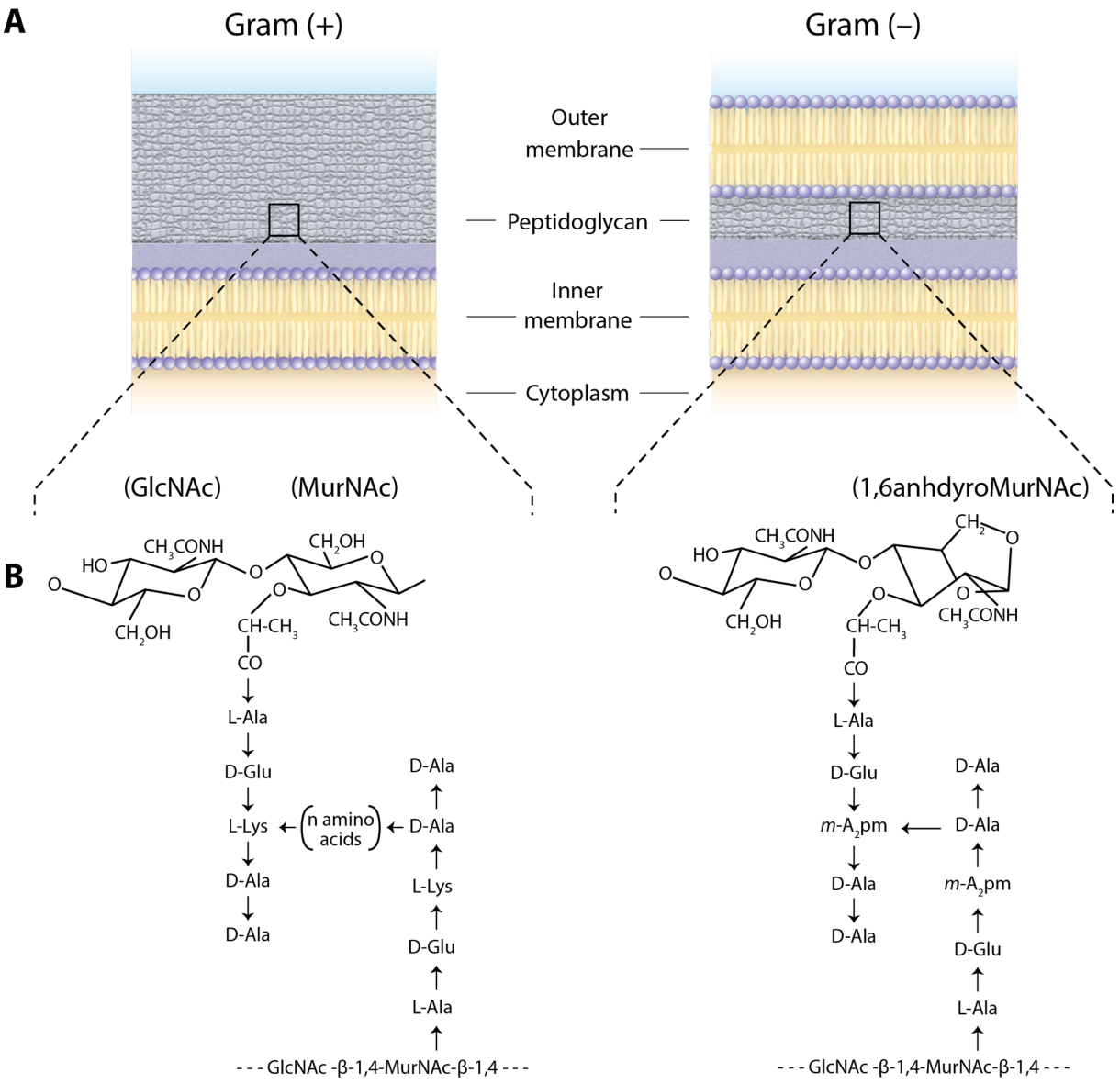


**Fig. 1**

**Fig. 2. Introduction to liquid crystals.**

A) Schematic depiction of the phase behavior of a molecule that exhibits a thermostropic or lyotropic nematic liquid crystal phase. (B) Molecular structure of disodium cromoglycate (DSCG).

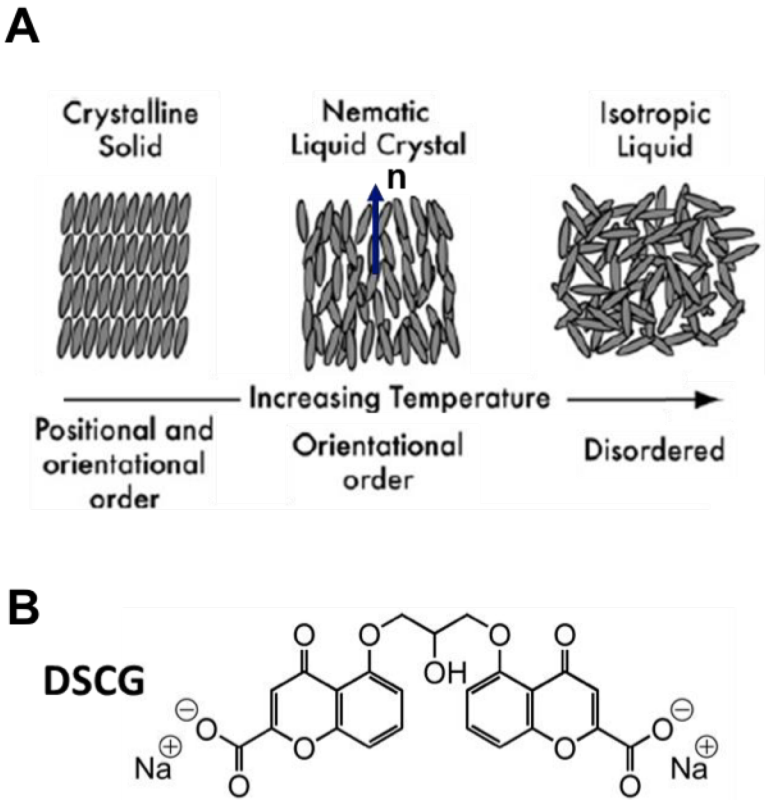


**Fig. 2**

**References**


1. Höltje, J.V., 1998. Growth of the stress-bearing and shape-maintaining murein sacculus of Escherichia coli. *Microbiology and Molecular Biology Reviews*, *62*(1), pp.181-203.

2. Walsh, Christopher. "Antibiotics: actions, origins, resistance." (2003).

3. Hobot, J.A., Carlemalm, E.R.I.C., Villiger, W. and Kellenberger, E.D.W.A.R.D., 1984. Periplasmic gel: new concept resulting from the reinvestigation of bacterial cell envelope ultrastructure by new methods. *Journal of Bacteriology*, *160*(1), pp.143-152.

4. Vollmer, W. and Bertsche, U., 2008. Murein (peptidoglycan) structure, architecture and biosynthesis in Escherichia coli. *Biochimica et Biophysica Acta (BBA)-Biomembranes*, *1778*(9), pp.1714-1734.

5. Yao, X., Jericho, M., Pink, D. and Beveridge, T., 1999. Thickness and elasticity of gram-negative murein sacculi measured by atomic force microscopy. *Journal of bacteriology*, *181*(22), pp.6865-6875.

6. Hayhurst, E.J., Kailas, L., Hobbs, J.K. and Foster, S.J., 2008. Cell wall peptidoglycan architecture in Bacillus subtilis. *Proceedings of the National Academy of Sciences*, *105*(38), pp.14603-14608.

7. Gan, L., Chen, S. and Jensen, G.J., 2008. Molecular organization of Gram-negative peptidoglycan. *Proceedings of the National Academy of Sciences*, *105*(48), pp.18953-18957.

8. Matias, V.R., Al-Amoudi, A., Dubochet, J. and Beveridge, T.J., 2003. Cryo-transmission electron microscopy of frozen-hydrated sections of Escherichia coli and Pseudomonas aeruginosa. *Journal of Bacteriology*, *185*(20), pp.6112-6118.

9. Matias, V.R. and Beveridge, T.J., 2005. Cryo-electron microscopy reveals native polymeric cell wall structure in Bacillus subtilis 168 and the existence of a periplasmic space. *Molecular microbiology*, *56*(1), pp.240-251.

10. Van Den Bogaart, G., Hermans, N., Krasnikov, V. and Poolman, B., 2007. Protein mobility and diffusive barriers in Escherichia coli: consequences of osmotic stress. *Molecular microbiology*, *64*(3), pp.858-871.

11. Glauner B (1988) Separation and Quantification of Muropeptides with High-Performance Liquid-Chromatography. *Anal Biochem* 172(2):451-464.

12. Desmarais, S.M., De Pedro, M.A., Cava, F. and Huang, K.C., 2013. Peptidoglycan at its peaks: how chromatographic analyses can reveal bacterial cell wall structure and assembly. *Molecular microbiology*, *89*(1), pp.1-13.

13. Typas, A., Banzhaf, M., Gross, C.A. and Vollmer, W., 2012. From the regulation of peptidoglycan synthesis to bacterial growth and morphology. *Nature Reviews Microbiology*, *10*(2), pp.123-136.

14. Thwaites JJ & Mendelson NH (1985) Biomechanics of Bacterial Walls - Studies of Bacterial Thread Made from Bacillus-Subtilis. *P Natl Acad Sci USA* 82(7):2163-2167.

15. Thwaites JJ, Surana UC, & Jones AM (1991) Mechanical-Properties of Bacillus-Subtilis Cell-Walls - Effects of Ions and Lysozyme. *J Bacteriol* 173(1):204-210.

16. Thwaites, J.J. and Mendelson, N.H., 1989. Mechanical properties of peptidoglycan as determined from bacterial thread. *International journal of biological macromolecules*, *11*(4), pp.201-206.

17. Thwaites, J.J. and Mendelson, N.H., 1991. Mechanical behaviour of bacterial cell walls. *Advances in microbial physiology*, *32*, pp.173-222.

18. Abu-Lail, N.I. and Camesano, T.A., 2006. The effect of solvent polarity on the molecular surface properties and adhesion of Escherichia coli. *Colloids and Surfaces B: Biointerfaces*, *51*(1), pp.62-70.

19. Vadillo-Rodriguez, V., Beveridge, T. J., and Dutcher, J. R. (2008) Surface viscoelasticity of individual Gram-negative bacterial cells measured using atomic force microscopy, *J. Bacteriol. 190*, 4225-4232

20. Tuson, H.H., Auer, G.K., Renner, L.D., Hasebe, M., Tropini, C., Salick, M., Crone, W.C., Gopinathan, A., Huang, K.C. and Weibel, D.B., 2012. Measuring the stiffness of bacterial cells from growth rates in hydrogels of tunable elasticity. *Molecular microbiology*, *84*(5), pp.874-891.

21. Zienkiewicz, O.C. and Taylor, R.L., 2005. *The finite element method for solid and structural mechanics*. Butterworth-heinemann.

22. Auer, G.K., Lee, T.K., Rajendram, M., Cesar, S., Miguel, A., Huang, K.C. and Weibel, D.B., 2016. Mechanical genomics identifies diverse modulators of bacterial cell stiffness. *Cell Systems*, *2*(6), pp.402-411.

23. Janmey, P.A. and McCulloch, C.A., 2007. Cell mechanics: integrating cell responses to mechanical stimuli. *Annu. Rev. Biomed. Eng.*, *9*, pp.1-34.

24. van den Ent, F., Amos, L.A. and LoÈwe, J., 2001. Prokaryotic origin of the actin cytoskeleton. *Nature*, *413*(6851), pp.39-44.

25. Gitai, Z., Dye, N. and Shapiro, L., 2004. An actin-like gene can determine cell polarity in bacteria. *Proceedings of the National Academy of Sciences of the United States of America*, *101*(23), pp.8643-8648.

26. Garner, E.C., Bernard, R., Wang, W., Zhuang, X., Rudner, D.Z. and Mitchison, T., 2011. Coupled, circumferential motions of the cell wall synthesis machinery and MreB filaments in B. subtilis. *Science*, *333*(6039), pp.222-225.

27. Van Teeffelen, S., Wang, S., Furchtgott, L., Huang, K.C., Wingreen, N.S., Shaevitz, J.W. and Gitai, Z., 2011. The bacterial actin MreB rotates, and rotation depends on cell-wall assembly. *Proceedings of the National Academy of Sciences*, *108*(38), pp.15822-15827.

28. Lee, D.G., Urbach, J.M., Wu, G., Liberati, N.T., Feinbaum, R.L., Miyata, S., Diggins, L.T., He, J., Saucier, M., Déziel, E. and Friedman, L., 2006. Genomic analysis reveals that Pseudomonas aeruginosa virulence is combinatorial. *Genome biology*, *7*(10), p.R90.

29. Liberati, N.T., Urbach, J.M., Miyata, S., Lee, D.G., Drenkard, E., Wu, G., Villanueva, J., Wei, T. and Ausubel, F.M., 2006. An ordered, nonredundant library of Pseudomonas aeruginosa strain PA14 transposon insertion mutants. *Proceedings of the National Academy of Sciences of the United States of America*, *103*(8), pp.2833-2838.

30. Fontes, D.E., Mills, A.L., Hornberger, G.M. and Herman, J.S., 1991. Physical and chemical factors influencing transport of microorganisms through porous media. *Applied and Environmental Microbiology*, *57*(9), pp.2473-2481.

31. Shaw, T., Winston, M., Rupp, C.J., Klapper, I. and Stoodley, P., 2004. Commonality of elastic relaxation times in biofilms. *Physical Review Letters*, *93*(9), p.098102.

32. Kasper, D., Fauci, A., Hauser, S., Longo, D., Jameson, J. and Loscalzo, J., 2015. *Harrison's principles of internal medicine, 19e*. Mcgraw-hill.

33. Flemming, H.C. and Wingender, J., 2010. The biofilm matrix. *Nature Reviews Microbiology*, *8*(9), pp.623-633.

34. Rey, A.D., 2010. Liquid crystal models of biological materials and processes. *Soft Matter*, *6*(15), pp.3402-3429.

35. Prost, J., 1995. *The physics of liquid crystals* (No. 83). Oxford university press.

36. Chandrasekhar, S. Liquid Crystals; Cambridge University Press: Cambridge, 1977.

37. Collings, P.J. and Hird, M., 1997. *Introduction to liquid crystals: chemistry and physics*. CRC Press.

38. Lapointe, C., Hultgren, A., Silevitch, D.M., Felton, E.J., Reich, D.H. and Leheny, R.L., 2004. Elastic torque and the levitation of metal wires by a nematic liquid crystal. *Science*, *303*(5658), pp.652-655.

39. Tkalec, U., Škarabot, M. and Muševič, I., 2008. Interactions of micro-rods in a thin layer of a nematic liquid crystal. *Soft matter*, *4*(12), pp.2402-2409.

40. Muševič, I., Škarabot, M., Tkalec, U., Ravnik, M. and Žumer, S., 2006. Two-dimensional nematic colloidal crystals self-assembled by topological defects. *Science*, *313*(5789), pp.954-958.

41. Poulin, P., Stark, H., Lubensky, T.C. and Weitz, D.A., 1997. Novel colloidal interactions in anisotropic fluids. *Science*, *275*(5307), pp.1770-1773.

42. Škarabot, M., Ravnik, M., Žumer, S., Tkalec, U., Poberaj, I., Babič, D., Osterman, N. and Muševič, I., 2008. Interactions of quadrupolar nematic colloids. *Physical Review E*, *77*(3), p.031705.

43. Paxton, W.F., Kistler, K.C., Olmeda, C.C., Sen, A., St. Angelo, S.K., Cao, Y., Mallouk, T.E., Lammert, P.E. and Crespi, V.H., 2004. Catalytic nanomotors: autonomous movement of striped nanorods. *Journal of the American Chemical Society*, *126*(41), pp.13424-13431.

44. Smalyukh, I.I., Butler, J., Shrout, J.D., Parsek, M.R. and Wong, G.C., 2008. Elasticity-mediated nematiclike bacterial organization in model extracellular DNA matrix. *Physical Review E*, *78*(3), p.030701.

45. Kumar, A., Galstian, T., Pattanayek, S.K. and Rainville, S., 2013. The motility of bacteria in an anisotropic liquid environment. *Molecular Crystals and Liquid Crystals*, *574*(1), pp.33-39.

46. Mushenheim, P.C., Trivedi, R.R., Tuson, H.H., Weibel, D.B. and Abbott, N.L., 2014. Dynamic self-assembly of motile bacteria in liquid crystals. *Soft Matter*, *10*(1), pp.88-95.

47. Mushenheim, P.C., Trivedi, R.R., Weibel, D.B. and Abbott, N.L., 2014. Using liquid crystals to reveal how mechanical anisotropy changes interfacial behaviors of motile bacteria. *Biophysical journal*, *107*(1), pp.255-265.

48. Trivedi, R.R., Maeda, R., Abbott, N.L., Spagnolie, S.E. and Weibel, D.B., 2015. Bacterial transport of colloids in liquid crystalline environments. *Soft matter*, *11*(43), pp.8404-8408.

# CHAPTER 2

## Mechanical genomics reveals the role of D-alanine metabolism in *Pseudomonas aeruginosa* cell stiffness

**Abstract**

Bacterial cell stiffness is a key characteristic for resisting the large osmotic pressure differential across the cell wall. Although some of the most successful antibacterial approaches disrupt the mechanical properties of cells, understanding the contribution of genes to bacterial cell stiffness is a parameter of bacterial physiology that has not been determined on a large scale.

We used a high-throughput methodology, general regulators of affecting bacterial stiffness (GRABS) assay to study the contribution of 5790 non-essential genes in the *P. aeruginosa* genome to cell stiffness. *P. aeruginosa* is an opportunistic human pathogen and is naturally resistant to multiple different families of antibiotics. Using GRABS methodology, we identified 42 genes with diverse functionalities that when deleted individually caused a significant decrease in cell stiffness. Our mechanical genomics study also helped assign stiffness function to 6 genes with previously unknown function. We also used a microfluidic-based bending assay to measure the bending rigidity and Young's modulus of bacterial cells to compare the stiffness change upon gene deletion. Our results highlight the fact that proteins with diverse functionalities alter bacterial cell stiffness, and by quantifying these interactions we are able to build a "mechanical genome" of *P. aeruginosa*.

We further extended our study to investigate the role of D-Alanine dehydrogenase enzyme, DadA in regulating mechanical properties of *P. aeruginosa* PA14 cells. We established that deletion of *dadA* leads to an imbalance of D-Ala concentration in the cell. Higher D-Ala levels in the *dadA* mutant reduce cell stiffness by downregulating the expression of genes in the peptidoglycan (PG) synthesis pathway. Our ultra performance liquid chromatography-mass spectrometry based analysis revealed that *dadA* mutants have lower PG crosslinking density and the overall composition of PG is altered compared to *P. aeruginosa* wild type cells.

**Introduction**

Bacterial cells live in hostile environments and require physical protection for survival. pressures (5-6 atmospheres for *Escherichia coli* and 20-25 atmospheres for *Staphylococcus aureus* that change with fluctuations in the molecular composition of extracellular environments[1, 2]. Bacterial cells live in rapidly flowing fluids, the corrosive environments of digestive organs, within deep thermal vents (>350 °C), survive the pressure and peristalsis of blood capillaries and arteries, and endure cycles of freezing and thawing[3-7]. A stiff cell wall (Young's modulus of ~25-100 mPa [8]) is a key structure for surviving many of these conditions and a hallmark of most bacterial genera with very few exceptions (e.g., mycoplasmas and L-forms)[9]. The peptidoglycan layer of the cell wall is the canonical example of a stiff material in bacteria and forms an exoskeleton-like structure that protects cells. With very few exceptions, almost everything known about the chemical and biological elements of bacteria that contribute to cell stiffness connects back to the peptidoglycan layer within the cell envelope and changes in its structure [10, 11].

The peptidoglycan consists of linear polysaccharide chains—composed of alternating N-acetylglucosamine (GlcNAc) and N-acetylmuramic acid (MurNAc) residues—cross-linked by short peptides (Fig. 1). A D-lactoyl group positioned at the C-3 position on each NAM residue is attached to a stem peptide with the common amino acid sequence L-Ala-D-Glu-meso-Dap (or L-Lys)-D-Ala-D-Ala; meso-Dap refers to meso-diaminopimelic acid[12, 13]. Two D-Ala residues at the fourth and fifth positions are a universal feature of the peptide stem of uncrosslinked peptidoglycan[12, 13]. The terminal D-Ala is cleaved off after peptides are cross-linked and is transported into the cell and recycled[14]. D-Ala is the most abundant D-amino acid in bacteria

and is exclusively incorporated into the peptidoglycan[14]. A unique feature of D-amino acids is their resistance to enzymatic processing, which presumably protects the peptidoglycan from degradation by proteases that have broad-spectrum activity[15].

Glycosyltransferases polymerize glycan chains and DD-transpeptidases crosslink stem peptides during peptidoglycan biosynthesis. Class A penicillin-binding proteins (PBPs) are bifunctional enzymes with both glycosyltransferase and transpeptidase activity, whereas class B PBPs are mono-functional transpeptidases. Cross-linking of the glycan strands in peptidoglycan generally occurs between the carboxyl group of D-Ala at position 4 of the stem peptide and the amino group of the meso-Dap on the peptide of an adjacent glycan strand; as bond formation proceeds, the terminal D-Ala is released[12, 13]. Although many of the enzymes involved in peptidoglycan biosynthesis have been identified in the most commonly studied model bacteria, a characterization of their function in cells is slowly emerging. For example, a recent genome-wide method for studying bacterial stiffness demonstrated that PBP1a and PBP1b—previously assigned to be interchangeable and have redundant function—have remarkably different contributions to cell stiffness[16]. A number of studies highlight that there is still much to be learned regarding peptidoglycan biosynthesis in bacterial cells[13, 17].

Antibiotics targeting components of the peptidoglycan biosynthesis machinery disrupt the mechanical integrity of the cell and promote lysis. For example, fosfomycin inhibits biosynthesis of cell-wall precursors and vancomycin, ramoplanin, and teicoplanin inhibit transglycosylase activity during peptidoglycan chain elongation[1, 10, 18, 19]. Amoxicillin, ampicillin, penicillin G, faropenem, cefixime, and aztreonam prevent amide bond formation between adjacent

pentapeptides by inhibiting transpeptidase activity of various PBPs and cause cell lysis[10, 19-23]. As the peptidoglycan is one of the most important targets for antibiotics, uncovering its biochemical regulation and role in stiffness marking this area of research as potentially important for clinical microbiology and medicine. From a broader perspective, a general understanding of bacterial cell mechanics is still lacking and would benefit from: 1) identification of regulators and factors that control peptidoglycan biosynthesis; 2) a mechanistic understanding of cell wall assembly in space and time; and 3) the identification and studying of proteins and materials—beyond the peptidoglycan—that contribute to cell stiffness.

Very few bacteria have been the focus of cell mechanics studies to-date. Among those that have largely evaded studies, *Pseudomonas aeruginosa* is a model bacterium that is clinically relevant and difficult to treat using chemotherapies[24, 25]. *P. aeruginosa* is notoriously resistant to different families of antibiotics—including low susceptibility to beta-lactams, aminoglycosides, and quinolones—due to an extensive drug efflux system that reduces the concentration of antibiotics intracellularly and cell susceptibility[24, 25]. A limited understanding of the function of many of its genes provides this bacterium with an advantage in evading antibiotic chemotherapies. The genome of multiple *P. aeruginosa* strains have been sequenced, however only 20% of the 5973 predicted genes in *P. aeruginosa* strain PA14 have an assigned function[26], making it an interesting organism in which to build connections between genes and cell stiffness, close the biochemical gap among genes of unknown function, and potentially reveal new targets for developing antibiotic strategies.

We performed a genome-wide cell mechanics screen in *P. aeruginosa* to identify and study biochemical elements that control cell mechanics and explore opportunities to alter cell mechanical properties. By screening a non-redundant transposon library of gene knockouts in *P. aeruginosa* strain PA14, we identified 43 candidate proteins that significantly altered cell mechanics[27]. Of those proteins, our studies illuminated the role of D-Ala in cell stiffness and the detrimental effect of its accumulation in *P. aeruginosa* cells, suggesting an uncharacterized biochemical network in cells and a potential Achilles heal to exploit in chemotherapies.

## Materials and Methods

### Strain and plasmid construction.

Screening was performed using the non-redundant transposon mutant library of P. aeruginosa strain PA14 consisting of 5,790 transposon mutants[27].

**Growth of bacterial cultures for screening.** Individual 2-mL cultures were inoculated from a freezer stock and grown overnight in lysogeny broth (LB) at 37 °C with shaking until saturation (~16 h). Since transposon has gentamycin resistance cassette, mutants were grown in the presence of 15 μg/mL gentamycin for selection of the transposon mutant in the overnight culture. Strains containing plasmid pUCP18 were grown overnight in 100 μg/mL ampicillin and 100μg/mL gentamycin, respectively[28].

**Preparation of GRABS 96-well plates.** To prepare GRABS 96-well plate, we used previously published GRABS protocol (Ref). Briefly, absorbance ($\lambda$ = 595 nm) of saturated overnight cultures for different mutant strains were measured and cells were harvested at 1000 x *g* for 10 min to give final absorbance of 0.32. 48 microstirrers (V&P Scientific, San Diego, CA, USA) were washed with 70% ethanol and placed into individual wells of first 6 columns of a 96-well microplate (Corning) and the microplate was sterilized with ultraviolet light for 20 min before transferring to a 50 °C hotplate to warm the plate and magnets. To prepare the final plate for growth-curve measurements, we pipetted 150 μL LB into the wells in last 6 columns (7-12 columns) and let the LB warm for 20 min. 1% UltraPure agarose solution was prepared by dissolving 0.2 g agarose in 20 mL LB until solution was visually homogeneous. Using a positive displacement pipette, we added 150 μL of 1% agarose solution from a 2.5-mL tip into each well

that contained a magnetic stirrer and stirrered for ~10 s. The microplate was transferred to a second hotplate set to 37 °C and cooled for 15-20 s. We aliquoted 5 μL of each cell suspension using a multichannel pipette into one well with LB and one well with agarose prepolymer to yield an OD 0.01 and mixed the cultures with magnetic stirrers for ~10 s.

We extracted magnetic stirrers by using another magnet and quickly removed any bubbles on the surface of the agarose gel with a sterile pipette tip. Once the agarose got solidified, we sealed the 96-well GRABS plate with a transparent polymer film. Finally, we placed the microplate into a preheated 37 °C M1000 Tecan plate reader and recorded absorbance at 595 nm at 37 °C. We used 30 s duration for orbital and linear shaking, and the plates were shaken at 2 mm amplitude. Readings were taken for 16 h at 5-min intervals and i-control v. 1.9.17.0 software (Tecan) was used to collect and export data from the plate reader for further analysis.

**GRABS data analysis**.

Growth data were collected over 16 h for PA14 transposon mutants in both agarose and liquid medium. To reduce the growth curve to a scalar value, we first normalized the growth data in liquid and agarose by subtracting the minimum absorbance reading (in agarose and liquid) for each mutant. We determined growth saturation point of *P. aeruginosa* wild type using a custom MATLAB script. The growth curve data was first smoothed due to optical stability issues of the instrument (Tecan M1000) and absorbance for blank sample measured by the instrument was subtracted from all the traces. To smooth the data, we utilized a moving average algorithm with a window size of 20 data points. To determine the time of bacteria growth saturation, we looked at the slope of the smoothed absorbance curve as the curve approaches saturation. We introduced a threshold on the slope to determine the first point at which the bacteria reach saturation. We set

the threshold value at $5 \times 10^{-6}$. If the slope never dips below this value, we exclude that curve from consideration. Based on the moving average algorithm, we decided to take the average of 7 data points at 12 h, which is approximately when PA14 wild type cells begin to enter stationary phase in liquid medium. We also used 12 h time points to calculate absorbance for cells embedded in 1% agarose as it provided the largest dynamic range of values to compare.

We measured the growth of cells of each mutant strain against wild type *P. aeruginosa* PA14 encapsulated in liquid lysogeny broth (LB) nutrient media and in 1% agarose gels (infused with LB nutrient media). We first normalized the absorbance (λ=595 nm) value of wild type PA14 cells grown in liquid LB and in 1% agarose and used this data to determine a percent growth value for each mutant compared to wild type cells. We determined a relative stiffness score—we refer to as a GRABS score[16]—for all mutant strains against wild type PA14 using the following equation:

$$GRABS\ score = 100 \times \left( \frac{OD_{mutant,\ agarose}}{OD_{wild\ type,\ agarose}} - \frac{OD_{mutant,\ LB}}{OD_{wild\ type,\ LB}} \right)$$

A positive GRABS score for a mutant indicates that if wild type and mutant cells grow at the same rate in liquid LB, cells of the mutant grow faster in 1% agarose than wild type cells. Based on our past experiments, mutants with a positive GRABS score indicate cells have increased stiffness. A negative GRABS score for a mutant indicates cells with reduced stiffness (compared to wild type cells) for which mutant cells grows more slowly in 1% agarose than wild type cells (again, when the growth of both wild type and mutant in liquid LB as similar).

For our screen in LB medium supplemented with D-Ala, we normalized all mutant data to an average of several wild type control growth curves in liquid and agarose infused with plain LB. We used multiple wild-type control on each plate to normalize the data.

**Complementation and deletion assays for *dadA* mutants.**

We acquired *dadA::*Tn mutant strain complemented with pDadAX plasmid from Marvin Whiteley lab[28]. pDadAX plasmid was constructed using pUCP18 vector, which allows constitutive expression of *dadA* from the lac operon promoter. We also used PA14 wild type/pUCP18 and *dadA::*Tn/pUCP18 strains as empty vector control for GRABS measurements. Briefly, we streaked out strains complemented with different plasmids onto LB agar plates with appropriate antibiotics to obtain individual colonies. Individual colonies were inoculated into 2 mL LB with appropriate antibiotics and grown overnight at 37 °C. GRABS 96-well plates were prepared as described above. For complementation assays, we did not add antibiotics so as to not influence the growth of the cells.

**Microfluidic-based stiffness measurements.** *P. aeruginosa* PA14 wild type, *dadA*::Tn and *dadA*::Tn/pDadAX strains were grown overnight in 2 mL LB containing appropriate antibiotics. We determined cellular bending rigidity and Young's modulus by deflecting filamented wild type and mutant strains using a fabricated microfluidic device as described previously [29]. We used 1 μg/mL aztreonam to filament both *P. aeruginosa* PA14 wild type and *dadA::* Tn cells, and absorbance (λ=600 nm) of filamented cells was normalized to 1 before loading into individual channels of the microfluidic to monitor deflection under fluid flow. Images were collected using a Zeiss Axiovert 100 microscope equipped with a 63X oil objective equipped

with an Andor iXon 3 EMCCD. Deflection of the cells was determined using a custom Igor Pro (WaveMetrics Inc.) image analysis algorithm and bending rigidity values were obtained via curve fitting.

To account for changes in the diameter of mutant cells compared to wild-type cells after filamentation, we collected static images with a 100X oil objective on a Nikon Eclipse Ti inverted microscope equipped with a CoolSNAP HQ2 camera. Cell width was measured using imageJ. These measurements were used to calculate the Young's modulus from the flexural rigidity, in which the moment of inertia ($I$) of a cross-section is dependent on cell radius ($r$) and thickness of the cell wall ($h$) according to $I = \pi r^3 h$.

**Quantitative polymerase chain reaction.** The Zymo Research Direct-zol RNA Miniprep kit was used to extract total RNA. Genomic DNA was removed using the ArcticZymes HL-dsDNase, and RNA was reverse transcribed using the Applied Biosystems High Capacity RNA-to-cDNA kit. Newly synthesized cDNA was treated with New England Biolabs RNase H to digest RNA hybridized to cDNA. The Thermo Fisher PowerUp SYBR Green Master mix was used for quantitative PCR on an Applied Biosystems 7500 Fast real-time PCR system, following the manufacturer's instructions for a standard cycling protocol. Primers for *rpsl* were used as endogenous controls.

**Purification of sacculi and ultra performance liquid chromatography (UPLC) of peptidoglycan composition.** Overnight cultures of *P. aeruginosa* PA14 wild type and *dadA* transposon mutants corresponding to $OD_{600}$ 100 were harvested by centrifugation at 5,000 × *g*

for 10 min at room temperature and resuspended in 3 mL LB. Cells were lysed with a tip sonicator (Qsonica) two times for ~15s and 10s each at a power setting of 75. Boiling sodium dodecyl sulfate (SDS) was added to cell suspensions, and stirred at 500 rpm for 3 hours to mix the cell suspensions and SDS. Insoluble material was collected by several rounds of ultracentrifugation at 400,000 × *g* for 20 min at room temperature. Samples were prepared for UPLC as previously described [30] and injected onto a Waters H Class UPLC system equipped with a BEH C18 1.7-µm column (Waters, MA, USA), using elution conditions previously described [31]. Peaks were quantified and identified as per the table and from which the crosslinking density and strand length were calculated [32, 33].

## Results and Discussion

### Amino acid metabolism genes are enriched in a genome-wide screen of *P. aeruginosa* PA14 cell stiffness

We used a reproducible and high-throughput assay (general regulators affecting bacterial stiffness, GRABS) to identify *P. aeruginosa* cells with altered stiffness from a library of transposon mutants [16]. We screened a non-redundant transposon mutant library of *P. aeruginosa* strain PA14 consisting of 5,790 clones covering ~80% of the non-essential PA14 ORFs to identify mutants with altered cell stiffness[27]. These mutants have been constructed using a mariner-based transposon MAR2xT7, which contains a gentamycin resistance. We measured the growth of cells of each mutant strain against wild type *P. aeruginosa* PA14 in liquid lysogeny broth (LB) nutrient media and encapsulated in 1% agarose gels infused with LB. We normalized the absorbance ($\lambda$=595 nm) value of wild type PA14 cells grown in liquid LB and in 1% agarose and used this data to determine a percent growth value for each mutant compared to wild type cells. We determined a relative stiffness score—referred to as a GRABS score[16]—for all mutant strains against wild type PA14.

For wild type and mutant cells growing at the same rate in liquid LB, a positive GRABS indicates a mutant growing faster in 1% agarose than wild type cells. Based on our past experiments, mutants with a positive GRABS score are indicative of increased stiffness. A negative GRABS score for a mutant indicates cells with reduced stiffness and growth in 1% agarose that is slower than wild type cells (again, when the growth of both wild type and mutant in liquid LB as similar). *P. aeruginosa* PA14 mutants with high or low scores revealed genes coding for proteins that are likely to play a role in cell stiffness.

Fig. 2A displays a scatter plot of every gene in the library, time dependent absorbance measurements for mutants growing in LB (λ=595 nm), and for mutants encapsulated and growing in 1% agarose infused with LB. From an analysis of the distribution of absorbance measurements (λ=595 nm) of mutants in LB and in agarose, we found that absorbance is approximately normally distributed and centered at a value of 0.67 in LB and at 0.27 in 1% agarose. Of the 5,728 mutants we studied, 35 mutants did not grow in LB and 1% agarose and we excluded them from our analysis, which reduced the number of genes in the data set to 5,693. Using two variables—the absorbance (λ=595 nm) in LB and 1% agarose—we fit a bivariate normal distribution to determine the direction of maximum variance in the dataset represented by a straight line. This line represents a positive, linear correlation between cell growth in 1% agarose and liquid LB media; the majority of the 5445 mutants were positioned within 3 standard deviations from this line, indicating a strong correlation between *P. aeruginosa* cell growth in 1% agarose versus LB (Fig 2B). We calculated the geometric distance of every gene to this line and filtered mutants positioned 3 standard deviations away from the line. These mutants had minimum correlation between their absorbance measurements in 1% agarose compared to liquid LB and lie farthest from the line of maximum variance within the data set. Most of these genes had a large increase or decrease of cell growth in 1% agarose, yet they maintained a growth rate in liquid LB similar to *P. aeruginosa* wild type PA14 cells. *P. aeruginosa* mutants depicted by blue data points (n=115) have higher absorbance (λ=595 nm) in 1% agarose compared to mutants depicted by red data points (n=133) suggesting that mutants in red have lower stiffness values (Fig. 2B).

We performed gene enrichment analyses on the blue and red subsets of mutants using Fisher's exact test to correlate KEGG pathways with altered cell stiffness in our assay. A variety of KEGG pathways were enriched in mutants with higher stiffness (blue data points), including those correlated to peptidoglycan biosynthesis and glycerolipid metabolism pathways. KEGG pathways enriched for lower stiffness mutants (red data points) included alanine, aspartate, and glutamate metabolism pathways among those most enriched (Fig. 2C, 2D).

We determined GRABS scores of all mutants in the *P. aeruginosa* PA14 library to qualitatively compare mechanical changes and found the distribution of scores to be approximately normal (Fig. 3A). We rescreened 178 mutants from the whole genome screen that had GRABS scores < -10 to confirm the results. The rescreened mutants had predominately negative GRABS scores and the distribution of values was shifted towards lower mean GRABS values (-17.5) compared to data from screening the entire mutant collection (Fig. 3A). Rescreening of the top hits enabled us to assign variance for individual genes with a negative GRABS score. A list of 42 mutants with the largest negative GRABS scores (<-20) is illustrated in Fig 3B. Six mutants—among 42 in the list—did not have an assigned function, suggesting that the proteins coded by these genes may play a role in cell mechanics; further investigation is required.

We were interested in the cellular distribution of proteins encoded by stiffness-related genes across different cellular compartments, namely those that are cytoplasmic, periplasmic, and extracellular. An analysis of the subcellular localization of the 36 mutants with the largest negative GRABS scores indicated that proteins coded by 24 were cytoplasmic, 7 were associated with the cytoplasmic membrane, 2 were periplasmic, 1 was associated with the outer membrane

and for 2 mutants we didn't have localization information. We performed an analysis of the ontology of genes corresponding to mutants with the largest change in cell stiffness (Fig. 3C). Cluster of orthologous groups (COGs) analysis revealed that 6 genes (from 36) were from amino acid transport and metabolism category, supporting our gene enrichment analysis for lower stiffness genes. *dadA* caught our attention for several reasons: 1) it is clustered in the amino acid transport and metabolism COGS category; 2) it belongs to the most enriched pathway from the KEGG gene enrichment analysis (i.e., alanine, aspartate, and glutamate metabolism); 3) it codes for a cytoplasmic enzyme which makes its study feasible; and 4) it is involved in the pathway for D-Ala metabolism, which is an amino acid that is involved in constructing the peptidoglycan (Fig. 3B).

**D-Ala dehydrogenase (DadA) is a modulator of *P. aeruginosa* PA14 cell stiffness**

The abundance of D-amino acids is generally low in cells; the most abundant D-amino acid in bacteria is D-Ala. In bacteria, Alanine racemases convert L-Ala to D-Ala, which is subsequently incorporated into the peptidoglycan (Figure 1)[34]. Alanine racemases have emerged as a well-studied class of enzymes and as drug targets for antibiotics due to the role of D-Ala in peptidoglycan[35]. *P. aeruginosa* produces two alanine racemases: Alr and DadX. Mutagenesis studies reveal low levels of constitutively expressed Alr that serves an anabolic function in peptidoglycan assembly[34]. In contrast, DadX converts L-Ala into D-Ala in alanine catabolism pathway to support cell growth on L-Ala [28]. DadA is a D-Ala dehydrogenase that oxidatively deaminates D-Ala to pyruvate and ammonia (Fig. 1)[36]. Collectively, DadA, DadX, and Alr play an essential role in the utilization of D-Ala and L-Ala as sources of carbon and energy for cell growth[28, 37].

During peptidoglycan synthesis, D-Ala-D-Ala ligases (Ddl) consume the cytoplasmic pool of D-Ala to form D-Ala-D-Ala dipeptides, which are ligated on the tripeptide stem of UDP-MurNAc to form the UDP-MurNAc-pentapeptide (Fig. 1)[17]. MurG catalyzes the addition of GlcNAc to lipid I (~700 copies/cell) to produce lipid II (~2000 copies/cell)—the building block of peptidoglycan—containing the complete disaccharide pentapeptide monomer unit[38]. Lipid II is transported across the cytoplasmic membrane into the periplasm where it is incorporated into peptidoglycan[13, 38]. D-Ala is also formed by transpeptidase and carboxypeptidase activities involved in peptidoglycan assembly and remodeling. During crosslinking of newly synthesized peptidoglycan strands, transpeptidases cleave the terminal D-Ala, which returns it to the pool of cytosolic D-Ala via active transport (Fig. 1)[12, 13, 39].

We studied the role of DadA in *P. aeruginosa* cell stiffness. The transposon mutant of *dadA* in *P. aeruginosa* PA14 had a GRABS score of -18 (Fig 4A). To confirm that the change in cell stiffness was the result of deleting *dadA*, we complemented cells by expressing *dadA* in the PA14 *dadA::*Tn strain. Complementation of the *dadA* mutant requires expression of both *dadA* and *dadX* due to polar effects of the *dadA* MAR2xT7 transposon insertion[28]. We followed this precedent by complementing *dadA* with *dadX* using vector pUCP18 as previously reported[28]. Overexpressing DadA and DadX in Δ*dadA* cells of *P. aeruginosa* PA14 led to a complete recovery of the growth phenotype in 1% agarose and rescued the GRABS phenotype for the *dadA* transposon mutant (Fig. 4A).

We previously used a microfluidic approach to measure the bending rigidity of cells and confirmed that *Escherichia coli* mutants with negative GRABS scores have reduced cell stiffness[16]. To confirm that the *P. aeruginosa* PA14 *dadA*::Tn mutant has reduced cell stiffness, we used the microfluidic approach to apply a shear flow on single cells, measured the deflection of cells, fit the data to a mechanics model, and quantified changes in cell bending rigidity[16, 40].

We measured the bending rigidity for cells of *P. aeruginosa* PA14, including wild type, *dadA*::Tn, and *dadA* ::Tn containing p*dadAX*. Estimating the thickness of the peptidoglycan layer of *P. aeruginosa* to be 3.0 ± 0.5 nm[41], we converted bending rigidity values to Young's modulus (*E*, the intrinsic stiffness of a material defined by the slope of the stress strain curve) and found *dadA* transposon mutant to have a 3-fold reduction in Young's modulus (*E*=7.78 MPa) compared to wild type cells (*E*=24.8 MPa) (Fig. 4B). Complementation by DadA and DadX in the *dadA*::Tn mutant rescued the stiffness phenotype ( *E*=30.6 MPa). These results suggest *dadA* contributes to the maintenance of *P. aeruginosa* cell stiffness, leading to the hypothesis that inhibiting the D-Ala degradation increases the cellular concentration of free D-Ala and reduces cell stiffness.

**Increase in D-Ala levels reduces cell stiffness**

DadA is involved in catabolism of cytosolic D-Ala and its conversion into pyruvate. We hypothesize that the transposon mutant of *dadA* may either increase the concentration of cytosolic D-Ala or decreases the concentration of pyruvate. Pyruvate in Gram-negative bacteria is predominantly produced by glycolysis and the intracellular concentration of pyruvate is 390

μM[42] which is estimated to be 100x higher than the combined concentration of D- and L-Ala, i.e., 4μM[43]. Consequently, degradation of D-Ala into pyruvate may contribute to the intracellular pool of pyruvate minimally; suggesting the transposon mutant of *dadA* may have little effect on pyruvate levels. Our data is consistent with an increase in the intracellular concentration of D-Ala reducing *P. aeruginosa* cell stiffness.

To explore the hypothesis that an increase in the intracellular concentration of D-Ala reduces *P. aeruginosa* cell stiffness and to confirm the *dadA*::Tn mutant has higher levels of D-Ala compared to *P. aeruginosa* PA14 wild type cells, we treated cells with D-cycloserine (i.e., DCS; 4-amino-3-isoxazolidinone). DCS is a cyclic mimic of D-Ala that inhibits Ala racemase (Alr), D-Ala-D-Ala ligase (Ddl), and inhibits cell growth by decreasing the intracellular pool of D-Ala[44-46]. The minimum inhibitory concentration (MIC) of DCS against *P. aeruginosa* PA14 wild type cells was two-fold lower (12.5 mM) than for *dadA* transposon mutants (25 mM). We measured the growth of *P. aeruginosa* PA14 wild type and *dadA* transposon mutants in the presence of varying DCS concentrations and observed the *dadA*::Tn mutant grew to an absorbance of 0.5 (λ=595 nm) while wild-type cells grew to an absorbance of 0.03 after 16 h of incubation, suggesting an increase in the intracellular pool of D-Ala in *dadA* mutant transcends growth inhibition by DCS (Fig. 5A). Supplementing growth media with D-Ala (25 mM) enabled *dadA*::Tn mutant to tolerate 4x MIC of DCS (50 mM) and grow to an absorbance of 0.15 (λ=595 nm) after 16 h. This data is consistent with a higher intracellular level of D-Ala in *dadA* transposon mutant titrating down the inhibitory effect of DCS on cell growth (Fig. 5A). The MICs for DCS against *P. aeruginosa* are presumably high due to the effective drug efflux system

in this bacterium; in contrast DCS has been measured to have MICs in the range of 50-500 uM in *Mycobacterium smegmatis* and *E. coli* [47].

If a reduction in cell stiffness is linked to an increase in the D-Ala concentration in *P. aeruginosa* cells, we expect cells grown in the presence of exogenous D-Ala will have a lower GRABS score than cells growing in the absence of D-Ala. *P. aeruginosa* has at least two mechanisms for transporting D-Ala into cells. Transport of amino acids across the outer membrane of Gram-negative bacteria, including *P. aeruginosa* occurs by diffusion through porin channels or by active, carrier-mediated proton motive force-dependent systems that transport essential solutes into cells [39, 48, 49]. *P. aeruginosa* also contains amino acid permeases that transport D-Ala into cells from the extracellular environment nutrient media[39]. To test the effect of D-Ala concentration on the stiffness of *P. aeruginosa* PA14 cells, we titrated different D-Ala concentration (25, 50 and 100 mM) in the nutrient media and measured GRABS scores of wild type and *dadA*::Tn mutant. The *dadA*::Tn mutant grown in the presence of 25 mM D-Ala had an 24.4% decrease in GRABS score compared to *P. aeruginosa* PA14 wild type cells grown in the absence of D-Ala. Increasing the D-Ala concentration to 50 mM reduced the GRABS score to -31.2%; at a concentration of 100 mM D-Ala, the GRABS score was -34.27% (Fig 5B). As a control, we also measured the GRABS score for *P. aeruginosa* PA14 wild type cells grown in the presence of D-Ala and observed no change in the GRABS score when we increased the D-Ala concentration from 25 mM to 100 mM (Fig 5B). These results suggest that wild type carefully regulates the concentration of D-Ala in the cells via utilizing D-Ala such that it doesn't exhibit lower stiffness phenotype in GRABS score.

Since DadA utilizes D-Ala in the cells, it was interesting to know how the *dadA* responds to higher D-Ala levels in the growth medium. We measured the change in *dadA* transcription in *P. aeruginosa* PA14 by growing cells in two conditions: 1) LB; and 2) LB supplemented with 25 mM D-Ala. We performed qPCR experiments and found *P. aeruginosa* PA14 cells grown in the presence of 25 mM D-Ala have a 2-3-fold higher level of *dadA* transcription than cells grown in plain LB (SI). This result support previously published study in *P. aeruginosa* strain PAO1, where *dadA* promoter activity was measured 12-fold higher when cells were grown in the presence of D-Ala compared to cells grown in the defined medium only[37]. These results suggest that the cell carefully regulate the intracellular concentration of D-Ala by triggering the expression of DadA, which siphons off excess D-Ala and regulate the stiffness of wild type cells.

We hypothesized that a higher cytosolic concentration of D-Ala present in the *P. aeruginosa dadA* transposon mutant increases the concentration of the D-Ala-D-Ala dipeptide—one of the substrates for MurG on the route to synthesis of lipid II—and affects the stiffness of cells through altering peptidoglycan structure or assembly. To test this hypothesis, we performed GRABS measurements on PA14 wild type and the *dadA*::Tn mutant in the presence of D-Ala-D-Ala (15, 25, 50 and 100 mM) supplemented in LB. We observed a 30.4% decrease in the GRABS score of the *dadA*::Tn mutant in the presence of 15mM D-Ala-D-Ala and higher D-Ala-D-Ala concentrations did not further lower the GRABS score for the mutants (Fig 5C).

These data indicate that a significant change in cell stiffness is correlated to the activity of DadA and its role degrading excess D-Ala into pyruvate. Since this pathway is expected to contribute only minimally to the total concentration of free pyruvate in cells, we attribute stiffness changes

to the concentration of D-Ala (that is, not incorporated into peptidoglycan) and possibly its incorporation into D-Ala-D-Ala.

**Peptidoglycan synthesis is sensitive to the concentration of D-Ala**

We hypothesize that high concentrations of D-Ala may affect enzymes that biosynthesize peptidoglycan, alter the structure or composition of peptidoglycan, and regulate the mechanical properties of *P. aeruginosa* cells. To test this hypothesis, we measured the transcription of various genes coding for proteins involved in the peptidoglycan synthesis pathway using qPCR. Specifically, we selected genes that codes for amino acid ligases (MurC, Ddl, and MurF), a glycosyltransferase (MurG), a transpeptidase (PonA*)*, a DD-carboxypeptidase (DacC), and an DD-endopeptidase (PbpG).

A comparison of the transcription levels of the amino acid ligases *murC, ddl,* and *murF* in *P. aeruginosa* PA14 wild type and the *dadA*::Tn mutant indicated *ddl* and *murF* were 23% and 20% downregulated in the *dadA* transposon mutant compared to wild type cells growing in LB. In contrast, the transcription of *murC* was 20% higher in mutant compared to wild type cells. Adding 25 mM D-Ala to cells growing in LB did not change the level of transcription of *murC*, however *ddl* and *murF* transcription levels decreased by 33% and 27% in the presence of D-Ala compared to wild type cells grown in plain LB. DD-carboxypeptidases and DD-endopeptidases cleave the terminal D-Ala residue from the pentapeptide on peptidoglycan (before or after crosslinking?). Transcription level of *dacC* and *pbpG*, we observed *dacC* transcription is reduced by 38% in the absence of *dadA* compared to wild type cells; growing cells in the presence of D-

Ala did not change *dacA* transcription. *pbpG* transcription did not change significantly for mutant in LB or LB supplemented with D-Ala (Fig 5D).

We did not observe a significant difference in the expression level of *murG* in *P. aeruginosa* PA14 wild type and *dadA*::Tn mutant cells, however *ponA* transcription was reduced 32% in the PA14 *dadA* mutant compared to wild type cells; adding D-Ala did not change *ponA or murG* transcription significantly (Fig 5D). Transpeptidase PonA crosslinks the peptide chains of PG monomers and reduction in the *ponA* levels in principle would reduce the crosslinking of PG. To quantify the differences in the PG composition and cross-linking density of mutant and wild type cells, we used ultra performance liquid chromatography-mass spectrometry (UPLC-MS). Compared to wild type cells, *dadA*::Tn had more monomers, fewer dimers and trimers, but anhydrous-containing saccharides or terminating end of the glycan-strand did not change (Fig 6A). We also calculated the PG cross-linking density of wild type and *dadA*::Tn and we found that mutant had lower crosslinking density compared to wild type cells (Fig. 6B).

Together these results suggest that in *P. aeruginosa* PA14 *dadA* mutant, peptidoglycan biosynthesis pathway genes—particularly those coding for enzymes that metabolize D-Ala or release D-Ala—are significantly downregulated, which might lead to the downregulation of the whole pathway when cells have higher level of D-Ala in PA14 *dadA* transposon mutant.

**Conclusion**

Using the GRABS assay, we identified 42 novel cell stiffness regulators in *P. aeruginosa* by screening a genome-wide collection of transposon mutants from a non-redundant transposon library of *P. aeruginosa* PA14 strain. The genes we discovered had three interesting characteristics: 1) they are ontologically diverse; 2) they are largely unconnected to cell mechanics; and 3) they reveal surprising connections between physiology and cell mechanics (Figure 3C). Our methodology also revealed six mutants with hypothetical gene function, suggesting that the proteins coded by these genes may play a role in cell mechanics.

We established and characterized the role of D-Alanine dehydrogenase, DadA in regulating cell stiffness. We found that *dadA* mutant have higher intracellular D-Ala concentrations, which affect the transcription of the peptidoglycan synthesis enzymes including transpeptidases. Transpeptidase is a crucial enzyme that crosslinks the peptide chains of peptidoglycan monomers to form dimers, trimers and tetramers. Using UPLC-MS analysis, we found that *dadA* mutant had lower crosslinking density compared to wild type cells which led to more elastic peptidoglycan and lower cell stiffness. Our study revealed the importance the D-Ala metabolism in maintaining cell mechanical properties as increase in D-Ala levels reduce cell stiffness. Finally, we hypothesize a model in which DadA acts as a valve to control the concentration of D-Ala in cells and regulate mechanical properties of *P. aeruginosa.* Further investigations are necessary to determine the viability of using DadA as a potential drug target in combination with traditional cell wall antibiotics against *Pseudomonas* infections and contaminations.

**Fig. 1. Fates of D-Ala in Gram-negative bacteria**

Cartoon represents fates of D-Ala in the cell. *P. aeruginosa* cells have two alanine racemases (Alr and DadX) that interconvert L-Ala to D-Ala. DadA is a D-amino acid dehydrogenase that degrades D-Ala into pyruvate. Ddl converts two D-Ala molecules into D-Ala-D-Ala dipeptide which is utilized to form Lipid I from MurNAc-tripeptide by MurF. MraY and MurG form Lipid II which is flipped and polymerized by glycosyltransferases and transpeptidases. Transpeptidase (PonA) crosslinks stem peptides during peptidoglycan biosynthesis by releasing the terminal D-Ala of the stem peptide in the periplasm. DD-carboxypeptidase (DacC) and DD-endopeptidases (PbpG) also release the terminal D-Ala from the un-crosslinked lipid II in the periplasm. Free D-Ala in the periplasm and in the extracellular environment gets transported into the cells via alanine transporters and permeases.

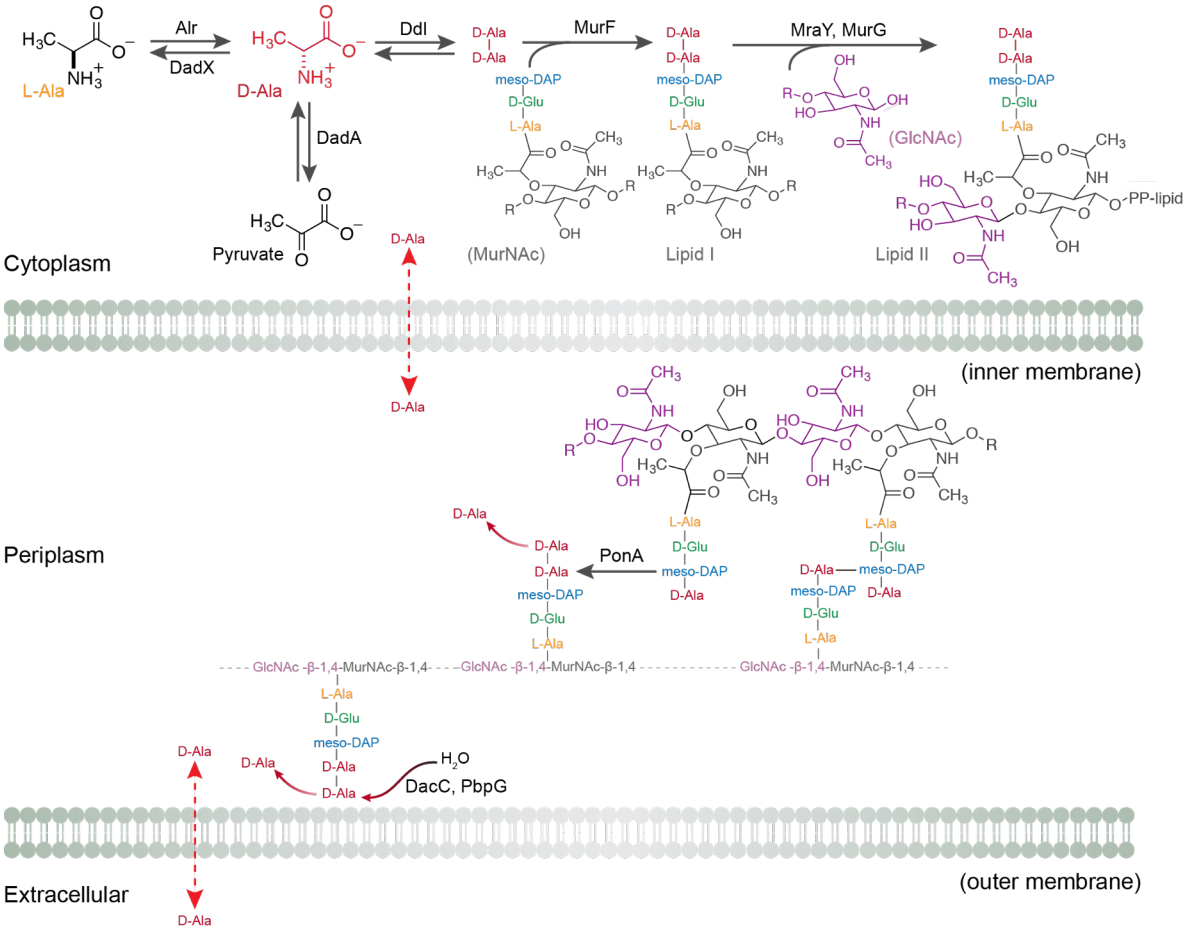
L-Ala
Alr
DadX
D-Ala
DadA
Pyruvate
Ddl
MurF
MraY, MurG
(GlcNAc)
(MurNAc)
Lipid I
Lipid II
PP-lipid
Cytoplasm
(inner membrane)
Periplasm
PonA
GlcNAc -β-1,4-MurNAc-β-1,4-
DacC, PbpG
$H_2O$
Extracellular
(outer membrane)

**Fig. 1**

**Fig. 2. Genome-wide stiffness screen of *Pseudomonas aeruginosa***

**A)** Scatter plot of all gene transposon mutants in *P. aeruginosa* PA14 with respective absorbance values (λ=595 nm) for cell growth in LB and in 1% agarose infused with LB; each point represents a single gene transposon mutant. Regions in the plot with the highest density of data points are depicted in yellow.

**B)** Genome-wide stiffness screening data fit with a bivariate normal distribution. Transposon mutants highlighted by blue points (n=115 genes) have higher growth in 1% agarose compared to red data points (n=133 genes). Genes that lie within the interval between two dashed lines (in grey) follow linear growth model.

**C)** KEGG pathway enrichment for blue gene subset, which have higher stiffness and red subset genes with lower stiffness.

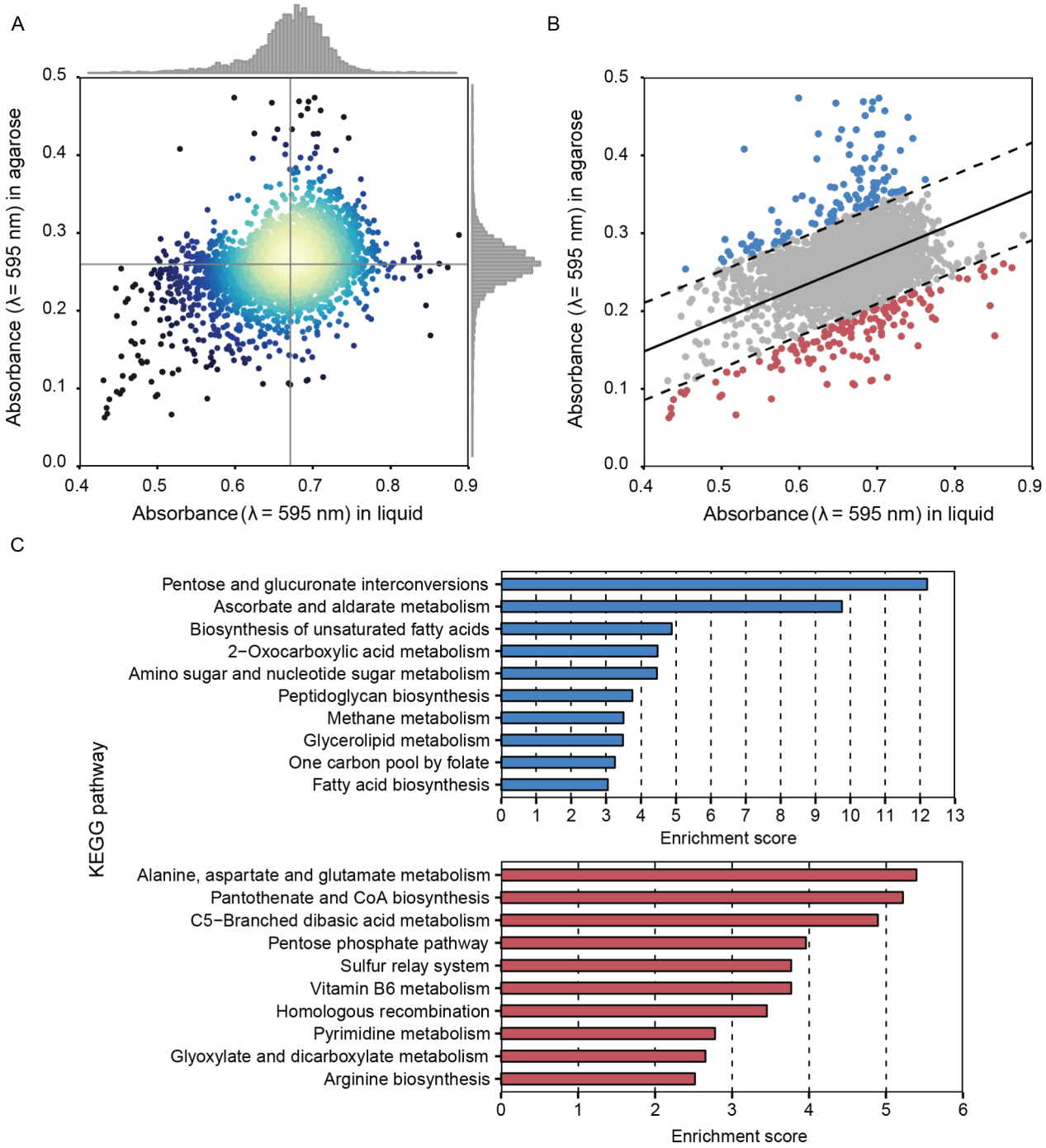
A
B
C
Absorbance (λ= 595 nm) in agarose
Absorbance (λ = 595 nm) in liquid
KEGG pathway
Enrichment score
Pentose and glucuronate interconversions
Ascorbate and aldarate metabolism
Biosynthesis of unsaturated fatty acids
2−Oxocarboxylic acid metabolism
Amino sugar and nucleotide sugar metabolism
Peptidoglycan biosynthesis
Methane metabolism
Glycerolipid metabolism
One carbon pool by folate
Fatty acid biosynthesis
Alanine, aspartate and glutamate metabolism
Pantothenate and CoA biosynthesis
C5−Branched dibasic acid metabolism
Pentose phosphate pathway
Sulfur relay system
Vitamin B6 metabolism
Homologous recombination
Pyrimidine metabolism
Glyoxylate and dicarboxylate metabolism
Arginine biosynthesis

**Fig. 2**

**Fig. 3. Stiffness genes span a range of biochemical pathways**

**A)** A histogram depicting that the GRABS score distribution of genes that were re-screened have a reduction in the mean GRABS score compared to the complete screen.

**B)** A plot of the GRABS scores along with the corresponding variance for 42 re-screened genes. 37 out of 43 genes were annotated and were assigned function. 6 out of top 42 hits did not have any annotation and were named after their respective gene locus in the genome. *P. aeruginosa PA14 dadA*::Tn mutant (depicted in a red) have very low variance in the GRABS score and consistently produce a negative GRABS score.

**C)** Subcellular compartment information for 42 genes from **(B)**.

**(D)** Gene ontology description for the top hits.

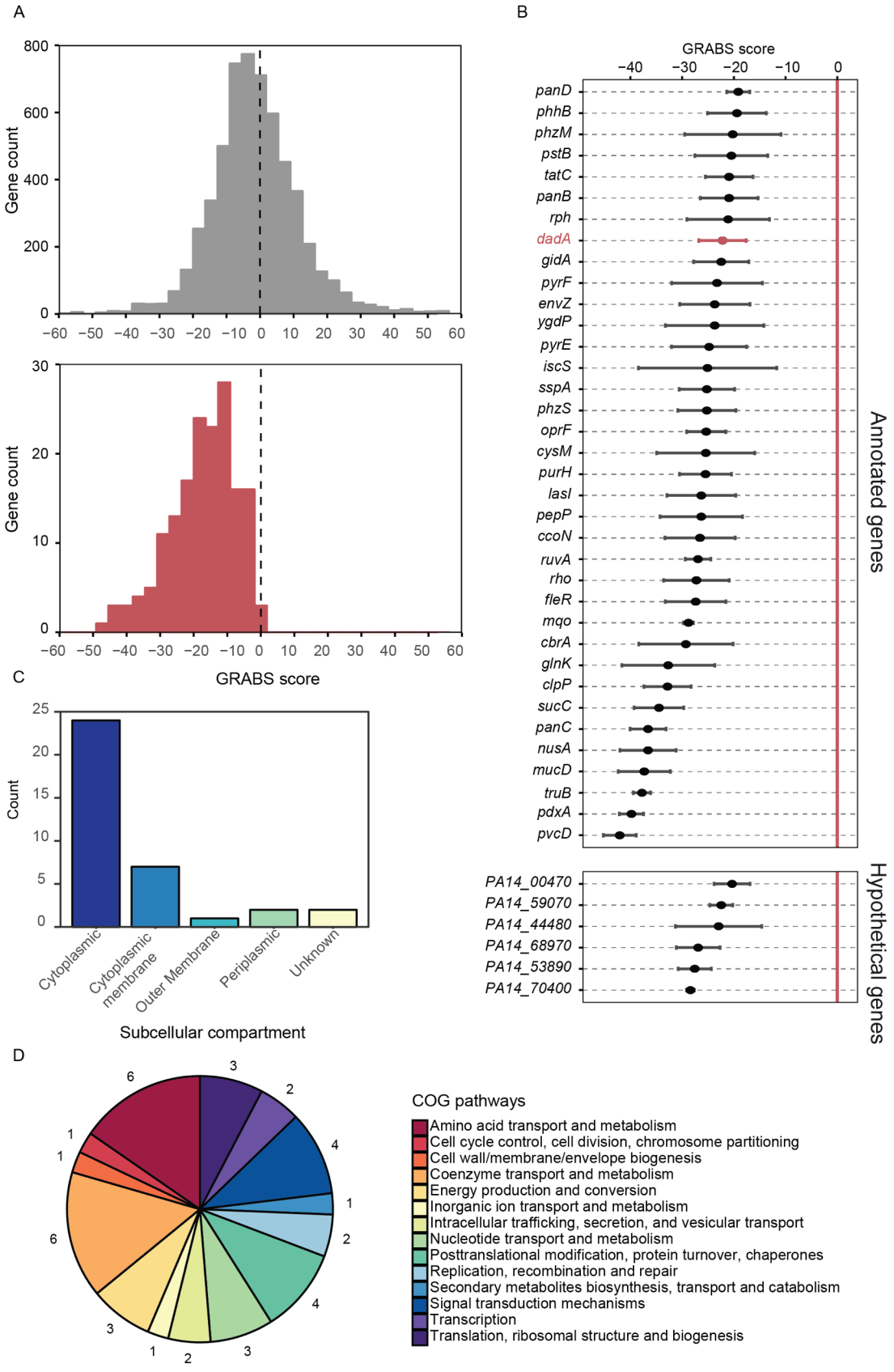
A
Gene count
GRABS score
B
GRABS score
panD
phhB
phzM
pstB
tatC
panB
rph
dadA
gidA
pyrF
envZ
ygdP
pyrE
iscS
sspA
phzS
oprF
cysM
purH
lasI
pepP
ccoN
ruvA
rho
fleR
mqo
cbrA
glnK
clpP
sucC
panC
nusA
mucD
truB
pdxA
pvcD
Annotated genes
PA14_00470
PA14_59070
PA14_44480
PA14_68970
PA14_53890
PA14_70400
Hypothetical genes
C
Count
Cytoplasmic
Cytoplasmic membrane
Outer Membrane
Periplasmic
Unknown
Subcellular compartment
D
COG pathways
Amino acid transport and metabolism
Cell cycle control, cell division, chromosome partitioning
Cell wall/membrane/envelope biogenesis
Coenzyme transport and metabolism
Energy production and conversion
Inorganic ion transport and metabolism
Intracellular trafficking, secretion, and vesicular transport
Nucleotide transport and metabolism
Posttranslational modification, protein turnover, chaperones
Replication, recombination and repair
Secondary metabolites biosynthesis, transport and catabolism
Signal transduction mechanisms
Transcription
Translation, ribosomal structure and biogenesis

**Fig. 3**

**Fig. 4. D-Ala dehydrogenase (DadA) is a modulator of *P. aeruginosa* cell stiffness**

**A)** GRABS score for *P. aeruginosa* wild type, *dadA* transposon mutant, and *dadA* complementation strain.

**B)** Young's modulus of wild-type, dadA transposon mutant and dadA mutant + pdadAX complementation vector.

**C)** Expression of *dadA* in wild type cells in two different media condition, plain LB and LB supplemented with D-Ala (25mM).

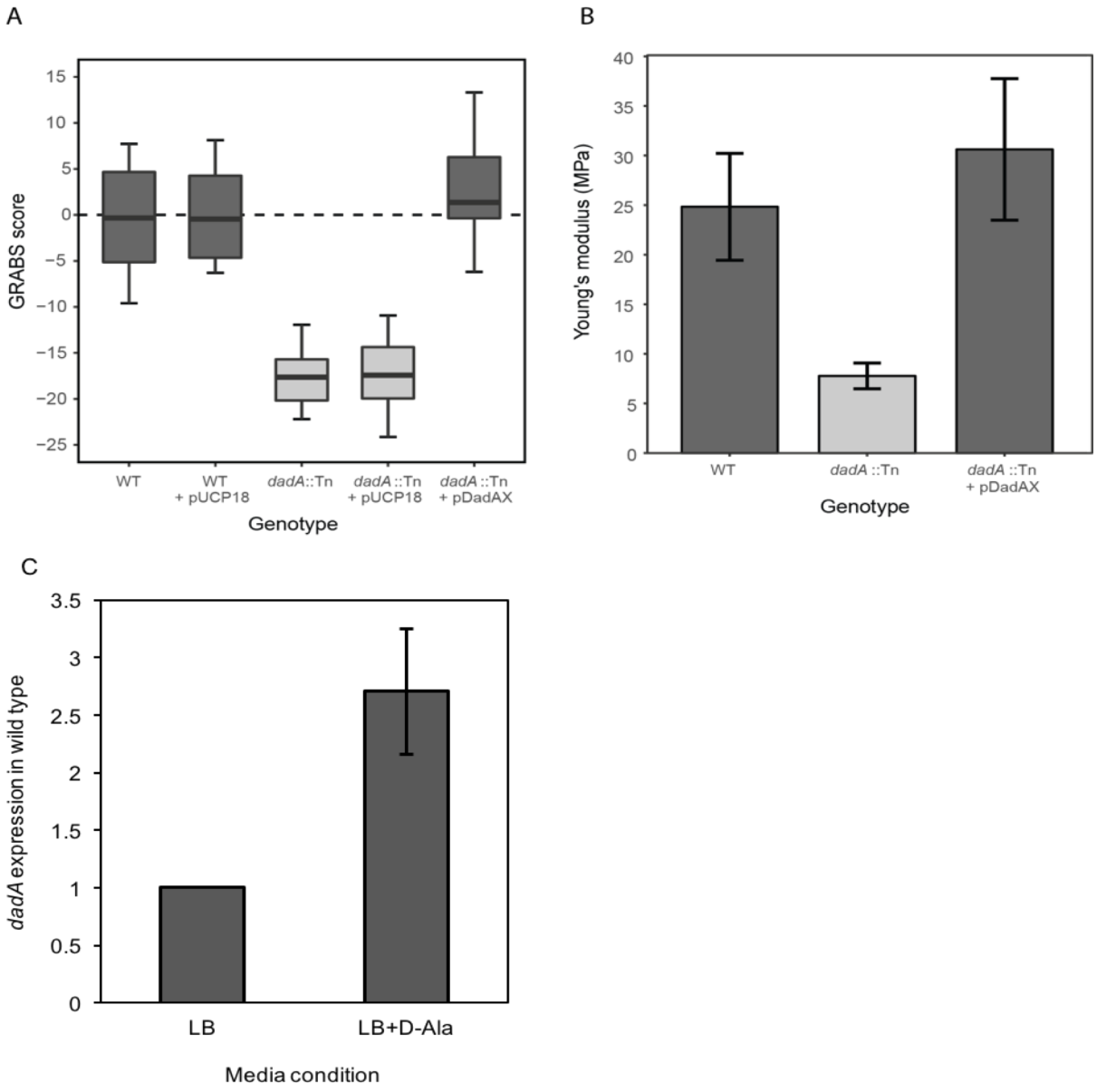
A
GRABS score
15
10
5
0
−5
−10
−15
−20
−25
WT
WT + pUCP18
dadA::Tn
dadA ::Tn + pUCP18
dadA ::Tn + pDadAX
Genotype
B
Young's modulus (MPa)
40
35
30
25
20
15
10
5
0
WT
dadA ::Tn
dadA ::Tn + pDadAX
Genotype
C
dadA expression in wild type
3.5
3
2.5
2
1.5
1
0.5
0
LB
LB+D-Ala
Media condition

**Fig. 4**

**Fig. 5. Peptidoglycan biosynthesis pathway is sensitive to D-Ala levels**

**A)** In the presence of sub-MIC concentration of DCS, *P. seruginosa PA14 dadA*::Tn mutant grows better compared to PA14 wild type strain. Y-axis represents absorbance (λ=595 nm) after 16 hours of growth. Adding D-Ala in the medium overall increases the growth phenotype of *dadA* mutant.

**B)** Increase in the exogenous D-Ala supplementation leads to lower GRABS score for *dadA*::Tn mutant compared to wild type.

**C)** *dadA*::Tn mutant grown in LB media supplemented with difference D-Ala-D-Ala concentrations (mM) had 30% decrease in the GRABS score compared to wild type.

**D)** *P. aeruginosa* PA14 *dadA*::Tn mutant has lower transcription level of *ponA*, *dacC, murF*, *ddl.* These genes code for protein that either releases D-Ala in the medium (*dacC, ponA)*, or utilizes D-Ala as a substrate for PG precursor synthesis (*ddl, murF*).

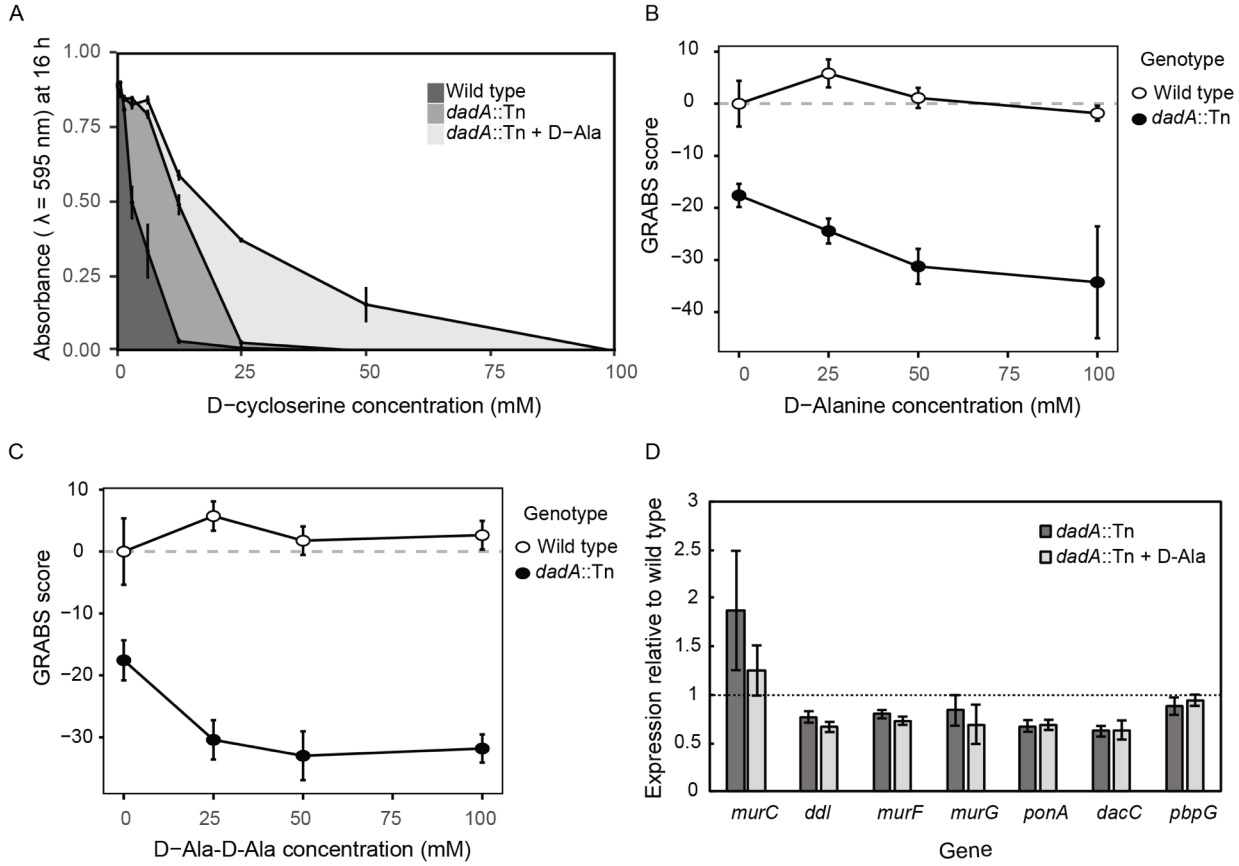
A
Absorbance ( λ = 595 nm) at 16 h
1.00
0.75
0.50
0.25
0.00
0
25
50
75
100
D−cycloserine concentration (mM)
Wild type
dadA::Tn
dadA::Tn + D−Ala
B
GRABS score
10
0
−10
−20
−30
−40
D−Alanine concentration (mM)
Genotype
Wild type
dadA::Tn
C
GRABS score
D−Ala-D-Ala concentration (mM)
Genotype
Wild type
dadA::Tn
D
Expression relative to wild type
3
2.5
2
1.5
1
0.5
0
dadA::Tn
dadA::Tn + D-Ala
murC
ddl
murF
murG
ponA
dacC
pbpG
Gene

**Fig. 5**

**Fig. 6. Peptidoglycan biosynthesis pathway is sensitive to D-Ala levels**

**Fig. 4.** Alterations in the PG muropeptide composition of *P. aeruginosa* wild type and *dadA* mutant.

**A)** UPLC-MS data reveal that the muropeptide composition of *P. aeruginosa* wild type and *dadA* mutant differs slightly in the abundance of monomer, dimer, and anhydrous-terminated saccharides. $n = 3$ biological replicates

**B)** We observed a relative decrease in PG cross-linking of *dadA*::Tn compared to wild type cells. Error bars represent the standard deviation of the mean.

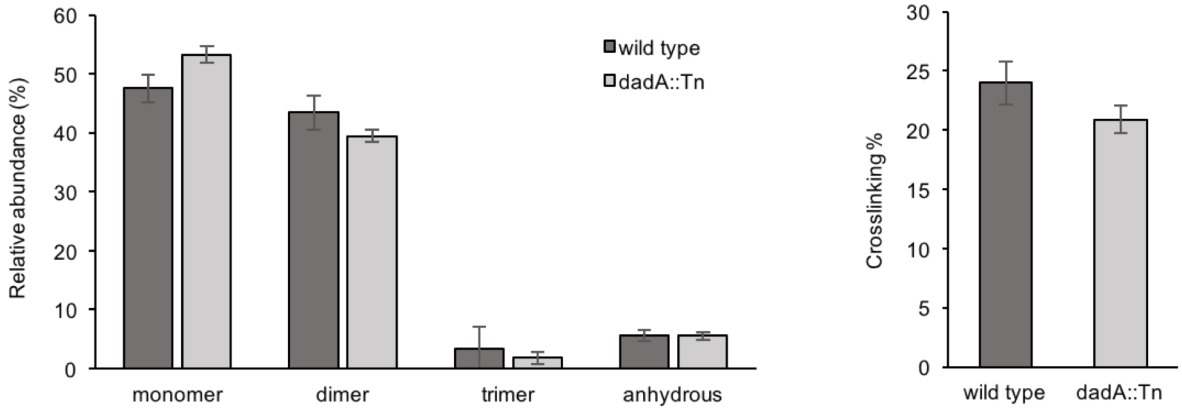
Relative abundance (%)
60
50
40
30
20
10
0
wild type
dadA::Tn
monomer
dimer
trimer
anhydrous
Crosslinking %
30
25
20
15
10
5
0
wild type
dadA::Tn

**Fig. 6**

**Table 1. Muropeptides analyzed by UPLC-MS in positive ion mode.** Identification of muropeptides by MS. Muropeptides were identified within (± 0.01 m/z) of the calculated muropeptide mass values. MS peaks were used to identify and quantify area under curve of UPLC $UV_{205nm}$ peaks.

| Peak | Retention time (min) | Calculated mass | | | Length of stem peptides |
|---|---|---|---|---|---|
| | | H+ | 2+ | 3+ | |
| 1 | 7.7 | 871.3784 | 436.1892 | 291.1261 | Tri |
| 2 | 8.6 | 928.3999 | 464.6999 | 310.1333 | Tetra-Gly(4) |
| 3 | 9.2 | 699.2936 | 350.1468 | 233.7645 | Di |
| 4 | 10.8 | 999.4370 | 500.2185 | 333.8123 | Penta-Gly (4) |
| 5 | 11.6 | 1243.5202 | 622.2601 | 415.5067 | Tri-Tri (-DS) |
| 6 | 12 | 942.4155 | 471.7078 | 314.8052 | Tetra |
| 7a | 13.6 | 1723.7102 | 862.3551 | 575.2367 | Tri-Tri |
| 7b | 20.6 | 1723.7102 | 862.3551 | 575.2367 | Tri-Tri |
| 8 | 21.3 | 1851.7970 | 926.3985 | 617.9323 | Tetra-Tetra-Gly(4) |
| 9a | 21.7 | 1794.7756 | 897.8878 | 598.9252 | Tetra-Tri |
| 10 | 22.6 | 1922.8341 | 961.9171 | 641.6114 | Tetra-Tetra-Gly (5) |
| 9b | 22.8 | 1794.7756 | 897.8878 | 598.9252 | Tetra-Tri |
| 11 | 24.1 | 1865.8127 | 933.4063 | 622.6042 | Tetra-Tetra |
| 12 | 28.6 | 2846.2313 | 1423.6156 | 949.4104 | Penta-Gly(5)-Tetra-Tetra |
| 13 | 30.1 | 2789.2098 | 1395.1049 | 930.4033 | Tetra-Tetra-Tetra |
| 14a | 30.7 | 1774.7402 | 887.8701 | 592.2467 | anhydro Tetra-Tri |
| 14b | 32.1 | 1774.7402 | 887.8701 | 592.2467 | anhydro Tetra-Tri |
| 15 | 33.2 | 1845.7865 | 923.3932 | 615.9288 | anhydro Tetra-Tetra |

**References**


1. Hiramatsu, K., *Vancomycin-resistant Staphylococcus aureus: a new model of antibiotic resistance.* Lancet Infect Dis, 2001. **1**(3): p. 147-55.

2. Stock, J.B., B. Rauch, and S. Roseman, *Periplasmic Space in Salmonella-Typhimurium and Escherichia-Coli.* Journal of Biological Chemistry, 1977. **252**(21): p. 7850-7861.

3. Flemming, H.C. and J. Wingender, *The biofilm matrix.* Nature Reviews Microbiology, 2010. **8**(9): p. 623-633.

4. Rothschild, L.J. and R.L. Mancinelli, *Life in extreme environments.* Nature, 2001. **409**(6823): p. 1092-1101.

5. Hall-Stoodley, L., J.W. Costerton, and P. Stoodley, *Bacterial biofilms: from the natural environment to infectious diseases.* Nat Rev Microbiol, 2004. **2**(2): p. 95-108.

6. Dajani, A.S., et al., *Prevention of bacterial endocarditis.* Circulation, 1997. **96**(1): p. 358-366.

7. Wood, J.M., *Bacterial responses to osmotic challenges.* Journal of General Physiology, 2015. **145**(5): p. 381-388.

8. Tuson, H.H., et al., *Measuring the stiffness of bacterial cells from growth rates in hydrogels of tunable elasticity.* Mol Microbiol, 2012. **84**(5): p. 874-91.

9. Razin, S. and M. Argaman, *Lysis of Mycoplasma, bacterial protoplasts, spheroplasts and L-forms by various agents.* Microbiology, 1963. **30**(1): p. 155-172.

10. Walsh, C., *Antibiotics: actions, origins, resistance.* 2003.

11. Reynolds, P.E., *Structure, Biochemistry and Mechanism of Action of Glycopeptide Antibiotics.* European Journal of Clinical Microbiology & Infectious Diseases, 1989. **8**(11): p. 943-950.

12. Typas, A., et al., *From the regulation of peptidoglycan synthesis to bacterial growth and morphology.* Nature Reviews Microbiology, 2012. **10**(2): p. 123-136.

13. Vollmer, W. and U. Bertsche, *Murein (peptidoglycan) structure, architecture and biosynthesis in Escherichia coli.* Biochim Biophys Acta, 2008. **1778**(9): p. 1714-34.

14. Park, J.T. and T. Uehara, *How bacteria consume their own exoskeletons (Turnover and recycling of cell wall peptidoglycan).* Microbiology and Molecular Biology Reviews, 2008. **72**(2): p. 211-227.

15. Horcajo, P., M.A. de Pedro, and F. Cava, *Peptidoglycan plasticity in bacteria: stress-induced peptidoglycan editing by noncanonical D-amino acids.* Microb Drug Resist, 2012. **18**(3): p. 306-13.

16. Auer, G.K., et al., *Mechanical Genomics Identifies Diverse Modulators of Bacterial Cell Stiffness.* Cell Systems, 2016. **2**(6): p. 402-411.

17. Barreteau, H., et al., *Cytoplasmic steps of peptidoglycan biosynthesis.* FEMS Microbiol Rev, 2008. **32**(2): p. 168-207.

18. Bugg, T.D.H. and C.T. Walsh, *Intracellular Steps of Bacterial-Cell Wall Peptidoglycan Biosynthesis - Enzymology, Antibiotics, and Antibiotic-Resistance.* Natural Product Reports, 1992. **9**(3): p. 199-215.

19. Kohanski, M.A., D.J. Dwyer, and J.J. Collins, *How antibiotics kill bacteria: from targets to networks.* Nature Reviews Microbiology, 2010. **8**(6): p. 423-435.

20. Davies, J., *Inactivation of antibiotics and the dissemination of resistance genes.* Science, 1994. **264**(5157): p. 375-82.

21. Donowitz, G.R. and G.L. Mandell, *Drug therapy. Beta-lactam antibiotics (2).* N Engl J Med, 1988. **318**(8): p. 490-500.

22. Donowitz, G.R. and G.L. Mandell, *Beta-Lactam antibiotics (1).* N Engl J Med, 1988. **318**(7): p. 419-26.

23. Wright, G.D., *Bacterial resistance to antibiotics: Enzymatic degradation and modification.* Advanced Drug Delivery Reviews, 2005. **57**(10): p. 1451-1470.

24. Livermore, D.M., *Multiple mechanisms of antimicrobial resistance in Pseudomonas aeruginosa: Our worst nightmare?* Clinical Infectious Diseases, 2002. **34**(5): p. 634-640.

25. Lambert, P.A., *Mechanisms of antibiotic resistance in Pseudomonas aeruginosa.* Journal of the Royal Society of Medicine, 2002. **95**: p. 22-26.

26. Lee, D.G., et al., *Genomic analysis reveals that Pseudomonas aeruginosa virulence is combinatorial.* Genome Biology, 2006. **7**(10).

27. Liberati, N.T., et al., *An ordered, nonredundant library of Pseudomonas aeruginosa strain PA14 transposon insertion mutants (vol 103, pg 2833, 2006).* Proceedings of the National Academy of Sciences of the United States of America, 2006. **103**(52): p. 19931-19931.

28. Boulette, M.L., et al., *Characterization of Alanine Catabolism in Pseudomonas aeruginosa and Its Importance for Proliferation In Vivo.* Journal of Bacteriology, 2009. **191**(20): p. 6329-6334.

29. Amir, A., et al., *Bending forces plastically deform growing bacterial cell walls.* Proc Natl Acad Sci U S A, 2014. **111**(16): p. 5778-83.

30. Brown, P.J., et al., *Polar growth in the Alphaproteobacterial order Rhizobiales.* Proc. Natl Acad. Sci. USA, 2012. **109**(5): p. 1697-1701.

31. Desmarais, S.M., et al., *Isolation and preparation of bacterial cell walls for compositional analysis by ultra performance liquid chromatography.* J Vis Exp, 2014(83): p. e51183.

32. Ottolenghi, A.C., M. Caparros, and M.A. de Pedro, *Peptidoglycan tripeptide content and cross-linking are altered in Enterobacter cloacae induced to produce AmpC beta-lactamase by glycine and D-amino acids.* J. Bacteriol., 1993. **175**(5): p. 1537-1542.

33. Pisabarro, A.G., M.A. de Pedro, and D. Vazquez, *Structural modifications in the peptidoglycan of Escherichia coli associated with changes in the state of growth of the culture.* J. Bacteriol., 1985. **161**(1): p. 238-242.

34. Walsh, C.T., *Enzymes in the D-Alanine Branch of Bacterial-Cell Wall Peptidoglycan Assembly.* Journal of Biological Chemistry, 1989. **264**(5): p. 2393-2396.

35. Radkov, A.D. and L.A. Moe, *Bacterial synthesis of D-amino acids.* Applied Microbiology and Biotechnology, 2014. **98**(12): p. 5363-5374.

36. Pioli, D., W.A. Venables, and F.C. Franklin, *D-Alanine dehydrogenase. Its role in the utilisation of alanine isomers as growth substrates by Pseudomonas aeruginosa PA01.* Arch Microbiol, 1976. **110**(23): p. 287-93.

37. He, W., C. Li, and C.D. Lu, *Regulation and characterization of the dadRAX locus for D-amino acid catabolism in Pseudomonas aeruginosa PAO1.* J Bacteriol, 2011. **193**(9): p. 2107-15.

38. van Heijenoort, J., *Assembly of the monomer unit of bacterial peptidoglycan.* Cell Mol Life Sci, 1998. **54**(4): p. 300-4.

39. Kay, W.W. and A.F. Gronlund, *Amino acid transport in Pseudomonas aeruginosa.* J Bacteriol, 1969. **97**(1): p. 273-81.

40. Amir, A., et al., *Bending forces plastically deform growing bacterial cell walls.* Proceedings of the National Academy of Sciences of the United States of America, 2014. **111**(16): p. 5778-5783.

41. Matias, V.R., et al., *Cryo-transmission electron microscopy of frozen-hydrated sections of Escherichia coli and Pseudomonas aeruginosa.* J Bacteriol, 2003. **185**(20): p. 6112-8.

42. Albe, K.R., M.H. Butler, and B.E. Wright, *Cellular Concentrations of Enzymes and Their Substrates.* Journal of Theoretical Biology, 1990. **143**(2): p. 163-195.

43. Yuan, J., et al., *Kinetic flux profiling of nitrogen assimilation in Escherichia coli.* Nature Chemical Biology, 2006. **2**(10): p. 529-530.

44. Lambert, M.P. and F.C. Neuhaus, *Mechanism of D-Cycloserine Action - Alanine Racemase from Escherichia-Coli W.* Journal of Bacteriology, 1972. **110**(3): p. 978-&.

45. Wargel, R.J., C.A. Shadur, and F.C. Neuhaus, *Mechanism of D-Cycloserine Action - Transport Mutants for D-Alanine, D-Cycloserine, and Glycine.* Journal of Bacteriology, 1971. **105**(3): p. 1028-&.

46. Wargel, R.J., C.A. Shadur, and F.C. Neuhaus, *Mechanism of D-Cycloserine Action - Transport Systems for D-Alanine, D-Cycloserine, L-Alanine, and Glycine.* Journal of Bacteriology, 1970. **103**(3): p. 778-&.

47. Gottlieb, D. and P.D. Shaw, *Mechanism of action*. Vol. 1. 2012: Springer Science & Business Media.

48. Reitzer, L., *Biosynthesis of Glutamate, Aspartate, Asparagine, L-Alanine, and D-Alanine.* EcoSal Plus, 2004. **1**(1).

49. Chopra, I., *Molecular Mechanisms Involved in the Transport of Antibiotics into Bacteria.* Parasitology, 1988. **96**: p. S25-S44.

# CHAPTER 3

## Dynamic self-assembly of motile bacteria in liquid crystals

Adapted from

Rishi R. Trivedi*, Peter C. Mushenheim*, Hannah H. Tuson, Douglas B. Weibel, Nicholas L. Abbott, Dynamic self-assembly of motile bacteria in liquid crystals. Soft matter. 2014;10(1):88-95.

* Equal contribution

**Abstract**

Bacteria display complex, dynamical and cooperative behaviors that are guided by the mechanical and biochemical environments in which they live. Here we report an investigation of the bacterium *Proteus mirabilis* dispersed in a model anisotropic viscoelastic medium comprised of a lyotropic liquid crystal (LC). We observe behaviors of the bacteria that emerge from the interplay of forces generated by the flagella of the bacteria and the elasticity of the LC, both of which are comparable in magnitude for *Proteus mirabilis.* In contrast to passive microparticles (including non-motile bacteria) that associate irreversibly in LCs via elasticity-mediated forces, we observe motile bacteria to form dynamic multiparticle assemblies, where dissociation driven by flagella-derived forces occurs in a direction determined by the LC. We also observe motile bacteria adhere to and propel themselves parallel to the LC director at isotropic fluid-LC interfaces, and escape through topological defects at the interface using flagella-derived forces. Non-motile bacteria and other passive synthetic microparticles, in contrast, adsorb irreversibly at the interface. Finally, we observe spatial variations in the LC orientation to guide the trajectory of bacteria around topological defects in the LC. Overall, these observations and others reported in this paper provide insights into the fundamental dynamical behaviors of bacteria in complex anisotropic environments and suggest that motile bacteria in LCs are an exciting model system for exploration of principles for the design of active media.

**Introduction**

Bacteria adapt to a broad range of environments with varied physical and chemical properties. Aspects of these habitats can impact the behavior and fitness of these microorganisms (*1*). Many such habitats are isotropic in nature: that is, they possess direction-independent physical properties. However, bacteria also colonize microenvironments that have anisotropic properties (e.g., optical, mechanical, and diffusional), including those enriched in collagen, cellulose, chitin, and synovial fluid, and the matrix of extracellular polymeric substances associated with bacterial biofilms (*2*-5). How the anisotropy of these environments influences dynamic behaviors of bacteria remains poorly understood. In this paper, we address this topic by studying bacteria in model liquid crystalline materials. Liquid crystals (LCs) encompass a state of soft matter in which properties are typically anisotropic (*5*). Unlike isotropic liquids, LCs exhibit elasticity that enables energy to be stored at rest in strained states, and they form topological defects in confined systems (*5*-*8*).

A series of recent studies of micrometer-sized synthetic particles (e.g., polystyrene or silica) have revealed that the anisotropic viscoelasticity of LCs can generate direction-dependent interparticle forces that lead to formation of complex, self-assembled structures of particles in LCs (*6*-*10*). Both organic and inorganic colloids (spherical and aspherical) have also been shown to interact with topological defects formed in LCs. Although the self-organization of 'passive' colloids in LCs has been well characterized, much less is known about the behaviors of 'active' particles (*11*, *12*) that propel themselves within LCs. Bacteria can be viewed as a promising class of active particles for fundamental studies because, as we demonstrate, they can be genetically engineered to manipulate the magnitude of the propulsive force that they generate in LCs. Here

we note also that many specialized bacteria including *Staphylococcus aureus, Neisseria gonorrhoeae,* Beta-hemolytic strains of *Streptococcus*, *Mycobacterium tuberculosis*, and *Pseudomonas aeruginosa* have been previously shown to colonize biological LCs (*2-4*). In this paper, we move beyond preliminary observations of anisotropic orientation and motion of bacteria in LCs (*13, 14*) to address key issues such as the influence of elastic and motive forces on the self-organization of bacteria, both within the bulk of a LC and at its interfaces. We also explore how the presence of topological defects in LCs can influence the dynamic behaviors of bacteria and how interactions of motile bacteria with regions of LCs that undergo spatial variation in orientation can guide complex cellular trajectories.

To investigate the above-described fundamental issues, we studied the behavior of *Proteus mirabilis* cells suspended in a lyotropic LC that creates an anisotropic viscoelastic microenvironment. *P. mirabilis* is a Gram-negative, rod-shaped γ-proteobacterium that is commonly associated with urinary tract infections and the biofouling of catheters. Guided by environmental cues, *P. mirabilis* cells differentiate into long swarmer cells that have a characteristically high density of flagella that enables them to move through high viscosity fluids and has been hypothesized to play a role in pathogenesis (*15*). Rather than working with swarmer cells per se, we studied *P. mirabilis* cells overexpressing the *flhDC* operon, which encodes the master regulator of flagellum biosynthesis, $FlhD_4C_2$. Overexpressing *flhDC* produces vegetative *P. mirabilis* cells (*P. mirabilis-flhDC*) that have a high density of flagella that resembles swarmer cells, and enables them to move through viscous fluids (*15*). Focusing our studies on *P. mirabilis-flhDC* enabled us to recapitulate the dominant phenotype of swarmers—movement through viscous environments—without the technical complexities of isolating and working with

isogenic populations of these differentiated cells.

For our studies of *P. mirabilis-flhDC* in anisotropic environments, we used aqueous solutions of disodium cromoglycate (DSCG). DSCG (also known as cromolyn) is an example of a lyotropic LC. Aqueous DSCG solutions exhibit nematic LC phases within a particular range of compositions and temperatures due to formation of aggregates of stacked DSCG molecules (*16, 17*). Our choice of DSCG for these studies was primarily guided by its known biocompatibility with several types of cells and bacteria (*18*, *19*). DSCG has also been characterized extensively, including the determination of its phase diagram (*16*, *20*), birefringence (*21*), and elastic constants (*22*). In addition, synthetic LCs are particularly attractive model anisotropic fluids because it is possible to exert spatiotemporal control of the local LC alignment, e.g. through changes in boundary conditions or application of external fields.

## Materials and Methods

### Bacterial strains and cell culture.

*P. mirabilis* strain HI4320 was transformed with plasmid pflhDC to create *P. mirabilis-flhDC.* The plasmid pflhDC contained the *flhDC* genes from *P. mirabilis* inserted into pACYC184 (which contains a gene for chloramphenicol resistance). Empty vector pACYC184 (without *flhDC*) was transformed into HI4320 to obtain wild type vegetative *P. mirabilis*. Both strains were grown in chloramphenicol-resistance nutrient medium consisting of 1% (wt/vol) peptone (Becton, Dickinson, Sparks, MD), 0.5% (wt/vol) yeast extract (Becton, Dickinson), and 1% (wt/vol) NaCl (Fisher Scientific, Fairlawn, NJ) at 30°C in a shaking incubator (*S1*). Saturated overnight cultures were diluted 100-fold in 10 mL of fresh nutrient medium and grown in 150 mL Erlenmeyer flasks at 30°C in a shaking incubator at 200 rpm. We observed that the highest swimming velocity of *P. mirabilis* cells occurred during stationary phase, hence we harvested cells at an absorbance ($\lambda$=600 nm) of ~3.2 and centrifuged. The cells were then washed three times with an aqueous buffer for bacterial motility (0.01 M $KPO_4$, 0.067 M NaCl, $10^{-4}$ M EDTA, 0.1 M glucose, and 0.001% Brig-35, pH 7.0). To obtain non-motile *P. mirabilis* cells, the cells were treated 4% glutaraldehyde for 3 h at 25°C after harvesting.

*E. coli* K-12 strain MG1655 (CGSC #8237) was grown in Luria-Bertani media (LB) (1% tryptone w/v, 0.5% yeast extract w/v, 1% NaCl w/v) at 37°C in a shaker incubator. Saturated overnight cultures were diluted 100-fold in 10 mL of fresh nutrient medium and grown in 150 mL Erlenmeyer flasks at 37°C in a shaking incubator at 200 rpm for 2 hours. These cells were washed as described above for *P. mirabilis* following harvesting.

**Lyotropic LC preparation**

Disodium cromoglycate (DSCG) was purchased from Sigma-Aldrich (Milwaukee, WI) and used as received. Lyotropic LCs containing DSCG were prepared by mixing 15.3 wt% of DSCG with 84.7 wt% of aqueous motility buffer. The mixture was shaken for at least 12 h to ensure complete solubility and homogeneity. Prior to experimentation, the DSCG solution was heated at 65°C for 10 min to avoid possible time dependence of the properties of the mixture (*S2*, *S3*). After cooling the solution to 25°C, a small volume of motility buffer containing bacteria was added to the DSCG mixture producing a final concentration of ~$10^4$ cells/μL. The final concentration of DSCG was 15.0 wt% in all experiments. At this concentration, DSCG forms a nematic LC phase below ~ 27°C and an isotropic phase above ~ 40°C with two-phase coexistence observed within the range of intermediate temperatures (*S4*, *S5*).

**Preparation of imaging chambers**

A glass slide and a glass cover slip were first rubbed unidirectionally multiple times with tissue paper (Kimwipe). We created imaging chambers by adding a small volume (~1 μL) of DSCG solution on top of the rubbed glass slide between two sheets of Mylar film. 6 μm-thick Mylar films were used for all experiments except those in which DSCG solutions were heated to temperatures where nematic and isotropic phases coexisted. For these studies, 18 μm-thick Mylar films were used instead. A rubbed glass cover slip was then placed on top of the Mylar and the chamber was sealed with epoxy to prevent water evaporation (**Fig. S1**). The sample was prepared such that the rubbed surfaces of the glass substrates were both in contact with the DSCG solution with rubbing directions antiparallel to each other. The sample was briefly (~10 s) heated to 42°C into the isotropic phase of DSCG to mitigate any flow-induced alignment of

the nematic LC before cooling back to room temperature. Using this technique, large regions (in excess of 100 μm × 100 μm) of the LC phase of DSCG (at 25°C) exhibited an orientation that was parallel to the surface with an azimuthal alignment in the direction of rubbing (**Fig. S1**). We confirmed that the alignment of the nematic LC in these regions was parallel to the direction of rubbing by inserting a quarter wave plate into the optical path of a microscope and analyzing the appearance of the sample between crossed polars (*S6*). Imaging chambers were used within 3 h of their preparation. Particular care was taken when analyzing the populations of multi-cellular complexes of motile and non-motile *P. mirabilis-flhDC* cells to disperse the cells in DSCG for the same amount of time prior to imaging.

**Microscopy**

We optically imaged cells housed within imaging chambers using a Nikon Eclipse Ti inverted microscope equipped with crossed polarizers and a Photometics CoolSNAP HQ2 CCD camera (Tucson, AZ) using a Nikon Plan Apo λ, 100X/1.45 oil objective lens. Videos consisting of 400 frames were collected with the EM gain off and with a 100 ms exposure time (10 frames/sec). Images of cells were collected using NIS Element. For non-motile cells, bright field and crossed polar images were collected for the same field of view. A thermoplate (Tokai Hit, Japan) and 100X objective heater (Bioptichs, PA) were used to control the temperature of the samples during experiments. An Olympus BX60 microscope equipped with crossed polarizers was also used to analyze the imaging chambers. Images were captured using a digital camera (Olympus C-2040 Zoom) mounted on the microscope and set to an f-stop of 2.8 and a shutter speed of 1/125 sec.

**Bacterial motility data analysis**

Microscopy data for motile cells were analyzed using the MATLAB computing environment (MathWorks, Natick, MA, USA) by identifying the centroid of each bacterium in successive frames and grouping those points together to create a cell trajectory. We combined the position of the cell at each interval in a cell track with the CCD frame rate to determine cell velocity. Using this script, we determined the length and position of each cell and the average cell velocity over the entire track. Tracks that were shorter than 25 frames were discarded. ImageJ software was used to calculate the angular dispersion of non-motile cell populations relative to the direction of rubbing as well as the distance between associated non-motile cells.

**Rheology**

An Advanced Rheometric Expansion System (ARES) (TA Instruments, Rheometric Scientific, Piscataway, NJ) with cone and plate type geometry (cone diameter 50 mm; cone angle 0.04 rad) was used to measure the effective viscosity of the DSCG solution. Steady shear rate sweeps were performed at room temperature at shear rates between $10^{-3}$ and $10^{3}$ $s^{-1}$. A gap of 0.0508 mm between the plate and the center of the cone was used such that DSCG solution fully filled the space between the plates, with excess material extended beyond the plates.

**Statistical analysis.**

All experimentally determined values have been reported in the text and figures with associated standard errors.

## Results and Discussion

### Anisotropic motion and orientation of cells in nematic DSCG phases

We first investigated whether elastic interactions with the nematic LC phase of DSCG solutions (15 wt%) in aqueous motility buffer induced suspended bacteria to move anisotropically. At this concentration, DSCG forms a nematic LC phase below ~ 27°C and an isotropic phase above ~ 40°C with coexistence of two phases at intermediate temperatures (*16*, *20*). All of the experiments described in this manuscript were performed in 15 wt% DSCG. We confined suspensions of bacterial cells in DSCG solutions between two rubbed glass substrates. The surfaces of the glass substrates were oriented such that direction of rubbing on each substrate was antiparallel. When confined between the rubbed surfaces, large regions of the LC phase of DSCG (at 25°C) exhibited an orientation that was parallel to the surface with an azimuthal alignment in the direction of rubbing. We confirmed that the alignment of the nematic LC was parallel to the direction of rubbing by inserting a quarter wave plate into the optical path of a microscope and analyzing the appearance of the sample between crossed polars (Fig. S1) (*23*).

Initial experiments with *E. coli* strain MG1655 revealed limited motility in nematic phases of DSCG (average velocity $\overline{V} \sim 1.2$ +/- 0.4 μm/s), which made it challenging to differentiate between motile and non-motile cells. With few exceptions, past studies have demonstrated that many types of bacteria are unable to move through fluids with $\mu > 0.06$ Pa·s (e.g. the motility of *Escherichia coli* strain KL227 ceases at $\mu = 0.06$ Pa·s) (*24*). Nematic LCs possess direction-dependent (Miesowicz) shear viscosities with the direction of lowest viscosity being parallel to the director (*25-27*). Experimental determination of Miesowicz viscosities of lyotropic LCs is difficult because general and facile methods to manipulate the surface anchoring of lyotropic LC

phases do not exist, so we performed rheological measurements of the DSCG solution at 25°C and measured an effective viscosity of $\mu \sim 1$ Pa·s. Since *E. coli* cells are not adapted for motility in fluids of such high viscosity, we investigated motile strains of *P. mirabilis* that were engineered to overexpress *flhDC* and enable cells to move through viscous fluids with a kinematic viscosity, $\mu < 8.34$ Pa·s (*15*). The aspect ratio of the engineered cells (k = L/2R) was ~3, closely matching vegetative *P. mirabilis* cells that did not overexpress *flhDC*. We measured the *P. mirabilis-flhDC* cells to move through DSCG solutions with a much higher velocity ($\overline{V}$ = 8.8 +/- 0.2 μm/s) than both the *E. coli* cells and vegetative *P. mirabilis* cells that did not overexpress *flhDC* ($\overline{V}$ = 0.2 +/- 0.1 μm/s) (Fig. 1*A*).

When we analyzed the motion of *P. mirabilis-flhDC* cells dispersed in nematic DSCG solution (Video S1), we observed cells moving preferentially along the direction of LC alignment (*13*, *14*), as illustrated by the representative trajectories shown in Fig. 1*B*. The mean-squared displacement for *P. mirabilis-flhDC* cells parallel to the nematic LC director (x-direction) was approximately two orders of magnitude greater than in the perpendicular direction (Fig. 1*D*). In contrast, *P. mirabilis-flhDC* cells suspended in an isotropic DSCG solution (achieved by equilibrating the solution at 42°C) exhibited a comparable velocity of $\overline{V}$ = 8.1 +/- 0.3 μm/s without a directional bias (Fig. 1*C* and *D*; Video S2). By comparing the average velocity of motile *P. mirabilis-flhDC* in nematic DSCG to previous measurements of *P. mirabilis-flhDC* motility in solutions of known viscosity (*15*), we estimate the viscous drag force that is balanced by the flagella-derived forces generated by the engineered bacteria to be tens of pN in 15 wt% DSCG.

We hypothesized that the interactions between *P. mirabilis-flhDC* cells mediated by the elasticity of the LC would be dependent on the anchoring of the LC on the surface of the bacteria and the resulting strain in the LC. To assess this prediction, we quantified the distribution of orientations of non-motile *P. mirabilis-flhDC* cells in both the nematic and isotropic phases of DSCG solutions and characterized the ordering of the LC near the cells by using polarized light microscopy. Treating *P. mirabilis-flhDC* cells with 4% glutaraldehyde rendered them non-motile. While non-motile *P. mirabilis-flhDC* cells suspended in an isotropic DSCG solution exhibited no preferential orientational alignment (Fig. S2), we measured the long axes of non-motile *P. mirabilis-flhDC* cells to preferentially align parallel to the far-field LC director in nematic DSCG (Fig. 1*E* and *H*) and we observed four small regions with a bright optical appearance near the poles of each bacterium (Fig. 1*F*), both which are consistent with tangential anchoring of the LC at the bacterial surface (Fig. 1*G*). We calculated that shear forces generated by motile bacteria should not perturb this local ordering of LC because the Ericksen number ($\mathrm{Er} = \eta\overline{\mathrm{V}}\mathrm{R}/\mathrm{K}$) for the motion of *P. mirabilis-flhDC* cells in DSCG is < 1 (*25*). If the tangential surface anchoring of the LC on the surface of *P. mirabilis-flhDC* was strong, the orientation-dependent energy of interaction of the LC and the rod-shaped bacterium (length L = 3 μm, radius R = 0.5 μm) would be $U_{elastic} = 2\pi K\theta^2 L/\ln(2L/R)$ (*6, 13, 28, 29*), where $\theta$ is the angle (in radians) between the director of the LC and long-axis of the bacterium and *K* is the elastic constant of the LC (*K* = 10 pN) (*22*), where for simplicity the elastic constants for splay, twist, and bend are assumed to be equal in magnitude allowing the strain of the LC to be described by a single elastic constant. This analysis leads to the prediction that even slight deviations of the bacterial long axis from the nematic director would be highly unfavorable (e.g., $U_{elastic} \sim 90\mathrm{kT}$ for $\theta = 4°$). In contrast, we measured a significant number of bacteria to be oriented away from

the far-field director (35% of cells in nematic DSCG were recorded with $\theta \geq 4°$), suggesting that the tangential anchoring of the LC on the surface of the bacteria is likely weak [a conclusion which receives support from additional observations reported below; we note also that weak, tangential anchoring of DSCG at surfaces has been reported elsewhere (*30, 31*)]. In addition, we note that the distribution of flagella over the surface of *P. mirabilis-flhDC* may not be uniform (*15*) and thus may contribute to the distribution of orientations in Fig. 1*H*.

**Dynamic association of dispersed cells within a nematic LC**

Past studies have demonstrated that the elasticity of LCs, and topological defects that form about passive particles in LCs, mediate particle-particle interactions that result in self-assembly of the particles (*7-10, 32)*. For example, it has been demonstrated that spherical and ellipsoidal colloids with tangential surface anchoring form well-defined chains (for spherical colloids the vector that joins the particle centers is offset 30° from the far-field director) (*33*). We observed the above-described strain induced in the LC by non-motile and motile *P. mirabilis-flhDC* cells similarly leads to inter-bacterial forces that resulted in the formation of multi-cellular complexes. Fig. 2*A* provides a sequence of snapshots which demonstrates the formation of a linear chain of two motile *P. mirabilis-flhDC* cells (Video S3). At t = 3.7 s, the two bacteria, which had previously been swimming towards one another, associate together into a chain. At later time points, the bacteria move within the LC together, retaining this state of association. We only observed the end-on-end association of *P. mirabilis-flhDC* cells in the nematic phase of the DSCG solution (they do not form within the isotropic phase). We also observed the closest approach of the surfaces of the motile bacteria to be 0.26 +/- 0.02 μm, indicating the existence of a short-range repulsion which we hypothesize originates from steric and/or electrostatic interactions between

cells due to the presence of the lipopolysaccharide that decorates the outer leaflet of the bacterial membrane. The role of the elasticity of the LC in mediating the inter-bacterial interactions was confirmed by measurement of the relative orientations of the centroids of non-motile bacterial cells within chains (Fig. 2*C*). An angle of 5.5 +/- 0.8° with respect to the far-field LC director was measured for chains of non-motile *P. mirabilis-flhDC* cells, consistent with theoretical predictions for elasticity-mediated interactions of ellipsoidal microparticles with aspect ratios matching *P. mirabilis-flhDC* cells (*32*). We found that linear chains of motile *P. mirabilis-flhDC* cells were instead oriented at an angle of 3.3 +/- 0.5° from the far-field director, an observation which likely reflects the drag forces generated by the motion of the swimming bacteria. Crossed-polar images confirm the quadrupolar symmetry of the nematic director near the surface of the non-motile bacteria within these chains (Fig. 2*D*).

Consistent with past studies of assemblies of passive particles, non-motile bacteria did not dissociate in nematic DSCG solutions. However, we frequently observed motile bacteria within multi-cellular assemblies to separate from each other with trajectories that followed the LC director (Fig. 2*E*; Videos S4 and S5). The dissociation of the bacteria via flagella-derived forces leads to differences in the populations of multi-cellular assemblies (monomers, dimers, trimers and tetramers) found in LC suspensions of motile and non-motile bacteria. For example, as seen in Fig. 2*F*, the population of motile monomers is higher by a factor of two relative to non-motile monomers, whereas the population of non-motile dimers is enriched relative to motile dimers. The role of flagella-derived forces in biasing the size-distribution of multi-cellular bacterial complexes is evidenced further in the populations of motile and non-motile trimers and tetramers

in Fig. 2*F*. We estimated the magnitude of the LC-mediated attractive force acting between bacteria with surface anchoring energy W and quadrupolar distortions of the director as

$$F_{elastic} \propto C\left(W^2R^2/K\right)\left(\frac{2R}{d}\right)^6$$

where *d* is the distance between the surfaces of the two rod-shaped bacteria (0.26 +/- 0.02 μm, see above), and C is a coefficient of order one (*13, 34, 35*). The parameter W (so-called "anchoring strength") quantifies how strongly LCs are held in a particular orientation at a surface. Guided by observations reported above indicating weak anchoring ($WR/K \sim 1$) of LCs on the surfaces of the bacteria [and reports of weak anchoring of DSCG at other interfaces (*30, 31*)], we used $W \sim 10^{-5}$ J/m$^2$ to calculate $F_{elastic} \sim 10$ pN at d = 0.26 +/- 0.02 μm. Our observation that $F_{elastic}$ is comparable to our estimate of the propulsive forces generated by the flagella of *P. mirabilis-flhDC* cells [tens of pN (*36*), see above] provides additional support for the conclusion that the population of multi-cellular assemblies shown in Fig. 2*F* (for motile bacteria) belong to non-equilibrium states of the system that arise from the interplay of flagella-derived dissociative forces and elasticity-mediated attractive forces in the LC.

**Influence of interfaces of nematic DSCG on behavior of cells**

Passive micrometer-sized particles adsorb strongly (irreversibly) to interfaces between immiscible isotropic-LC phases and experience rheological environments that lead to anisotropic diffusion in the plane of the interface (*27*). At temperatures between 27°C and 40°C, the DSCG solution used in our experiment exhibited coexisting nematic and isotropic (N-I) phase domains. In particular, upon quenching samples from 42°C to 35°C, nematic domains with an elongated and cusped shape (tactoids) formed within a continuous isotropic phase (Fig. 3*A* and *F*).

Conversely, heating from 25°C to 32°C led to formation of isotropic tactoid domains within a continuous nematic phase (Fig. S3). These domains generally nucleated at and remained attached to one of the glass substrates. We observed non-motile bacteria to attach to and remain immobile at the N-I interface of the tactoids. In contrast, motile bacteria adsorbed to the N-I interface and then moved along the N-I interface as well as the triple phase (N-I-glass substrate) contact line with a velocity ($\overline{V}$ = 14.0 +/- 0.8 μm/s) slightly larger than that which we measured in bulk nematic and isotropic phases. We found that both motile and non-motile *P. mirabilis-flhDC* cells adsorbed at the N-I interface adopted orientations parallel to the local director [LCs are anchored tangentially at the N-I interface (Fig. 3*B*)]. Fig. 3*C* depicts the trajectory of a *P. mirabilis-flhDC* cell moving along the N-I interface of a nematic tactoid projected onto the glass substrate (also the position of the focal plane). We note that the cell moves out of the focal plane as it moves along the interface of the hemispherical tactoid. A comparison of Figs. 3*B* and 3*C* reveals that the bacterial trajectory maps out the interfacial director profile of the tactoid (Video S6). In contrast to non-motile cells, motile *P. mirabilis-flhDC* cells often escaped their association with the interface and entered the bulk isotropic phase (Fig. 3*C-E*). Interestingly, two-thirds (N=170) of the motile bacteria that escaped from the interface did so at the cusped poles of the tactoids, where a LC topological defect is present [a surface point defect with topological charge k = +1, often called a boojum (*9*)]. We hypothesize that escape occurs most commonly at the boojums because motile bacteria are focused to these points by the convergence of the LC director profile (Fig. 3*B*); for bacteria not moving along the three-phase contact line, a component of force generated by the bacteria will be directed normal to the contact line near the boojum (away from the defects, the parallel orientation of the bacteria at the interface results in flagella-derived forces that largely act in the tangential direction).

LC-mediated interactions organize particles into hexagonal and chain-type two-dimensional assemblies at LC-water and LC-air interfaces (*37*-*39*). We also observed that bacteria assembled into chains at N-I interfaces (Fig. 3*F*-*J*; Video 7). Similar to the chains of bacteria formed in bulk nematic LCs, bacteria within these chains positioned at the interface were separated by a small distance. Formation of these chains is consistent with previous theoretical calculations for spherical microparticles at N-I interfaces with tangential/planar LC anchoring (*40*). The end-on-end assemblies formed by motile *P. mirabilis-flhDC* cells at the N-I interfaces were dynamic and reversible.

**Interaction of cells with a defect in the LC director field**

LCs are a particularly interesting class of anisotropic media in which to investigate bacterial dynamics because the local alignment of nematic LCs can be manipulated both spatially and temporally and topological defects can be created by manipulating LC anchoring at boundaries. We sought to investigate further how the motility of bacteria dispersed within nematic LC would be influenced by strain stored within a LC in the vicinity of a topological defect. We confined a nematic solution of DSCG between glass slides that had not been rubbed. The resulting film of DSCG exhibited spatial variation in the azimuthal orientation of the nematic director and the presence of defects in the LC. Fig. 4*A* shows the trajectory of a bacterium in the vicinity of a topological defect (disclination line) of strength k = +1/2 within the LC phase (Video S8). The trajectory of the cell is superimposed on an image of the LC field taken with crossed polars. Two optically bright brushes are apparent that emanate from the central defect, indicative of regions of the LC with azimuthal orientations that are not parallel to either polarizer. Comparison of

Figs. 4*A* and 4*B* reveals that the *P. mirabilis-flhDC* cell traces a path around the disclination line in which the long axis of the bacterium remains parallel to the local director during the transit. More generally within these spatially complex LC phases, we found that the direction of cell motion was always parallel to the local director when the curvature of the director was comparable to or larger than the size of the bacterium. These results suggest that the trajectories of motile bacteria in anisotropic LCs can be manipulated precisely by patterning glass substrates to provide well-defined variations in the orientation of the LC director.

**Conclusions**

In summary, our results reveal that bacteria can be genetically engineered to serve as model "active" particles in LCs with which to unmask dynamic phenomena that emerge from the interplay of local propulsive forces and anisotropic viscoelastic environments. In particular, we observe the forces generated by the flagella of *P. mirabilis-flhDC* cells to be comparable in magnitude to those that result from the elasticity-induced interactions between cells in LCs. This leads to the observation of the *reversible* assembly of motile bacteria within LCs and the demonstration that bacteria can be used to overcome the kinetic trapping of passive particles in aggregates due to strong LC-mediated forces (*7-10*). More broadly, our studies reveal that motile bacteria in LCs are a versatile system for investigations of self-organization that result from dissipative processes, for elucidation of general design principles for active soft matter (including systems containing synthetic particles driven by catalytic reactions *(11,12)*), and potentially for studies of the emergence of cooperative behaviors of populations of bacteria at high concentrations. The observation that bacteria can be either focused to defects or guided around defects in a manner that depends on the topological strength of the defects provides new insight into the ways in which anisotropic environments can influence bacterial behaviors. Because confinement of LCs, or external electric and magnetic fields, can be used to manipulate LCs and their defects, our results also reveal that LCs are a promising class of materials with which to actively control bacterial behavior (e.g., to dynamically focus isolated bacteria to a specific location in a system for analysis).

**Acknowledgements**

This chapter was prepared as a Full Paper reporting original research in the journal Soft Matter. Peter Mushenheim contributed equally to performing and analyzing the experiments and preparing the manuscript. Hannah Tuson assisted in preliminary experiments and taught Peter and I how to use the MATLAB bacteria tracking script.

This work was supported by the National Science Foundation (under awards DMR-1121288 (MRSEC), CBET-0754921, and MCB-1120832), the National Institutes of Health (CA108467, AI092004, and 5T32GM08349), the Army Research Office (W911-NF-11-1-0251 and W911-NF-10-1-0181), and the United States Department of Agriculture (WIS01594).

**Fig. 1.** Configuration of LC around bacteria in nematic LC and resulting bacterial alignment and anisotropic motion. (*A*) Average velocities of *P. mirabilis-flhDC* cells in nematic DSCG solutions (15 wt%) at 25°C. (*B)* Superimposed trajectories of *P. mirabilis-flhDC* in nematic DSCG solutions at 25°C. The LC director was oriented along the x-axis (in the direction of rubbing of the glass slides). (*C*) Superimposed representative trajectories of *P. mirabilis-flhDC* in isotropic phases of DSCG at 42°C. (*D*) Plot of the mean-square displacement of *P. mirabilis-flhDC* calculated from analysis of 139 trajectories (25°C) and 75 trajectories (42°C). The velocities of *P. mirabilis-flhDC* cells in DSCG solution were comparable in magnitude at 25°C ( $\overline{V}$ = 8.8 +/- 0.2 μm/s) and 42°C ($\overline{V}$ = 8.1 +/- 0.3 μm/s). (*E*, *F*) Bright field and crossed polars images, respectively of non-motile *P. mirabilis-flhDC* cells dispersed in nematic DSCG solution at 25°C. In the crossed polars image, not all of the bright optical regions near the poles of the bacterium are equal in intensity because the bacterium was not aligned exactly with a polarizer. The double-headed solid arrows in *F* indicate the positions of the polarizers. (*G*) Schematic representation of the LC director profile that results from weak, tangential anchoring of the LC on the surface of *P. mirabilis-flhDC* cells. (*H*) Distribution of angles between the rubbing direction of the glass slides and the long axis of *P. mirabilis-flhDC* cells in DSCG solution at 25°C (nematic) and 42°C (isotropic). The scale bar in E is 10 μm. Values are reported with associated standard errors.

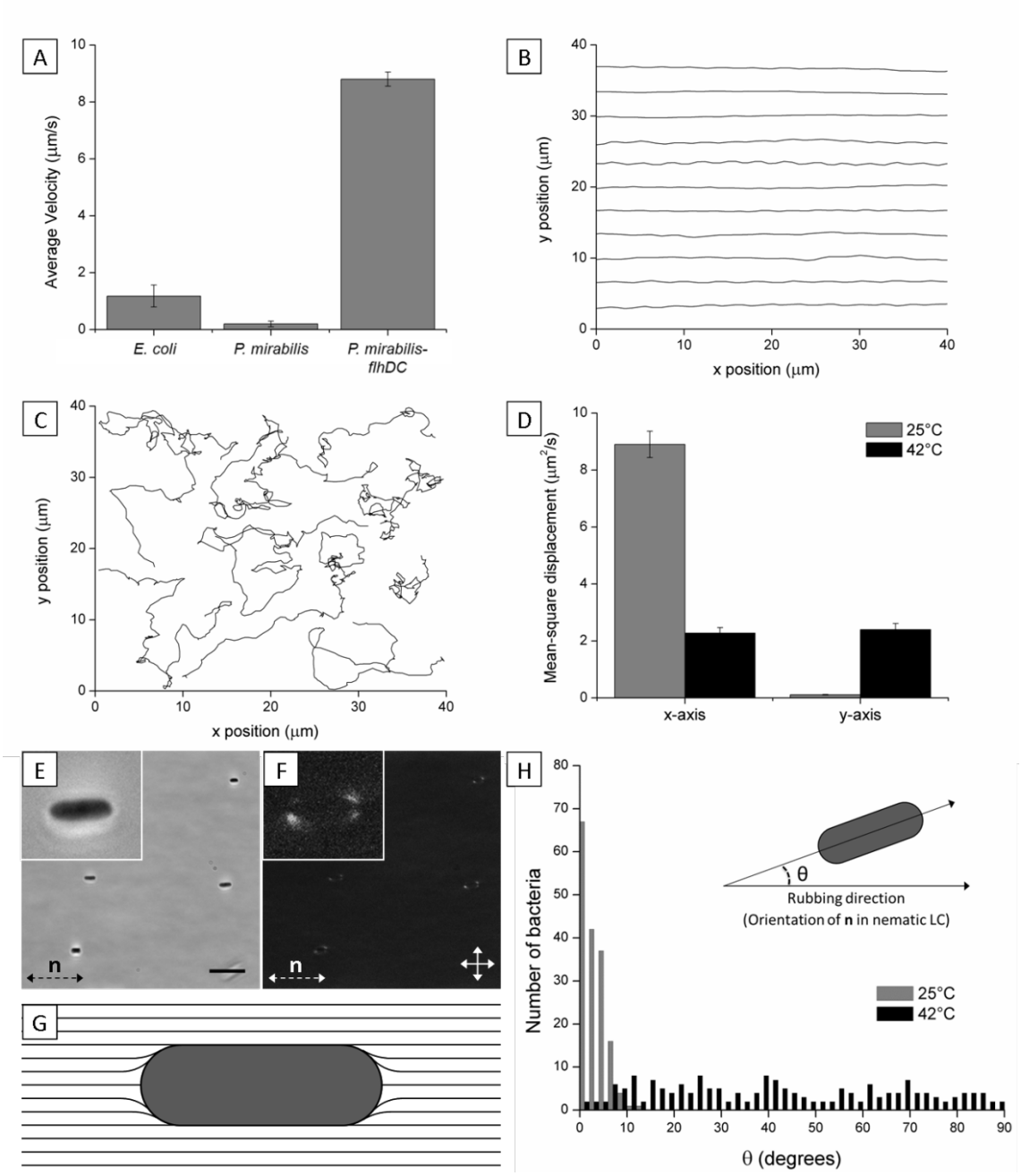
A
Average Velocity (μm/s)
E. coli
P. mirabilis
P. mirabilis-flhDC
B
y position (μm)
x position (μm)
C
y position (μm)
x position (μm)
D
Mean-square displacement (μm²/s)
25°C
42°C
x-axis
y-axis
E
n
F
n
G
H
Number of bacteria
θ
Rubbing direction
(Orientation of n in nematic LC)
25°C
42°C
θ (degrees)

**Fig. 1**

**Fig. 2.** Dynamic association of motile bacteria in nematic LC. (*A*) Sequence of images (bright field) showing end-on-end association of two motile *P. mirabilis-flhDC* cells in nematic DSCG solution (15 wt%) at 25°C. Dotted arrows indicate the velocity of the bacterial cells (see calibration in t = 1.5s). (*B*) Plot of the velocities of the *P. mirabilis-flhDC* cells shown in *A* before and after association into the chain. (*C*) Bright field and (*D*) crossed polars images of a chain of three non-motile *P. mirabilis-flhDC* cells in nematic DSCG solution (15 wt%) at 25°C. (*E*) Sequence of images (bright field) showing both the association and dissociation of two motile bacteria in nematic DSCG solution at 25°C. (*F*) Populations of bacteria in multi-cellular complexes formed in nematic DSCG solution by non-motile (black) and motile (gray) bacteria. The total number of cells in both populations is 400. Scale bars are 5 μm.

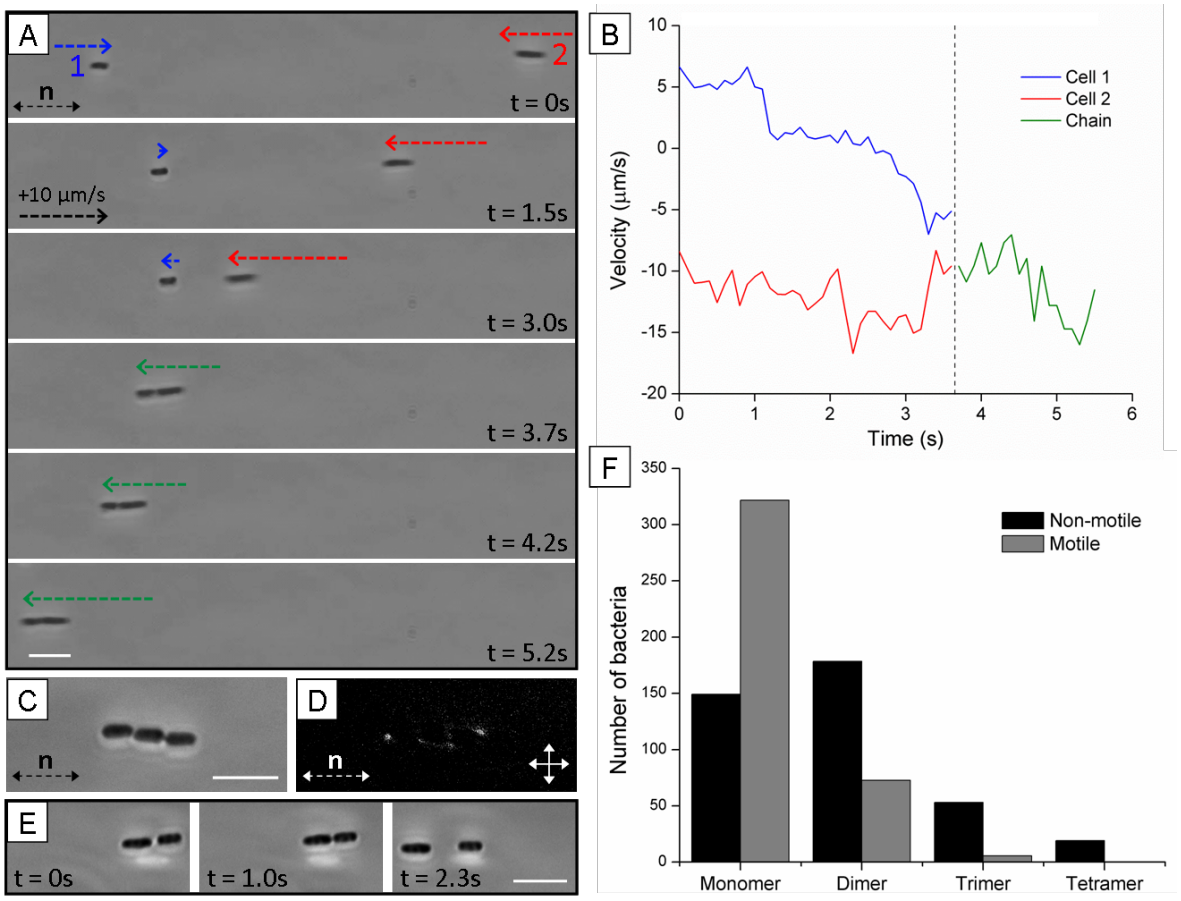
A
1
2
n
t = 0s
+10 µm/s
t = 1.5s
t = 3.0s
t = 3.7s
t = 4.2s
t = 5.2s
B
Cell 1
Cell 2
Chain
Velocity (µm/s)
Time (s)
C
n
D
n
E
t = 0s
t = 1.0s
t = 2.3s
F
Non-motile
Motile
Number of bacteria
Monomer
Dimer
Trimer
Tetramer

**Fig. 2**

**Fig. 3**. Interactions of bacteria with nematic LC-isotropic interfaces. (*A*) Optical micrograph (crossed polars) of a nematic LC domain of DSCG (tactoid) that partially wets a glass substrate. The tactoid formed within a continuous isotropic phase containing 15 wt% DSCG upon quenching samples from 42°C to 35°C. (*B*) Schematic representation of the LC director profile of the tactoid in *A*. (*C*) Bright field micrograph of a nematic tactoid on which the trajectory of a motile *P. mirabilis-flhDC* cell (indicated by an arrow) adsorbed to the N-I interface is indicated. Note that the cell briefly leaves the imaging focal plane as it moves along the interface of the lens-shaped tactoid. A comparison of this trajectory with the LC director profile in *B* reveals that the motion of the bacterium largely follows the interfacial nematic director field. (*D*, *E*) Bright field micrographs of a motile cell that escapes from the N-I interface at a boojum (topological defect at the cusped pole) of the tactoid. In *D*, the cell is oriented towards the viewer. (*F-J*) Sequence of images (bright field and crossed polars) showing end-on-end association of two motile *P. mirabilis-flhDC* cells (indicated by an arrow) adsorbed to the N-I interface (near the triple-phase contact line) of a tactoid. Scale bars are 10 μm.

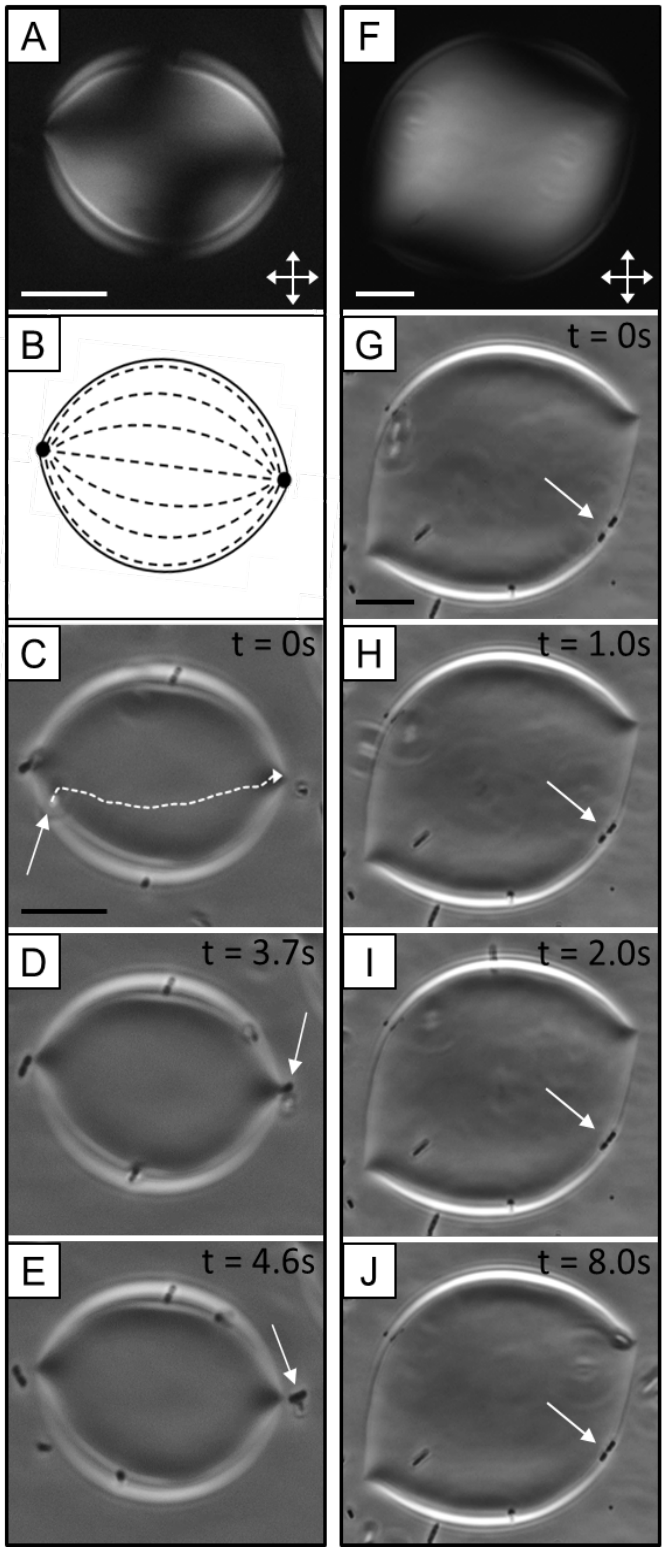


**Fig. 3**

**Fig. 4**. Bacteria motility near a LC defect. (*A*) The trajectory of a motile *P. mirabilis* cell within bulk nematic DSCG solution (15 wt%) near a disclination line of strength k = +1/2 is superimposed on an optical image (crossed polars) of the LC. The bacterium is highlighted in red and the dot indicates the origin of the trajectory. (*B*) Schematic representation of the LC director profile corresponding to the image in *A*. The black dot represents the cross-section of the core of the disclination line that is oriented towards the viewer. The scale bar in *A* is 10 μm.

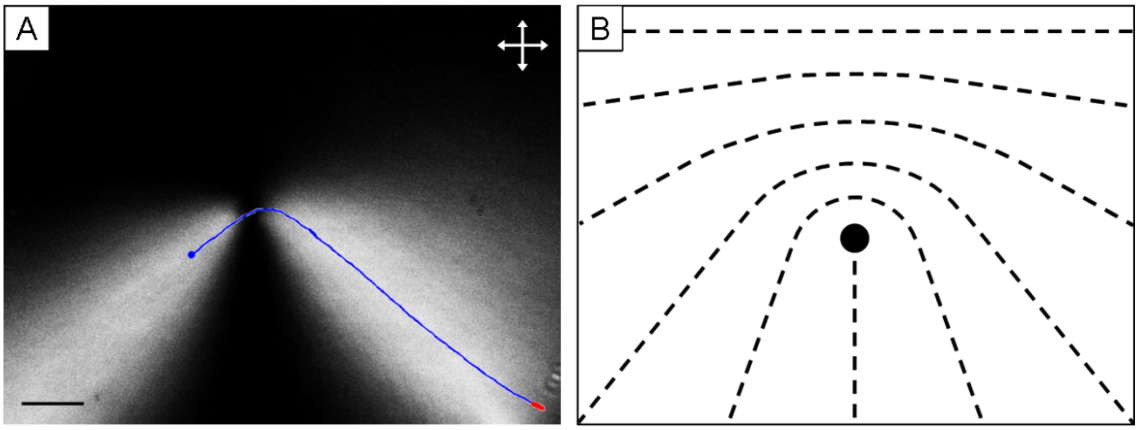


**Fig. 4**

**Fig. S1.** Experimental setup. (*A*) A schematic illustration depicting imaging chambers used to analyze bacterial cells in LC solutions. The double-headed arrows indicate the direction of rubbing along the surface of the glass slides. The LC director profile is indicated by the dotted lines. (*B*, *C*) Polarized light micrographs of the experimental cell aligned (*B*) parallel and (*C*) 45° to one of the crossed polarizers. We confirmed that the alignment of the nematic LC was parallel to the direction of rubbing by inserting a quarter wave plate into the optical path of a microscope and analyzing the appearance of the sample between crossed polars. The scale bar in *B* is 200 μm.

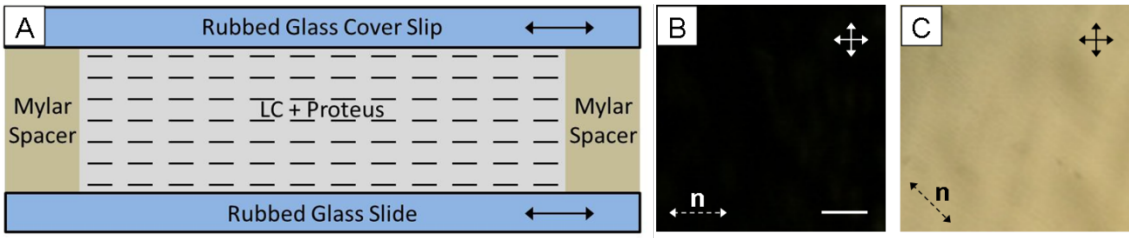


**Fig. S1**

**Fig. S2.** Bright field micrograph showing non-motile *P. mirabilis-flhDC* cells in an isotropic DSCG solution at 42°C. The scale bar is 10 μm.

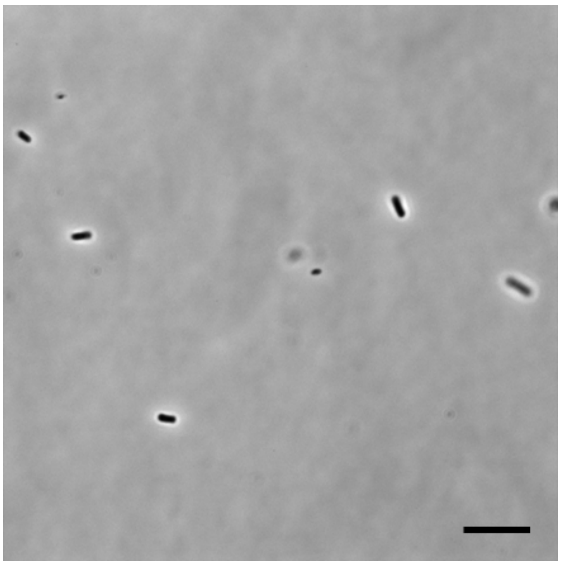

**Fig. S2**

**Fig. S3.** Bright field and crossed polars images, respectively, of motile *P. mirabilis-flhDC* cells adsorbed at the interface of domains of isotropic DSCG (tactoids) that formed on the glass substrate following heating of a nematic phase of DSCG (15 wt%) from 25°C to 32°C. The scale bar in *A* is 10 μm.

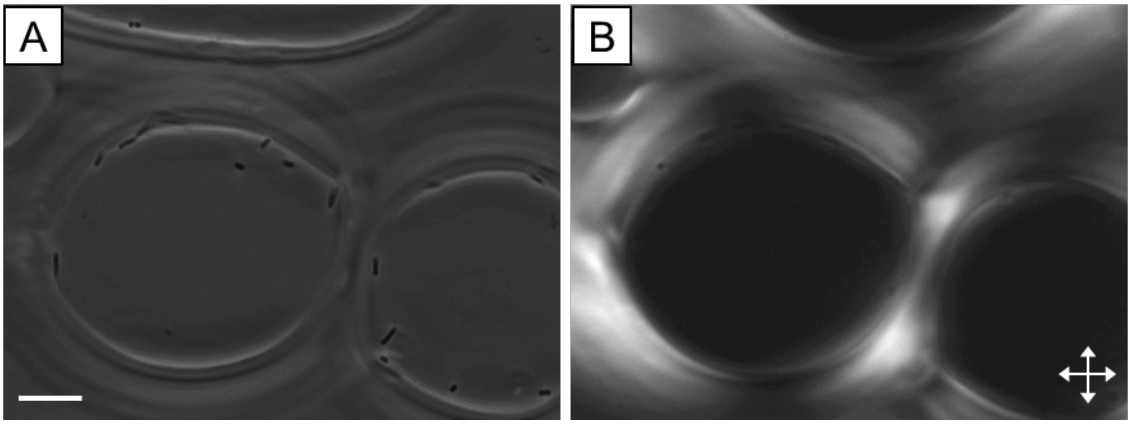


**Fig. S3**

**Video Captions**

**Video S1.** Bright field optical microscopy video showing anisotropic motion of *P. mirabilis-flhDC* cells in 15 wt% DSCG at 25°C (nematic phase). The LC director is aligned in the x-direction (horizontal direction of movie). Scale bar = 10 μm.

**Video S2.** Bright field optical microscopy video depicting isotropic motion of *P. mirabilis-flhDC* cells in 15 wt% DSCG at 42°C (isotropic phase). Scale bar = 5 μm.

**Video S3.** Bright field optical microscopy video which demonstrates the formation of a linear chain of two motile *P. mirabilis-flhDC* cells in 15 wt% DSCG at 25°C (nematic phase). Scale bar = 5 μm.

**Video S4.** Bright field optical microscopy video depicting the elasticity-mediated formation and subsequent dissociation of a linear chain of motile *P. mirabilis-flhDC* cells in 15 wt% DSCG at 25°C (nematic phase). Scale bar = 5 μm.

**Video S5.** Bright field optical microscopy video in which a linear chain of motile *P. mirabilis-flhDC* cells in 15 wt% DSCG at 25°C dissociates (nematic phase). Scale bar = 5 μm.

**Video S6**. Bright field optical microscopy video in which the trajectories of motile *P. mirabilis-flhDC* cells adsorbed at the N-I interface largely map out the interfacial director profile of the

tactoid. Additionally, bacteria can be observed escaping the interface at the cusped poles of the tactoids where a boojum is present. Scale bar = 10 μm.

**Video S7**. Bright field optical microscopy video which demonstrates the formation of a chain of motile *P. mirabilis-flhDC* cells adsorbed at the N-I interface. Scale bar = 10 μm.

**Video S8.** Bright field optical microscopy video depicting the motion of a *P. mirabilis-flhDC* cell in the vicinity of a topological defect (disclination line) of strength k = +1/2. See Fig. 4A for a corresponding crossed polars image of the field of view. The bacterium traces a path around the disclination line in which the long axis of the cell remains parallel to the local director during the transit. Scale bar = 10 μm.

**References**


1. Fontes DE, Mills AL, Hornberger GM, Herman JS (1991) Physical and chemical factors influencing transport of microorganisms through porous media. *Appl Environ Microbiol*, 57:2473-2481.

2. Shaw T, Winston M, Rupp CJ, Klapper I, Stoodley P (2004) Commonality of elastic relaxation times in biofilms. *Phys Rev Lett*, 93:098102.

3. Madoff LC, Thaler SJ, Maguire JH (2005) in *Harrison's Principles of Internal Medicine*, eds Kasper DL, Braunwald E, Fauci AS, Hauser SL, Longo DL, Jameson JL (McGraw-Hill, New York) p. 2050.

4. Flemming H-C, Wingender J (2010) The biofilm matrix. *Nat Rev Microbiol*, 8:623-633.

5. Rey AD (2010) Liquid crystal models of biological materials and processes. *Soft Matter*, 6:3402-3429.

6. Lapointe C, et al. (2004) Elastic torque and the levitation of metal wires by a nematic liquid crystal. *Science*, 303:652-655.

7. Tkalec U, Škarabot M, Muševič I (2008) Interactions of micro-rods in a thin layer of a nematic liquid crystal. *Soft Matter,* 4:2402-2409.

8. Musevic I, Škarabot M, Tkalec U, Ravnik M, Žumer S (2006) Two-dimensional nematic colloidal crystals self-assembled by topological defects. *Science*, 313:954-958.

9. Poulin P, Stark H, Lubensky TC, Weitz DA (1997) Novel colloidal interactions in anisotropic fluids. *Science*, 275:1770-1773.

10. Škarabot M, et al. (2008) Interactions of quadrupolar nematic colloids. *Phys Rev E*, 77:031705.

11. Paxton WF, et al. (2004) Catalytic nanomotors: Autonomous movement of striped nanorods. *J. Am Chem Soc*, 126:13424-13431.

12. Paxton WF, Sundararajan S, Mallouk TE, Sen A (2006) Chemical locomotion. *Angew Chem Int Ed Engl*, 45:5420-5429.

13. Smalyukh II, Butler J, Shrout JD, Parsek MR, Wong GCL (2008) Elasticity-mediated nematiclike bacterial organization in model extracellular DNA matrix. *Phys Rev E*, 78:030701.

14. Kumar A, Galstian T, Pattanayek SK, Rainville S (2013) The motility of bacteria in an anisotropic liquid environment. *Molecular Crystals and Liquid Crystals*, 574:33-39.

15. Tuson HH, Copeland MF, Carey S, Sacotte R, Weibel DB (2013) Flagella density regulates *Proteus mirabilis* swarmer cell motility in viscous environments. *J Bacteriol*, 195:368-377.
16. Hartshorne NH, Woodard GD (1973) Mesomorphism in the system disodium chromoglycate-water. *Mol Cryst Liq Cryst*, 23:343-368.

17. Lydon J (2010) Chromonic review. *J Mater Chem*, 20:10071-10099.

18. Cheng L-L, Luk Y-Y, Murphy CJ, Israel BA, Abbott NL (2005) Compatibility of lyotropic liquid crystals with viruses and mammalian cells that support the replication of viruses. *Biomaterials*, 26:7173-7182.

19. Shiyanovskii SV, et al. (2005) Lyotropic chromonic liquid crystals for biological sensing applications. *Mol Cryst Liq Cryst*, 434:587-598.

20. Lee H, Labes MM (1983) Phase diagram and thermodynamic properties of disodium cromoglycate-water lyomesophases. *Mol Cryst Liq Cryst*, 91:53-58.

21. Nastishin YA, et al. (2005) Optical characterization of the nematic lyotropic chromonic liquid crystals: Light absorption, birefringence, and scalar order parameter. *Phys Rev E*, 72:041711.

22. Nastishin YA, Neupane K, Baldwin AR, Lavrentovich OD, Sprunt S (2008) Elasticity and viscosity of a lyotropic chromonic nematic studied with dynamic light scattering. *Electronic-Liquid Crystal Communications*, http://arxiv.org/abs/0807.2669.

23. Luk Y-Y, et al. (2003) Using liquid crystals to amplify protein−receptor interactions: Design of surfaces with nanometer-scale topography that present histidine-tagged protein receptors. *Langmuir*, 19:1671-1680.

24. Greenberg EP, Canale-Parola E (1977) Motility of flagellated bacteria in viscous environments. *J Bacteriol*, 132:356-358.

25. Stark H, Ventzki D (2001) Stokes drag of spherical particles in a nematic environment at low Ericksen numbers. *Phys Rev E*, 64:031711.

26. Koenig GM, et al. (2009) Single nanoparticle tracking reveals influence of chemical functionality of nanoparticles on local ordering of liquid crystals and nanoparticle diffusion coefficients. *Nano Lett*, 9(7):2794-2801.

27. Abras D, Pranami G, Abbott NL (2012) The mobilities of micro- and nano-particles at interfaces of nematic liquid crystals. *Soft Matter*, 8:2026-2035.

28. Smith CJ, Denniston C (2007) Elastic response of a nematic liquid crystal to an immersed nanowire. *J Appl Phys*, 101:014305.

29. Brochard F, de Gennes PG (1970) Theory of magnetic suspensions in liquid crystals. *J Phys (Paris)*, 31:691-708.
30. Nazarenko VG, et al. (2010) Surface alignment and anchoring transitions in nematic lyotropic chromonic liquid crystal. *Phys Rev Lett*, 105:017801.

31. Shiyanovskii SV, et al. (2005) Real-time microbe detection based on director distortions around growing immune complexes in lyotropic chromonic liquid crystals. *Phys Rev E*, 71:020702.

32. Mondiot F, Chandran SP, Mondain-Monval O, Loudet J-C (2009) Shape-induced dispersion of colloids in anisotropic fluids. *Phys Rev Lett*, 103:238303.

33. Poulin P, Weitz DA (1998) Inverted and multiple nematic emulsions. *Phys Rev E*, 57:626-637.

34. Smalyukh II, Lavrentovich OD, Kuzmin AZ, Kachynski AV, Prasad PN (2005) Elasticity-mediated self-organization and colloidal interactions of solid spheres with tangential anchoring in a nematic liquid crystal. *Phys Rev Lett*, 95:157801.

35. Smalyukh II, Kachynski AV, Kuzmin AN, Prasad PN (2006) Laser trapping in anisotropic fluids and polarization-controlled particle dynamics. *Proc Natl Acad Sci U S A*, 103:18048-18053.

36. Darnton NC, Turner L, Rojevsky S, Berg HC (2007) On torque and tumbling in swimming *Escherichia coli*. *J Bacteriol*, 189:1756-1764.

37. Smalyukh II, et al. (2004) Ordered droplet structures at the liquid crystal surface and elastic-capillary colloidal interactions. *Phys Rev Lett*, 93:117801.

38. Lin I-H, Koenig GM, de Pablo JJ, Abbott NL (2008) Ordering of solid microparticles at liquid crystal-water interfaces. *J Phys Chem B*, 112:16552-16558.

39. Koenig GM, Lin IH, Abbott NL (2010) Chemoresponsive assemblies of microparticles at liquid crystalline interfaces. *Proc Natl Acad Sci U S A*, 107:3998-4003.

40. Tasinkevych M, Andrienko D (2010) Colloidal particles in liquid crystal films and at interfaces. *Condens Matter Phys*, 13:33603.

S1. Tuson HH, Copeland MF, Carey S, Sacotte R, Weibel DB (2013) Flagella density regulates *Proteus mirabilis* swarmer cell motility in viscous environments. *J Bacteriol*, 195:368-377.

S2. Champion JV, Meeten GH (1973) Conformation of sodium cromolyn in aqueous solution using light scattering and magnetic birefringence. *J Pharm Sci*, 62:1589-1595.

S3. Nastishin YA, et al. (2004) Pretransitional fluctuations in the isotropic phase of a lyotropic chromonic liquid crystal. *Phys Rev E*, 70:051706.

S4. Hartshorne NH, Woodard GD (1973) Mesomorphism in the system disodium chromoglycate-water. *Mol Cryst Liq Cryst*, 23:343-368.

S5. Lee H, Labes MM (1983) Phase diagram and thermodynamic properties of disodium cromoglycate-water lyomesophases. *Mol Cryst Liq Cryst*, 91:53-58.

S6. Luk Y-Y, et al. (2003) Using liquid crystals to amplify protein−receptor interactions: Design of surfaces with nanometer-scale topography that present histidine-tagged protein receptors. *Langmuir*, 19:1671-1680.

# CHAPTER 4

## Using Liquid Crystals to Reveal How Mechanical Anisotropy Changes Interfacial Behaviors of Motile Bacteria

Adapted from

Peter C. Mushenheim, Rishi R. Trivedi, Douglas B. Weibel & Nicholas L. Abbott, Using Liquid Crystals to Reveal How Mechanical Anisotropy Changes Interfacial Behaviors of Motile Bacteria. Biophysical Journal. 2014; 107(1), 255-265.

**Abstract**

Bacteria often inhabit and exhibit distinct dynamical behaviors at interfaces, but the physical mechanisms by which interfaces cue bacteria are still poorly understood. In this Article, we use interfaces formed between coexisting isotropic and liquid crystal (LC) phases to provide insight into how mechanical anisotropy and defects in LC ordering influence fundamental bacterial behaviors. Specifically, we measure the anisotropic elasticity of the LC to change fundamental behaviors of motile, rod-shaped *Proteus mirabilis* cells (3 $\mu$m in length) adsorbed to the LC interface, including the orientation, speed and direction of motion of the cells (the cells follow the director of the LC at the interface), transient multi-cellular self-association, and dynamical escape from the interface. In this latter context, we measure motile bacteria to escape from the interfaces preferentially into the isotropic phase, consistent with the predicted effects of an elastic penalty associated with strain of the LC about the bacteria when escape occurs into the nematic phase. We also observe boojums (surface topological defects) present at the interfaces of droplets of nematic LC (tactoids) to play a central role in mediating the escape of motile bacteria from the LC interface. Whereas the bacteria escape the interface of nematic droplets via a mechanism that involved nematic director-guided motion through one of the two boojums, for isotropic droplets in a continuous nematic phase, the elasticity of the LC generally prevented single bacteria from escaping. Instead, assemblies of bacteria "piled up" at boojums and escape occurred through a cooperative, multi-cellular phenomenon. Overall, our studies demonstrate that the dynamical behaviors of motile bacteria at anisotropic LC interfaces can be understood within a conceptual framework that reflects the interplay of LC elasticity, surface-induced order, and topological defects.

**Introduction**

Many bacteria live at interfaces (1–11). The accumulation of bacteria at liquid-solid and liquid-air interfaces is an early step in the formation of bacterial communities that have a staggering impact on ecology (1–5), industrial processing (1, 6, 7), agriculture (1, 8, 9), and human health (1–3, 5, 10, 11). In response to the growing significance attributed to bacteria in these niches, microbiologists have studied the mechanisms that influence cell movement, behavior, and assembly into multi-cellular structures at interfaces (12–17). Much of this research has centered around biofilms on the surfaces of rigid solids due to the impact of these structures on human health, and the high costs associated with eradicating these microbial communities (18–20). Although the extracellular matrix of biofilms (21, 22) and other complex fluids in which bacteria live (e.g., synovial fluid, chitin, mucus, as well as fluids enriched in biopolymers such as collagen and cellulose (15, 23, 24)) possess anisotropic physical properties, virtually nothing is known about how anisotropy of an interfacial environment impacts fundamental bacterial behaviors. Significantly, the range of bacteria living in these anisotropic environments includes the biomedically important organisms *Mycobacterium tuberculosis*, *Neisseria gonorrhoeae*, *Pseudomonas aeruginosa, Staphylococcus aureus,* and beta-hemolytic strains of *Streptococcus* (22–24). While previous investigators have studied bacteria at interfaces of isotropic liquids (25–29), developing an understanding of the behavior and dynamics of bacteria at interfaces of anisotropic complex fluids, such as the liquid crystals (LCs) described in this Article, has the potential to open a new window through which to view bacteria in environments that are relevant to biofilms, infections and other fundamental and technological contexts.

In contrast to our lack of understanding of motile bacteria at the interfaces of complex fluids such as LCs, much more is known about the behavior at LC interfaces of synthetic microparticles that are commensurate in size to bacteria (30–37). Three key properties of LCs impact the equilibrium and dynamic interfacial behaviors of such micrometer-sized particles. First, because of the long-range ordering of molecules within LC phases, elastic strain of LCs about adsorbed microparticles gives rise to inter-particle forces that have unusual symmetries (30–34). These LC-mediated inter-particle forces can generate hexagonal and chain-like two-dimensional interfacial assemblies. Second, LC phases possess anisotropic viscosities that influence the dynamics of localized particles, as indicated by the anisotropic diffusion of microparticles adsorbed to LC interfaces (35). Third, topological defects that form at the surfaces of curved LC interfaces, such as LC droplets, possess high free energy densities and thus attract and localize microparticles (36, 37). Inspired by these past observations regarding synthetic microparticles at LC interfaces, we hypothesized that LC elasticity, viscosity and topological defects would also likely impact fundamental behaviors of motile bacteria at LC interfaces.

In this Article, we report the use of *Proteus mirabilis* as a model bacterium to study the dynamics of motile bacteria at interfaces of LCs, as it has been demonstrated previously that genetically manipulating flagella density on *Proteus mirabilis* can create cells that produce sufficient flagella-derived propulsive forces to move through viscous fluids (38). Specifically, *P. mirabilis* cells overexpressing flagella (that we refer to as *P. mirabilis* in this Article) are rod-shaped with a length of ~3 μm and move at a velocity, $\overline{V}$ = 6.9 +/- 1.6 μm/s through an aqueous polymer solution that has a kinematic viscosity (0.83 Pa·s) (38) comparable to the nematic LCs reported in this Article. The interfaces used in our studies of *P. mirabilis* are formed between coexisting

isotropic and nematic domains of aqueous solutions of disodium cromoglycate (DSCG) (Fig. 1 A). This use of DSCG interfaces extends previous studies of bacterial motility within the bulk phase of the LC (39–41). We recently reported that *P. mirabilis* cells align nematic DSCG phases parallel to their surfaces (40). Minimization of the associated elastic strain of the LC resulted in orientations and motions of the rod-shaped cells along the nematic director (40). We found also that the elasticity of the LC mediates attractive forces that assemble *P. mirabilis* cells into linear, multi-cellular structures. Formation of these structures was dynamic and reversible due to the interplay of flagella-derived propulsive forces and the elasticity-mediated attractive forces, both of which were comparable in magnitude for motile *P. mirabilis* cells (tens of pN).

The nematic-isotropic (N-I) interfaces used in our current study are defined by "tactoids," which are elongated and cusped domains of either nematic LC in a continuous isotropic solution or isotropic phase domains dispersed in a continuous LC phase (42–45). Such domains define a particularly interesting class of LC interfaces because their geometry leads to the generation of surface-localized topological defects (see below for additional discussion). Using this experimental system, we sought to determine whether bacteria would insert into the N-I interface of the tactoids and whether the orientational order (and associated anisotropic mechanical properties) of the nematic interface would guide the interfacial motility of cells. In addition, inspired by observations (see above) of the association of microparticles with defects of LC droplets (36, 37), we aimed to explore how motile bacteria would be influenced by interfacial defects in the LC order. As described below, we find that the nematic elasticity of the LC combines with the presence of defects to define specific pathways by which bacteria can escape from nematic interfaces. We also show how this phenomenon can be tuned to control the

capture and release of motile bacteria in LCs. We close this Introduction by noting that a recent publication by Zhou et al. reports an observation regarding the interaction of *Bacillus subtilis* cells with isotropic tactoids in nematic LC (41). Below we contrast our findings with *P. mirabilis* to the observation with *B. subtilis* cells.

## Materials and Methods

### Bacterial strains and cell culture

*P. mirabilis* strain HI4320 was transformed with plasmid pflhDC to create *P. mirabilis* cells overexpressing flagella. The plasmid pflhDC contained the *flhDC* genes from *P. mirabilis* inserted into pACYC184 (which contains a gene for chloramphenicol resistance). *P. mirabilis* cells were grown in chloramphenicol-resistance nutrient medium consisting of 1% (wt/vol) peptone (Becton, Dickinson, Sparks, MD), 0.5% (wt/vol) yeast extract (Becton, Dickinson), and 1% (wt/vol) NaCl (Fisher Scientific, Fairlawn, NJ) at 30°C in a shaking incubator (38). Saturated overnight cultures were diluted 100-fold in 10 mL of fresh nutrient medium and grown in 150 mL Erlenmeyer flasks at 30°C in a shaking incubator at 200 rpm. We observed that the highest swimming velocity of *P. mirabilis* cells occurred during stationary phase, hence we harvested cells at an absorbance ($\lambda$ = 600 nm) of ~3.2 and concentrated them by centrifugation. The cells were washed three times with an aqueous buffer for bacterial motility (0.01 M $KPO_4$, 0.067 M NaCl, $10^{-4}$ M EDTA, 0.1 M glucose, and 0.001% Brig-35, pH 7.0). To obtain non-motile *P. mirabilis* cells, the cells were treated with 4% glutaraldehyde for 3 h at 25°C after harvesting.

### Lyotropic LC preparation

Disodium cromoglycate (DSCG) was purchased from Sigma-Aldrich (Milwaukee, WI) and used as received. Lyotropic LCs containing DSCG were prepared by mixing 15.3 wt% of DSCG with 84.7 wt% of aqueous motility buffer. The mixture was shaken for at least 12 h to ensure complete solubility and homogeneity. Prior to experimentation, the DSCG solution was heated at 65°C for 10 min to avoid possible time dependence of the properties of the mixture (46, 47).

After cooling the solution to 25°C, a small volume of motility buffer containing bacteria was added to the DSCG mixture producing a final concentration of ~$10^5$ cells/μL. The final concentration of DSCG was 15.0 wt% in all experiments.

**Preparation of imaging chambers**

We created imaging chambers by adding a small volume (~1 μL) of DSCG solution on top of a glass slide between two sheets of 18 μm-thick Mylar film. A glass cover slip was placed on top of the Mylar and the chamber was sealed with epoxy to prevent water evaporation (see Fig. S1 in the Supporting Material). We confirmed the direction of alignment of the nematic LC by inserting a quarter wave plate into the optical path of a microscope and analyzing the appearance of the sample between crossed polars (48). Imaging chambers were used within 3 h of their preparation.

**Microscopy**

We imaged cells using a Nikon Eclipse Ti inverted optical microscope equipped with crossed polarizers and a Photometics CoolSNAP HQ2 CCD camera (Tucson, AZ) using a Nikon Plan Apo $\lambda$, 100X/1.45 oil objective lens. Videos were collected with the EM gain off and with a 90 ms exposure time (11 frames/sec). Images of cells were collected using Nikon NIS Elements software. A thermoplate (Tokai Hit, Japan) and 100X objective heater (Bioptechs, PA) were used to control the temperature of the samples during experiments. DSCG solutions were equilibrated at a particular temperature for at least 10 minutes prior to making observations and performing measurements of bacteria motility. An Olympus BX60 microscope equipped with crossed polarizers was also used to analyze the imaging chambers. Images were captured using a

digital camera (Olympus C-2040 Zoom) mounted on the microscope and set to a f-stop of 2.8 and a shutter speed of 1/125 sec.

**Bacterial motility data analysis**

Microscopy data for motile cells were analyzed using the MATLAB computing environment (MathWorks, Natick, MA, USA) by identifying the centroid of each bacterium in successive frames and grouping those points together to create a cell trajectory. These data were combined with the CCD frame rate to determine cell velocity.

**Tactoid triple phase contact line measurement**

Individual video frames were opened in ImageJ and the position of the triple phase contact line was determined using the "Find Edges" tool. Three consecutive traces of the triple phase contact line were performed to estimate its length.

**Statistical analysis**

All experimentally determined values have been reported in the text and figures with associated standard errors unless otherwise noted.

## Results

### Capture and escape of *P. mirabilis* cells from the interfaces of nematic tactoids

We first sought to determine whether motile *P. mirabilis* cells would adsorb to interfaces formed between coexisting aqueous nematic and isotropic phases of 15 wt% DSCG in motility buffer. To this end, we prepared optical chambers containing 18 μm-thick DSCG films (see above) in which the nematic phase of DSCG was oriented parallel to the glass substrates and exhibited a degenerate azimuthal alignment. We observed the 15 wt% DSCG solution to form coexisting nematic and isotropic domains at temperatures between 29°C and 35°C. Specifically, after quenching samples from 40°C (isotropic phase) to 33°C, "spindle-like" domains of nematic phase with positive interface curvature and an elongated and cusped shape (tactoids) formed on the surface of the glass slides within a continuous isotropic phase (Fig. 1B) (42–45). The prolate shape of the tactoids arises from a competition between the elasticity of the nematic phase and the interfacial tension between the nematic and isotropic phases (49, 50). As detailed elsewhere (42–45), imaging of the nematic tactoids between crossed polars confirmed that the LC was anchored tangentially at the N-I interface and that two topological LC defects (boojums (42, 51)) were located at the cusped poles near the triple phase (N-I-glass substrate) contact line. Although the elastic constant for twist ($K_{22}$) in nematic DSCG is an order of magnitude smaller than the elastic constants for splay ($K_{11}$) and bend ($K_{33}$) (52), we did not observe a twisted director profile within the sessile nematic tactoids, as evidenced by the extinction that occurs in the center of the tactoid when the major axis of the tactoid is aligned parallel with one of the polarizers (Fig. 1 *B*) (43, 44, 49, 53, 54). We also formed isotropic phase tactoids (in a continuous nematic phase) in our studies by heating a 15 wt% DSCG solution from 25°C (nematic phase) to 30°C (Fig. 1C). We observed that both nematic and isotropic tactoid domains

generally nucleated at and remained attached to one of the glass substrates and following equilibration at either 33°C (nematic tactoids) or 30°C (isotropic tactoids) for several minutes, grew to a structure that was 30-μm in diameter along the major axis (Fig. 1D). Unless otherwise noted, we restrict our observations to tactoids that had depth d < 18 μm, which is smaller than the gap between the glass substrates.

When *P. mirabilis* cells were dispersed uniformly in isotropic phases of DSCG at 40°C and then cooled to 33°C, we observed that the cells were excluded from the growing nematic domains (Figs. 1B and 2A) and became concentrated in the continuous isotropic phase as well as proximate to the curved N-I interfaces of the tactoids. The *P. mirabilis* cells suspended within the bulk isotropic phase at 33°C moved without a directional bias with an average velocity of $\overline{V}$ = 17.6 +/- 0.7 μm/s (N = 34), which is significantly faster than the velocity we measured previously for *P. mirabilis* cells in an isotropic phase of 15 wt% DSCG at 42°C ($\overline{V}$ = 8.1 +/- 0.3 μm/s (40)) (Table 1). This difference in velocity is consistent with an increase in the viscosity of isotropic DSCG solutions with decreasing temperature (46) and an inverse relationship between *P. mirabilis* velocity and solution viscosity for μ < 9 mPa·s (38) (See Table 1 for viscosities). In contrast to the random movement of cells in the bulk isotropic phase, we observed bacteria near the surface of tactoids propelling themselves with clear directional bias along the N-I interface and the triple phase contact line with an average velocity of $\overline{V}$ = 17.1 +/- 0.4 μm/s (N = 40) (Table 1).

Limited by the resolution of our optical microscope, we were unable to initially determine whether the *P. mirabilis* cells near the N-I interface were inserted into the interface, such that

they contacted both nematic and isotropic phases, or whether they remained suspended in the isotropic phase. We hypothesized that if they were inserted into the interface, *P. mirabilis* cells (which we reported previously anchor LCs tangentially (40)) would preferentially orient and move parallel to the local director at the interface of the tactoid due to the elasticity of the nematic phase. Fig. 2C depicts the trajectory of a *P. mirabilis* cell that we observed to move along the N-I interface of a nematic tactoid. The cell depicted in Fig. 2 *C* moves out of the focal plane—located at the surface of a glass slide—as it moves along the interface of the sessile tactoid. A comparison of Figs. 2B and 2C reveals that the trajectory of the cell follows the interfacial director profile of the tactoid (Movie S1). We also determined the long axis of the motile bacterium to be oriented parallel to the LC director. Analysis of additional bacterial trajectories near nematic tactoids yielded similar results (Fig. S2). In particular, we note that due to the quadrupolar symmetry of the tactoids, bacteria were guided by the LC director towards either of the boojum defects. Based on the directed motion of *P. mirabilis* at the interface of the tactoid, we concluded that the motile cells adsorb and insert into the N-I interface. We also observed non-motile bacteria (*P. mirabilis* cells treated with 4% glutaraldehyde) to adopt orientations parallel to the local nematic director when positioned at the interface of nematic tactoids (Fig. S3).

The strong adsorption of micrometer-sized particles to liquid-liquid interfaces is known to be driven, in part, by the interfacial tension between the two phases. To determine if the interfacial tension between the isotropic and nematic phases of the DSCG solution ($\gamma_{NI}$) is sufficiently large to drive the adsorption of the bacterial cells, we considered that the prolate shape of tactoids (with characteristic radius, R) arises from a balance between the elasticity of the bulk nematic phase (which scales as ~KR, where K is a one constant approximation of the LC elastic constant) and the energy of the N-I interface (which scales as ~ $\gamma_{NI}$ $R^2$) (43, 49, 50). For these bulk and surface energies to be comparable when R ~ $10^{-5}$ m (using K ~ 10 pN (52)), we estimate that $\gamma_{NI}$ is ~ $10^{-6}$ J/m$^2$. This agrees with estimates of $\gamma_{NI}$ for other lyotropic LCs including aqueous sols of vanadium pentoxide (49) ($\gamma_{NI}$ ~ $10^{-6}$ J/m$^2$) and aqueous suspensions of cellulose crystallites (55) ($\gamma_{NI}$ ~ $10^{-6}$ – $10^{-7}$ J/m$^2$) although a larger estimate ($\gamma_{NI}$ ~ $10^{-4}$ J/m$^2$) has been reported previously for DSCG (42). By modeling *P. mirabilis* cells as rod-shaped particles with a major axis 2*a* and minor axis 2*b*, and by noting the radius of curvature of the interface to be large compared to the cell, the interfacial area ($A_{NI}$) removed due to the presence of an adsorbed bacterium is given by $A_{NI} = \pi b^2 \sin^2\left[\cos^{-1}(1-h/b)\right]\left[1+\frac{4(a/b-1)}{\pi \sin\left[\cos^{-1}(1-h/b)\right]}\right]$, where *h* is the depth of immersion of the bacterium in the nematic phase (56). From this expression, we calculate the maximum area occupied by *P. mirabilis* to be 2.8 μm$^2$, thus leading to an upper bound on the contribution of $\gamma_{NI}$ to the adsorption energy of 3 × $10^{-18}$ J/cell (~$10^3$kT). This value is consistent with our observation of irreversible adsorption of non-motile *P. mirabilis* cells to the interfaces of nematic tactoids of DSCG.

Although we calculated *P. mirabilis* cells to be attached to the N-I interface with an adsorption energy of ~$10^3$kT, we observed motile cells to be able to escape from the interface of nematic

tactoids and enter the continuous isotropic phase. Fig. 2, C–E show a representative example in which a motile cell adsorbs to a nematic tactoid and follows the director profile along the interface of the tactoid (Fig. 2C) to arrive at one of the two cusped poles of the tactoid, where a boojum is present (Fig. 2D). At the boojum, the cell escapes from the N-I interface into the isotropic phase (Fig. 2E). Overall, we found that two-thirds (N = 170) of motile bacteria that escaped from the interface of nematic tactoids did so near a boojum. We hypothesize that this dominant mode of escape reflects the fact that (i) motile bacteria are focused to the boojums by the convergence of the LC director profile (Fig. 2B); and (ii) a component of the flagella-derived force produced by cells ($F_{prop}$; estimated to be ~60 pN for *P. mirabilis* moving in bulk nematic DSCG (40)) is directed normal to the contact line near the boojum and thus can overcome forces associated with interfacial tension that hold cells at the interface (Fig. 2F). These ideas are supported by additional observations reported below which reveal motile bacteria to escape from the N-I interfaces of isotropic tactoids almost exclusively via boojums.

Whereas bacterial cells were able to escape from the N-I interface into the isotropic phase, we did not observe detachment of motile bacteria from the N-I interface into the interior of the nematic tactoids in our experiments. Two factors are likely responsible for this observation. First, due to the convex curvature of the N-I interface, cells adsorbed at the interface are unable to create a component of $F_{prop}$ that is directed radially inward towards the interior of the nematic tactoid (Fig. 2F). Second, an energetic penalty associated with elastic strain of the nematic director around a cell, which occurs principally near the hemispherical poles of the bacteria (40, 57), will tend to prevent escape of bacteria into the LC phase. We estimate the energy associated with the elastic strain of the LC around a cell on the interface as $E_{elastic} \sim K b\, f(h/b)$, where $f(x)$

is a dimensionless function of the location of the cell at the interface (32, 58). For *P. mirabilis* and 15 wt% DSCG, we estimate K*b* to be $5 \times 10^{-18}$ J, and conclude that the magnitude of this elastic energy penalty is comparable to the adsorption energy due to interface tension.

The above conclusion that the energetic effects associated with elastic deformations around bacteria are comparable to interfacial tension leads us to also hypothesize that the nematic elasticity of the LC likely impacts the location of cells at N-I interfaces. Specifically, the elasticity of the LC should promote contact of the surface of the cells with the isotropic phase at the interface. Indeed, our measurement of *P. mirabilis* cells moving along the N-I interface with an average velocity similar to that in bulk isotropic phase at 33°C (Table 1) suggests that the majority of the surface of each cell is in contact with the isotropic phase.

**Dynamics of *P. mirabilis* cells at the interfaces of isotropic tactoids**

Based on the observations above, we interpret the curvature of the N-I interface and the elasticity of the LC to play key roles in influencing the interfacial behavior of bacteria. To further explore how these properties of the N-I interface impact *P. mirabilis* behaviors, we created isotropic domains within a continuous nematic phase by heating 15 wt% DSCG solutions from 25°C (nematic phase) to 30°C (Fig. 1C). The lateral size (~30 μm in diameter) and elongated, tactoidal shape of the isotropic domains resembled the nematic tactoids at 33°C described above. However, tangential anchoring of the LC produced boojum defects just outside the N-I interface of the two cusped poles of the isotropic tactoids (Fig. 3, A and B). In addition, the morphologies of the isotropic domains that formed—particularly when they were in close proximity to one

another (Fig. 1C)—displayed considerably greater complexity than the nematic domains (Fig. 1B) due to the strain present in the continuous nematic phase separating the isotropic domains. We found that isotropic domains with either one or three cusps nucleated from the cores of half-integer disclinations when heating from the nematic phase (42). Below, we describe experiments with motile bacteria interacting with sessile isotropic tactoids containing two cusps.

During the heating of DSCG solutions into the biphasic region, we observed motile *P. mirabilis* cells to adsorb to the interface of the growing isotropic tactoid domains. Consistent with previous observations for *B. subtilis* (41), the orientation and motion of the adsorbed motile *P. mirabilis* cells were constrained to be parallel to the orientation of the local director of the adjacent nematic phase (Fig. 3, B and C), similar also to motile bacteria adsorbed to nematic tactoids (Fig. 2). Cells moved along the interface of isotropic tactoids with an average velocity of $\overline{V}$ = 16.7 +/- 0.5 μm/s (N = 40). This velocity is similar to our measurement of bacterial motility at the interface of nematic tactoids (Table 1) and suggests that the interfacial environment experienced by *P. mirabilis* cells at the N-I interface (away from the cusps) is similar for the two types of tactoids.

In contrast to our observations with nematic tactoids (motile cells did not detach from the N-I interface to enter the nematic phase), however, we observed motile *P. mirabilis* cells to escape the N-I interface of isotropic tactoids into the surrounding nematic phase. Escape of motile cells into the nematic phase primarily (~95%, N = 274) occurred at one of the two cusped poles of the tactoid, where boojums are located in the adjacent nematic phase (Fig. 3B). We observed cell detachment to occur by at least two mechanisms. First, as shown by the sequence of micrographs in Fig. 3C, we observed individual *P. mirabilis* cells adsorbed at the N-I interface to

move toward one of the cusps of the isotropic tactoids, where they escaped (Movie S2). Detachment of isolated cells from isotropic tactoids in this manner closely resembled our previous observations of the method of cell detachment from nematic tactoids (Fig. 2) as well as the mechanism of single-cell escape from the interface of an isotropic tactoid observed for *B. subtilis* (41).

However, we more frequently observed a second mechanism through which groups of motile *P. mirabilis* cells collectively escaped the interface of isotropic tactoids (Fig. 3D, Movie S3). This event occurred when an adsorbed motile cell arrived at the cusp of an isotropic tactoid and appeared to get trapped by the boojum defect. Subsequently, additional cells that were directed towards the same cusp by the interfacial LC director profile were blocked in their escape by the first cell. This phenomenon led to the accumulation of an assembly of cells at the boojum. After several cells were trapped near the boojum, these cells along with additional motile cells that arrived at the cusp exerted a collective force on the interface of the tactoid that was observed to deform the N-I interface near the accumulated cells and lead to a growing, measurable extension of the triple phase contact line with time (Fig. 3D). Ultimately, after the N-I interface near the cusp had been significantly deformed, the arrival of one additional motile cell at the cusp was typically observed to initiate collective escape of the entire cluster of cells into the nematic phase. Free from the strain generated by the assembly of bacteria, the N-I interface relaxed back to its initial state and the process could be repeated. Overall, we found that motile *P. mirabilis* cells exited the N-I interface of isotropic tactoids much more frequently through this cooperative mechanism than as individual cells (Fig. 3E). We also note that our observation of the trapping of motile bacteria at boojum defects near the cusps of isotropic tactoids closely resembles the

partitioning of synthetic (e.g., polystyrene) microparticles to surface-associated defects of LC droplets (36, 37). This latter phenomenon is driven by replacement of the high-energy defect core and surrounding strained LC by the particle. We hypothesize that this same mechanism underlies the trapping of motile bacteria at defects described in this Article. In support of this hypothesis, we observed that non-motile *P. mirabilis* cells, which adsorb irreversibly to isotropic tactoids, were also frequently localized at the cusps (Fig. S4).

While motile cells did not detach into the interior of nematic tactoids, we occasionally observed the detachment of motile cells into the interior of isotropic tactoids (Fig. S5) despite the curvature of the N-I interface, which largely prevents flagella-derived propulsive forces (of bacteria adsorbed parallel to the interface) from being directed towards the interior of tactoid domains (Fig. 2F). Together, these observations reflect the relative ease with which cells can detach from the N-I interface into the isotropic phase, likely due to several factors including the release of elastic strain accompanying cells at the interface (as opposed to introduction of additional strain associated with escape into the nematic phase) and the preferential wetting of adsorbed cells by the isotropic phase. To confirm this conclusion, we prepared two LC samples in parallel containing equal densities of motile cells. One sample was heated from room temperature to 30°C to form isotropic tactoids while the other was cooled from 40°C to 33°C to form nematic tactoids. After equilibration for 15 min, we imaged many tactoids in both samples and quantified the number of motile bacteria found adsorbed to the N-I interface. The tactoids that we analyzed were all of similar size (~30 μm in diameter). Inspection of Fig. 4 reveals that cells were only concentrated on the interface of the isotropic tactoids (see also Fig. S6). Additional observations confirmed that motile *P. mirabilis* cells have a much shorter residence

time on the N-I interface of nematic tactoids relative to isotropic tactoids. These differences provide added support for the conclusion that the elasticity of the nematic phase generates a barrier for bacterial detachment and that, in the presence of this barrier, bacteria escape is largely limited to a structured pathway that involves director-guided motion to boojums through which the cells exit using a force generated by a multi-cellular assembly.

**Capture and release of motile bacteria by using nematic elasticity and topological defects**

Our observations of the infrequency with which bacteria escape from the N-I interface of isotropic tactoids into the nematic phase—particularly when not proximate to a topological defect—led us to explore if it is possible to corral motile *P. mirabilis* within large isotropic domains of a 15 wt% DSCG solution at 30°C by quenching the solution from the isotropic phase into the biphasic region rather than heating from the nematic (the latter was shown in Fig. 3). We also hypothesized that the probability of encountering a topological defect would be dependent on domain size and thus release of bacteria from isotropic "corrals" might be tuned via control of the size of domains. To test this concept, we heated a suspension of cells in DSCG to 40°C and subsequently quenched the sample to 30°C. As the DSCG solution entered the biphasic region during cooling, motile cells were excluded from nucleating nematic phase tactoids. While the sample was equilibrated at 30°C, nematic tactoids grew in size and coalesced, trapping isotropic phase domains (Fig. 5, A–C). These isotropic domains were initially larger (~60 μm in diameter) than the sessile tactoid domains described above (Figs. 1 and 2) and contacted the glass substrates on both sides of the 18-μm tall chamber. As these large isotropic domains formed, the inward-directed motion of the N-I interface pushed high densities of cells forward and trapped them within or at the domain interface (Fig. 5A, Movie S4). For

example, we observed that more than 80 cells were captured within the 60 μm-wide isotropic domain near the plane of focus depicted in Fig. 5 *A*, representing an enhancement in the local concentration of the bacteria (Fig. 5D).

Due to the orientation of the director profile in the adjacent nematic phase (see Fig. 5C), motile cells were largely constrained to circular trajectories when adsorbed to the interface of the nearly cylindrical isotropic domains with diameters of 40 μm or larger. The large size and nearly circular cross-section of these isotropic domains (such as the one depicted in Fig. 5A) prevented most of the cells from escaping into the nematic phase. The cells were, in effect, corralled by the elasticity of the surrounding nematic phase. The few escape events that did occur took place proximate to one of the two LC surface defects in the nematic phase near the poles of the spanning isotropic domains (Fig. 5C), which are either boojums or cross sections of disclination lines.

By adjusting the temperature of the sample, we were able to tune the size of the isotropic corrals in which cells were confined. Specifically, over the course of 20 min, we slowly lowered the temperature of the sample from 30°C to 29°C and observed the isotropic domain to reduce in size and transform into a sessile droplet (Fig. 5, E and F). We found that by decreasing the area of the interface between the nematic and isotropic phases, *P. mirabilis* cells more frequently encountered the topological defects at the cusped regions at the N-I interface and escaped in greater numbers. For example, when the isotropic domain was approximately 30 μm in diameter (Fig. 5E), we observed that 20 cells escaped into the nematic phase over the course of one minute. This increase in escape frequency may also reflect changes in the morphology of the N-I

interface near the LC surface defects that occur as the isotropic domain becomes smaller and transforms into a sessile state (with two boojums, similar to Fig. 3).

When the temperature of our sample reached 29°C, we observed the cells that remained adsorbed to the interface of the shrinking isotropic domain to ultimately form a small multi-cellular aggregate (Fig. 5G). Past studies have reported that cooling DSCG samples from the biphasic region into the homogeneous nematic phase can shrink isotropic domains to disclination cores that remain stable even when positioned deep within the nematic phase (42). The disclination cores serve as the sites of nucleation of isotropic tactoids upon reheating. We also observed an isotropic tactoid to reform at the site of the bacterial aggregate in Fig. 5G upon reheating.

**Discussion**

The results presented in this paper reveal that interfacial environments defined by anisotropic phases have a profound impact on fundamental behaviors of motile bacteria. Our observations have broad implications for studies aimed at understanding microbes in a range of ecologically and pathogenically relevant microenvironments that are known or suspected to be anisotropic. Specifically, we have found that motile *P. mirabilis* cells adsorbed at interfaces between coexisting nematic and isotropic phases of a biocompatible lyotropic LC are strongly influenced by the elasticity of the nematic LC. For example, we observed the elasticity of the LC to orient both non-motile and motile bacteria at the N-I interface in a manner that minimized the elastic energy cost associated with the strain of the LC about the bacteria and resulted in strongly biased motion of motile bacteria along the interfacial director profile of nematic tactoids. This result is consistent with tangential anchoring of the LC at the surface of the bacteria. Significantly, this motion also led to LC director-guided accumulation of cells at defects at the interface of the tactoids. Additional evidence of the influence of the nematic elasticity of the N-I interface can be found in our observations of multi-cellular behaviors (Fig. 6). In particular, we observed *P. mirabilis* cells to assemble into linear chains induced by LC elasticity at the N-I interface (Fig. 6, *B* and *C*). These chains were observed to be dynamic and reversible consistent with the interplay between LC elasticity-mediated forces and flagella-derived propulsive forces (40) (Fig. 6, *D* and *E*). Overall, our observations suggest that curvature strain associated with anisotropic interfacial environments can orient rod-shaped bacteria and lead to new classes of inter-bacterial interactions that are absent in isotropic interfacial environments.

Another key influence of the elasticity of the nematic phase on the behavior of the bacteria at the N-I interface was evident in the statistics of bacterial populations found at the interfaces of isotropic versus nematic tactoids. Specifically, we observed the elastic energy penalty associated with strain of the LC about the cells in the nematic phase to substantially influence the probability of escape from nematic and isotropic domains. While escape from the interface of a nematic domain into the isotropic phase was facile and resulted in only transient associations of cells with nematic tactoids, bacteria adsorbed at the interfaces of isotropic domains formed within a continuous nematic phase exhibited much longer residence times. Moreover, the barrier created by the elastic energy penalty associated with strain of the LC about the cells resulted in the cells adopting a cooperative mechanism of escape that involved formation of transient colonies at the poles of isotropic domains. This set of observations suggests that individual bacterial present at the interfaces of heterogeneous isotropic-anisotropic systems will tend to preferentially exit the interfaces into the isotropic domains but that multi-cellular assemblies may form that enable the bacteria to inhabit the anisotropic domains.

As noted above, one of the most interesting findings of our study relates to the role that topological defects play in mediating the escape of bacteria from the N-I interface, particularly escape into bulk nematic phases. We observed escape from isotropic tactoids to occur most commonly through a collective mechanism that involved three distinct steps: (i) director guided motion of motile cells to a boojum, (ii) trapping of individual bacteria at the boojum, (iii) cooperative escape of an assembly of bacteria from the boojum once a critical colony size was formed. This collective phenomenon is in contrast to that observed for escape from the N-I interface into the isotropic phase of DSCG. While the predominant mechanism of escape was

still via a boojum, individual bacteria were able to dissociate from the potential well caused by the defect. In addition, non-motile bacteria were observed to associate irreversibly at the boojums of tactoids (Fig. S4), similar to passive synthetic particles. More broadly, these results suggest that defects present in anisotropic native environments in which bacteria live, whether transient or equilibrium in nature, likely play a central role in dictating fundamental behaviors, including collective dynamic behaviors, of the cells.

In a recent publication, Zhou et al. describe an observation of a single *B. subtilis* cell moving along the interface of an isotropic tactoid in a nematic LC before escaping attachment to the interface into the LC at the cusp of the tactoid (41). We note that this observation contrasts with our own conclusions obtained with *P. mirabilis* cells in which we quantified the statistics of escape and found escape from isotropic tactoids to be most commonly mediated by the cooperative multi-cellular mechanism described above (Fig. 3E). We also note that Zhou et al. do not report evidence of elasticity-mediated interactions between *B. subtilis* cells as we reported previously in bulk LCs (40), suggesting that *P. mirabilis* and *B. subtilis* cells differ in fundamental ways in terms of their behavior in LCs and at LC interfaces. Additionally, although both *P. mirabilis* and *B. subtilis* move at similar velocities through nematic DSCG (8.8 +/- 0.2 μm/s (40) and 8 +/- 3 μm/s (41), respectively), *B. subtilis* cells likely generate greater propulsive forces since they are approximately twice as long as *P. mirabilis*. Thus, while we have found that flagella-derived propulsive forces and elasticity-mediated forces are comparable in magnitude for *P. mirabilis* cells in DSCG (40), the relative magnitude of these forces appears to be different for *B. subtilis*.

We end this discussion by noting that the influence of nematic elasticity and topological defects on dynamic interfacial behaviors of bacteria, as reported in this paper, also suggests the basis of new approaches to manipulating bacteria in a technological context. We demonstrate, for example, that it is possible to use nematic elasticity of LCs to dynamically corral motile cells within isotropic domains in a continuous nematic phase and then release the cells through the topological defects of the domains via tuning of the sizes of the domain. In future studies, we envision spatially-targeted heating of a suspension of cells in DSCG (e.g., using Joule heating from an embedded wire or by dispersing dye molecules in the sample and employing a focused beam of light) to dynamically control the localization and release of bacteria.

**Conclusion**

Overall, our observations provide fundamental insight into how anisotropy, nematic elastic forces and topological defects can substantially change the behaviors of motile bacteria at interfaces between isotropic and anisotropic microenvironments in ways that are not observed at interfaces between isotropic phases. Not only do we find that the dynamics of individual cells are altered at anisotropic LC interfaces, as demonstrated by the guided motion of cells along the nematic director and interactions of cells with boojums, but we also uncover multi-cellular phenomena that emerge, including the organization of cells into chains and the formation and cooperative escape of large assemblies of cells from interfaces of isotropic domains. These studies open a new window through which to view the behavior of bacteria in conditions that recapitulate key physical properties of native bacterial environments and also suggest new opportunities to achieve temporal and spatial control over bacteria.

**Acknowledgements**

This chapter was prepared as a Full Paper reporting original research in the journal Biophysical Journal. I assisted Peter in conceiving, performing and analyzing the experiments and preparing the manuscript.

This work was supported by the National Science Foundation (under awards DMR-1121288 (MRSEC), CBET-0754921, and MCB-1120832), the National Institutes of Health (CA108467, AI092004, and 5T32GM08349), the Army Research Office (W911-NF-11-1-0251 and W911-NF-10-1-0181), and the United States Department of Agriculture (WIS01594).

**Fig. 1.** Formation of nematic and isotropic tactoids. (A) Molecular structure of DSCG. (B and C) Crossed polar images of (B) nematic and (C) isotropic tactoids. The nematic tactoids formed in imaging chambers following cooling of an isotropic phase of 15 wt% DSCG solution from 40°C to 33°C; isotropic tactoids formed in imaging chambers following heating of a nematic phase DSCG solution from 25°C to 30°C. (D) Three-dimensional depiction of the shape adopted by sessile tactoids (both isotropic and nematic) in our experiments. Scale bars are 100 μm.

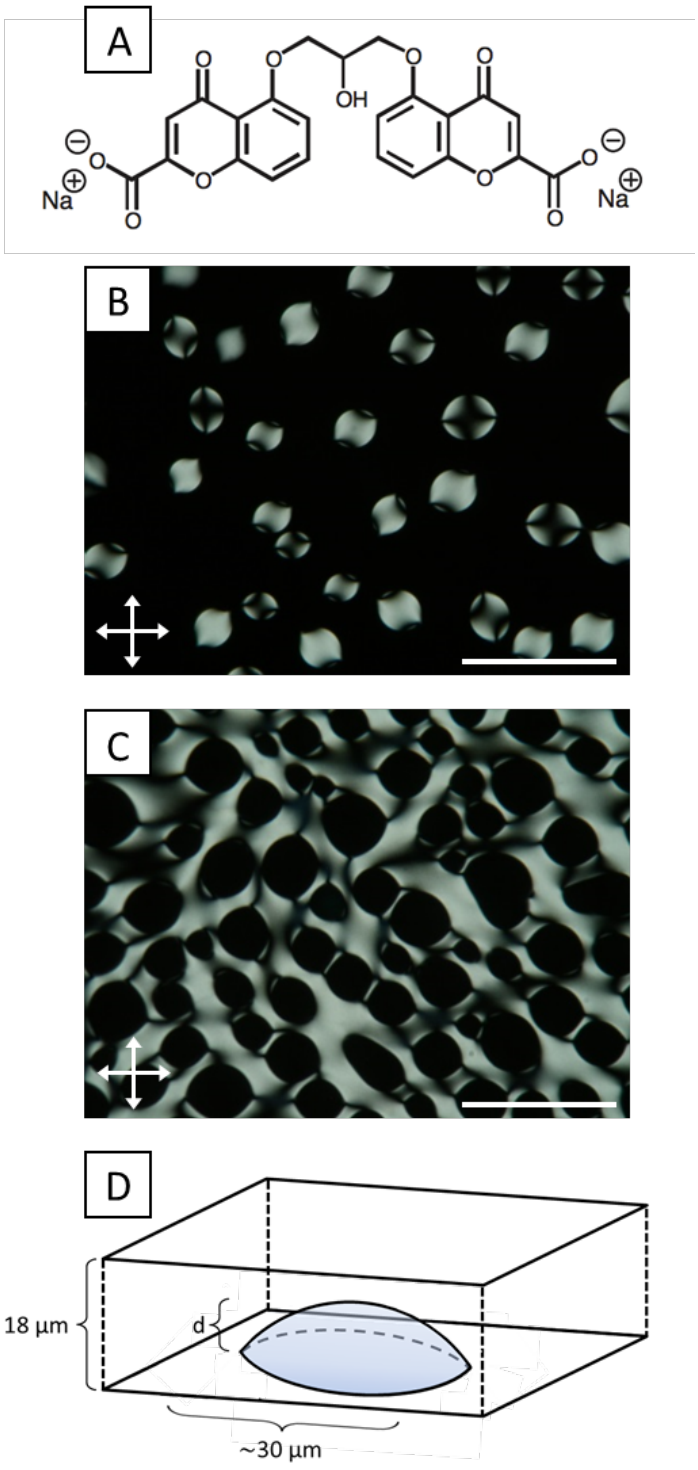


**Fig. 1**

**Fig. 2.** Guided motility and escape of a cell adsorbed to a nematic tactoid. (A) Optical micrograph (crossed polars) of a nematic tactoid that formed within a continuous isotropic phase upon quenching a 15 wt% DSCG sample from 40°C to 33°C and that partially wets one of the glass surfaces of the imaging chamber. (B) Schematic representation of the LC director profile of the tactoid in A. (C) Bright field micrograph of a nematic tactoid on which the trajectory of a motile P. mirabilis cell (depicted by an arrow) adsorbed to the N-I interface is indicated. (D and E) Bright field micrographs of a motile cell that escapes from the N-I interface at a boojum (topological defect at the cusped pole) of the tactoid. In D, the cell is oriented towards the viewer. (F) Schematic diagram depicting the orientation of the flagella-derived propulsive force ($F_{prop}$) of motile bacteria adsorbed at various positions on the interface of a nematic tactoid. Scale bars are 10 μm.

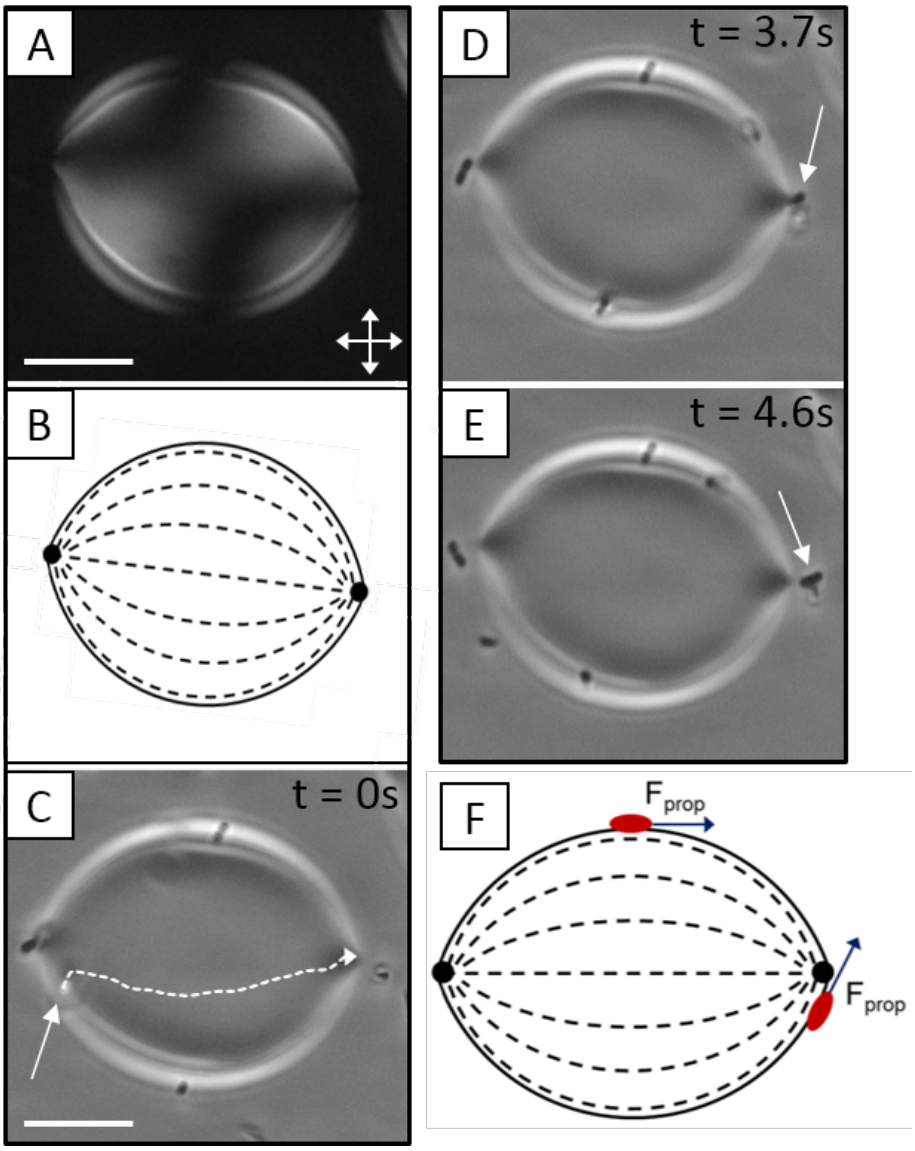


**Fig. 2**

**Fig. 3.** Escape mechanisms of motile bacteria from adsorption to an isotropic tactoid. (A) Optical micrograph (crossed polars) of a sessile isotropic tactoid that forms within a continuous nematic phase after heating a 15 wt% DSCG sample from 25°C to 30°C. (B) Schematic representation of the LC director profile in the nematic phase. (C) Sequence of images (bright field) depicting the escape of a motile P. mirabilis cell (indicated by an arrow) from the interface of an isotropic tactoid into the continuous nematic phase at the cusped pole of the tactoid (adjacent to a boojum defect in the nematic phase). (D) Graph and sequence of images (bright field) depicting the accumulation of motile P. mirabilis cells near the cusped pole of an isotropic tactoid and their collective escape. The force generated by trapped cells at the pole deforms the interface and extends the triple phase (N-I-glass substrate) contact line of the tactoid ($L_{tactoid}$). Ejection of the trapped cells into the nematic phase allows the interface to relax to its initial shape. (E) A plot of the frequency with which motile cells escape the N-I interface of isotropic tactoids near defect points as either single cells (as in C) or through a collective mechanism (as in D). Scale bars are 10 μm. Error bars represent standard deviations.

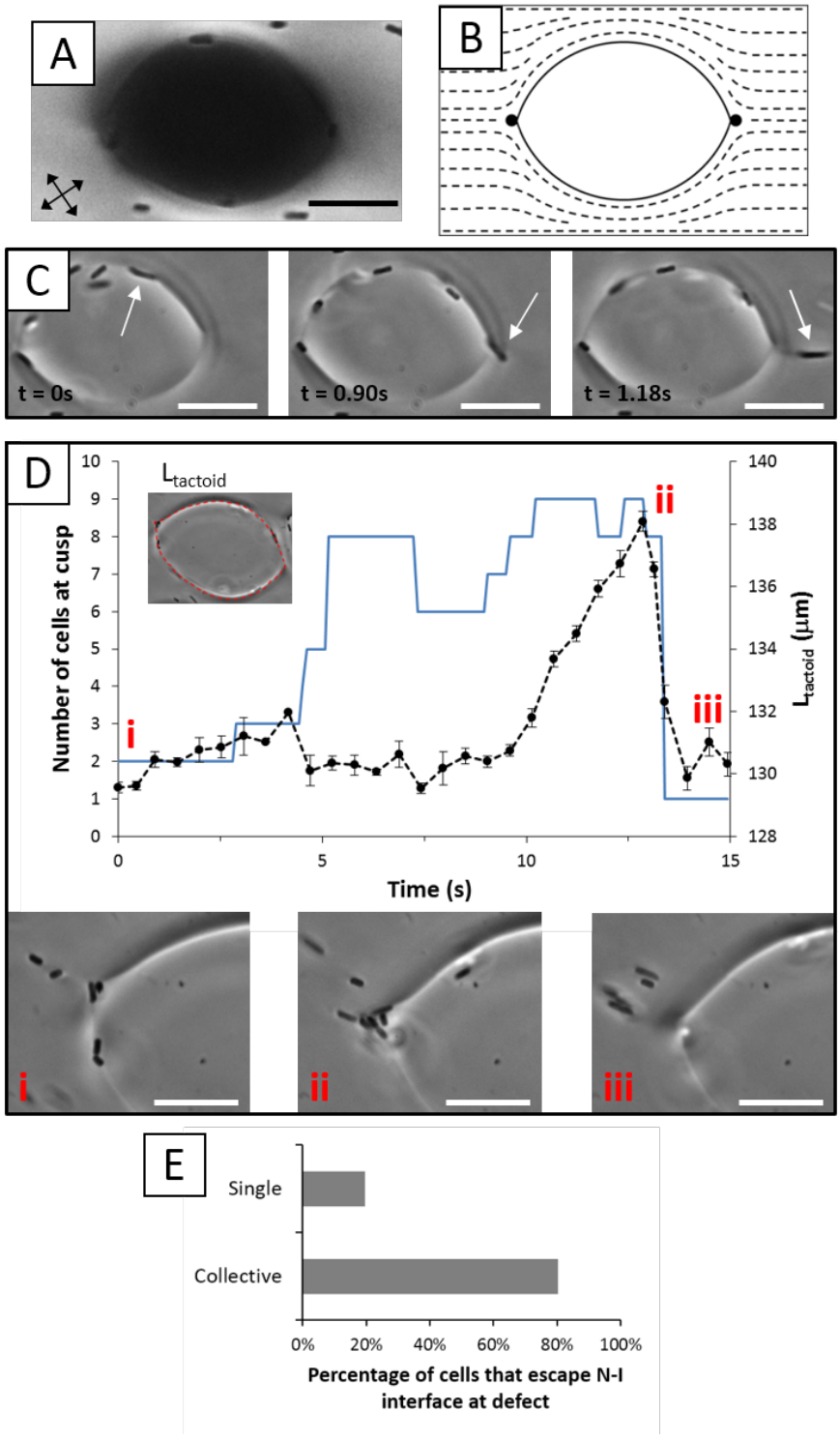
A
B
C
t = 0s
t = 0.90s
t = 1.18s
D
L tactoid
i
ii
iii
Number of cells at cusp
L tactoid (μm)
Time (s)
0
5
10
15
0
1
2
3
4
5
6
7
8
9
10
128
130
132
134
136
138
140
E
Single
Collective
0%
20%
40%
60%
80%
100%
Percentage of cells that escape N-I interface at defect

**Fig. 3**

**Fig. 4.** Temporal accumulation of motile bacteria at the interface of isotropic tactoids. Average number of cells adsorbed to nematic tactoids (at 33°C) (N = 35) and isotropic tactoids (at 30°C) (N = 37) following a 15-minute equilibration period at the indicated temperature. The tactoids were of similar size: ~30 μm in diameter. Error bars represent standard errors.

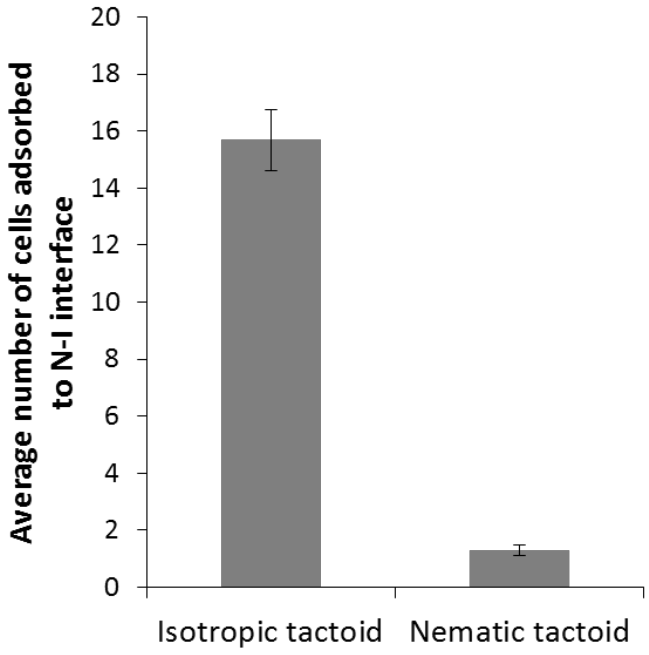
Average number of cells adsorbed to N-I interface
20
18
16
14
12
10
8
6
4
2
0
Isotropic tactoid
Nematic tactoid

**Fig. 4**

**Fig. 5.** Temperature-controlled capture and release of bacteria from an isotropic domain. (A) Bright field micrograph of an isotropic domain (diameter ~60 μm) that forms upon quenching a 15 wt% DSCG sample from 40°C to 30°C and spans the 18 μm-thick imaging chamber. (B) Corresponding crossed polars optical micrograph. (C) Schematic representation of the director profile corresponding to a cross section of the isotropic domain imaged in A and B. (D) Number of cells trapped by the isotropic domain depicted in A and in the nematic phase encompassing it. Cells both in and out of the focal plane are counted. The black, horizontal lines indicate the number of cells expected to be in the isotropic and nematic domains within the field of view as calculated based on the total concentration of cells (~$10^5$ cells/μL) in the suspension. (E–G) Bright field micrographs of the isotropic sample after cooling to 29.5°C, 29.2°C, and 29°C, respectively. Rafts of cells collectively escape into the nematic phase in E and F while an aggregate of cells forms as the isotropic domain in G nearly disappears. Scale bars are 20 μm.

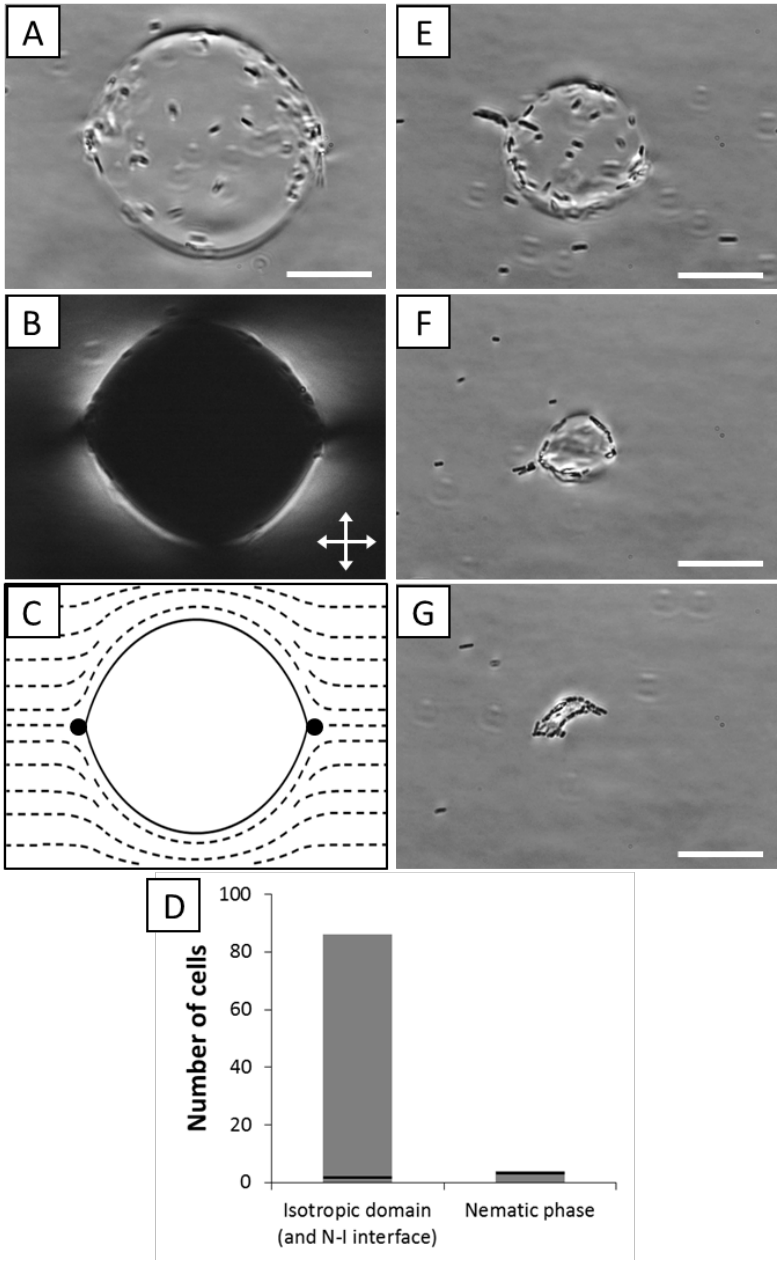
A
E
B
F
C
G
D
100
80
60
40
20
0
Number of cells
Isotropic domain
(and N-I interface)
Nematic phase

**Fig. 5**

**Fig. 6.** Reversible formation of multi-cellular assemblies at the N-I interface. (A) Estimated minimum separation distance as a function of time between (B and C) two motile *P. mirabilis* cells that undergo LC elasticity-mediated end-on-end association and between (D and E) two motile *P. mirabilis* cells that dissociate from a chain-like assembly. Scale bars are 5 μm.

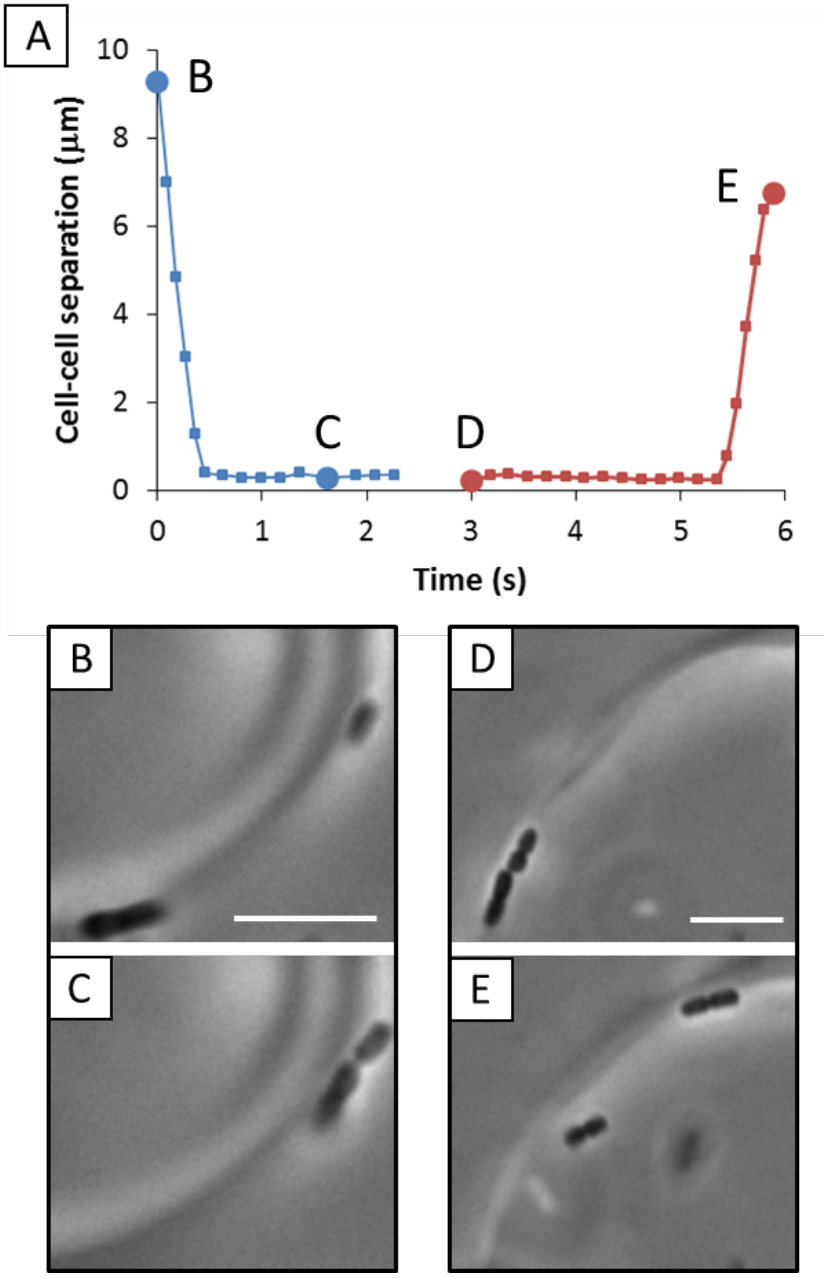


**Fig. 6**

**Figure S1.** Experimental setup. A schematic illustration depicting imaging chambers used to analyze bacterial cells in LC solutions. The LC director profile of nematic DSCG at 25°C (in a region of the sample exhibiting uniform polar and azimuthal alignment) is indicated by the dotted lines.

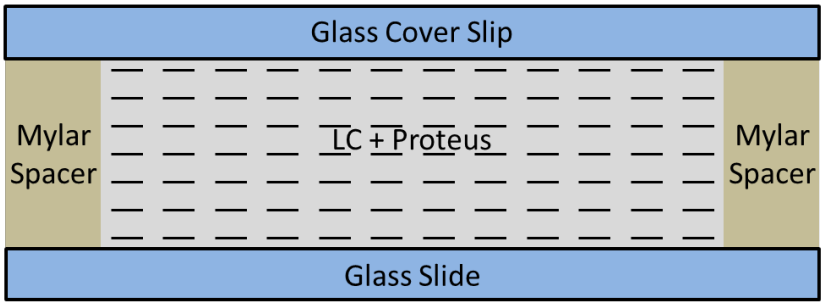


**Fig. S1**

**Figure S2.** Additional examples of LC elasticity-induced guided motility of cells adsorbed to nematic tactoids. Two examples (A–C and D–F) of the motility of *P. mirabilis* cells adsorbed to the interface of nematic tactoids. (A and D) Bright field micrographs of nematic tactoids on which the trajectories of motile *P. mirabilis* cells (indicated by arrows) adsorbed to the N-I interface are indicated. (B and E) Corresponding crossed polars images. (C and F) Schematic representations of the LC director profiles of the tactoids in B and E, respectively. Scale bars are 10 μm.

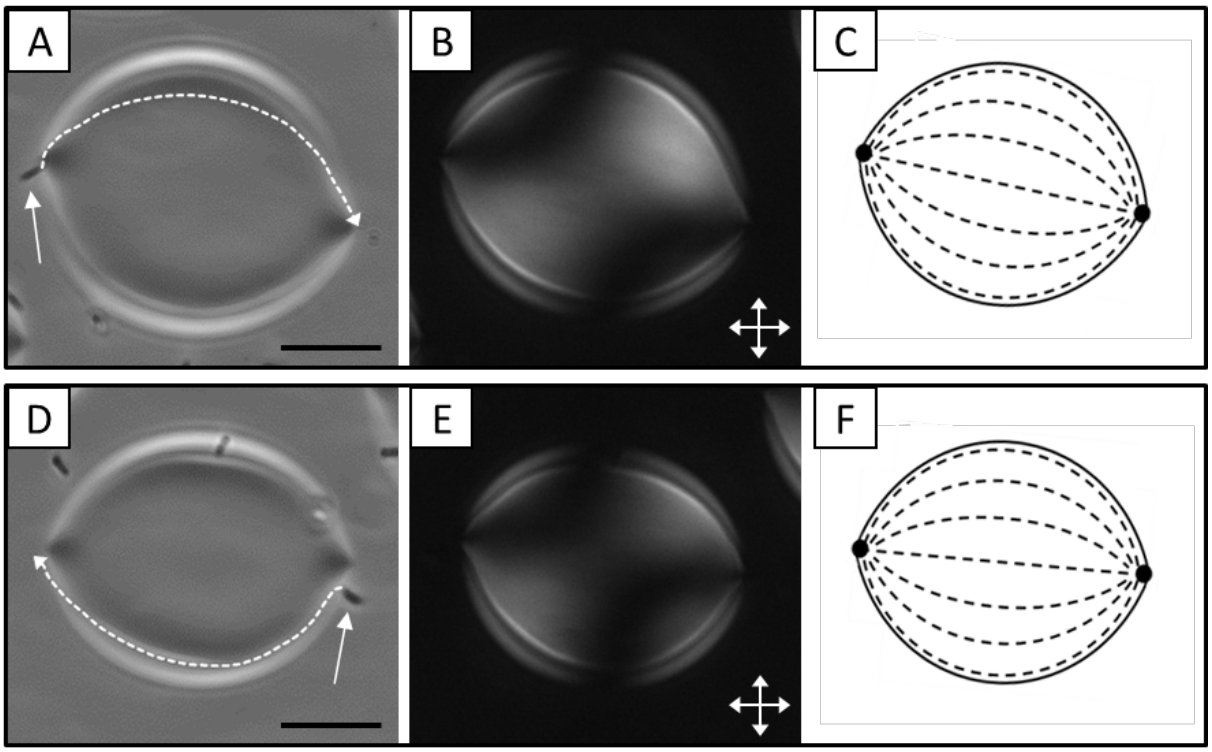


**Fig. S2**

**Figure S3.** Orientations of non-motile bacteria adsorbed to nematic tactoids. (A) Bright field and (B) crossed polars images, respectively, of non-motile *P. mirabilis* cells adsorbed at the interface of nematic tactoids that formed on a glass substrate following cooling of an isotropic phase of DSCG (15 wt%) from 40°C to 33°C. The scale bar is 10 μm.

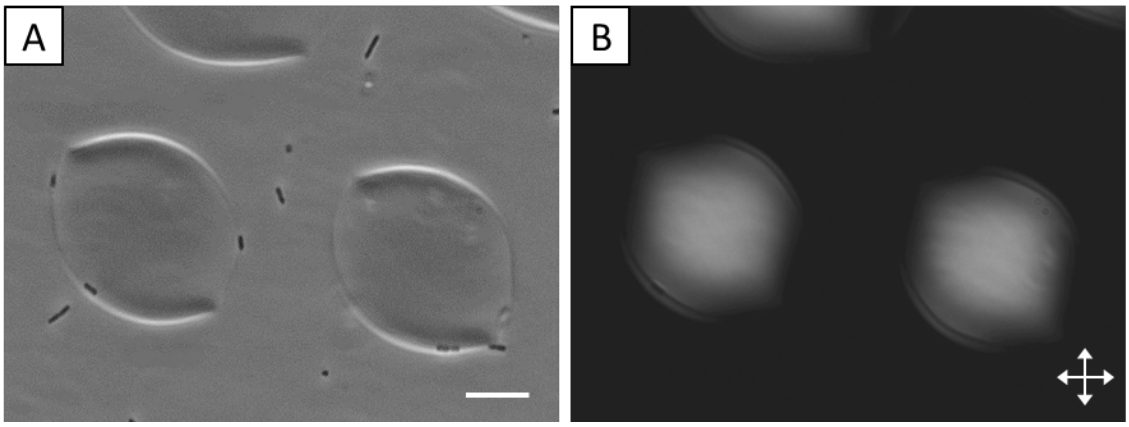


**Fig. S3**

**Figure S4.** Trapping of non-motile cells at the boojum associated with an isotropic tactoid. (A) Bright field and (B) crossed polars micrographs of non-motile *P. mirabilis* cells adsorbed at the N-I interface of an isotropic tactoid. Scale bars are 10 μm.

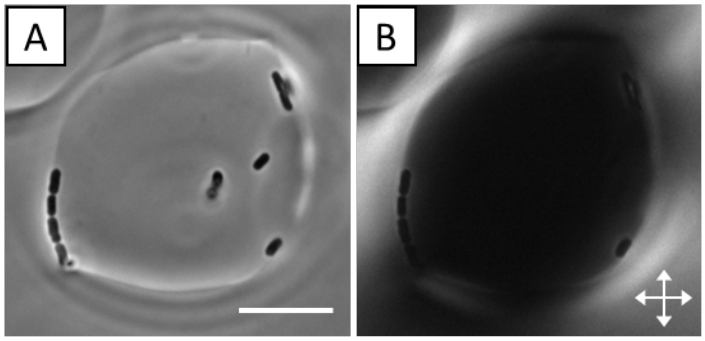


**Fig. S4**

**Figure S5.** Escape of an adsorbed motile cell into the interior of an isotropic tactoid. Sequence of bright field micrographs that depicts the trajectory of a motile *P. mirabilis* cell, initially adsorbed to the interface of an isotropic tactoid, which escapes into the interior of the tactoid. The trajectory of the cell (indicated by a red dot) is depicted in the images. The random motion of the cell suggests that it is not adsorbed to the N-I interface. The scale bar is 10 μm.

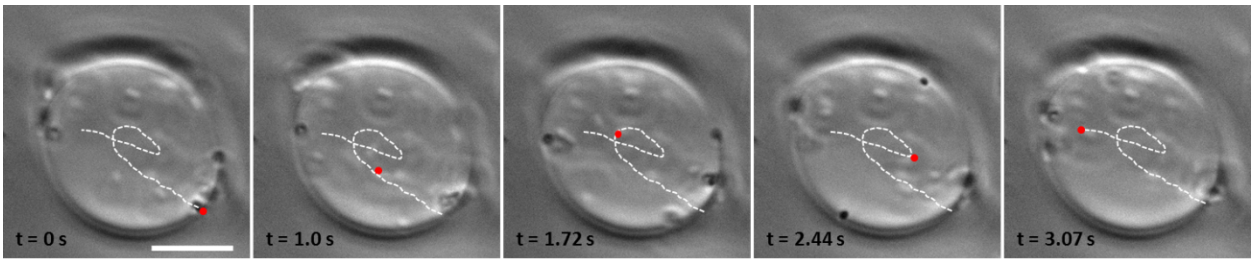


**Fig. S5**

**Figure S6.** Temporal accumulation of motile bacteria at the interface of isotropic tactoids. (A and B) Bright field and crossed polars images, respectively of motile *P. mirabilis* cells dispersed in DSCG solution quenched to 33°C that contains nematic tactoids encompassed by isotropic phase solution. (C and D) Bright field and crossed polars images, respectively of motile *P. mirabilis* cells dispersed in DSCG solution heated to 30°C that contains isotropic tactoids surrounded by a continuous nematic phase. All images were obtained following 15 min of equilibration at the specified temperatures. Scale bars are 20 μm.

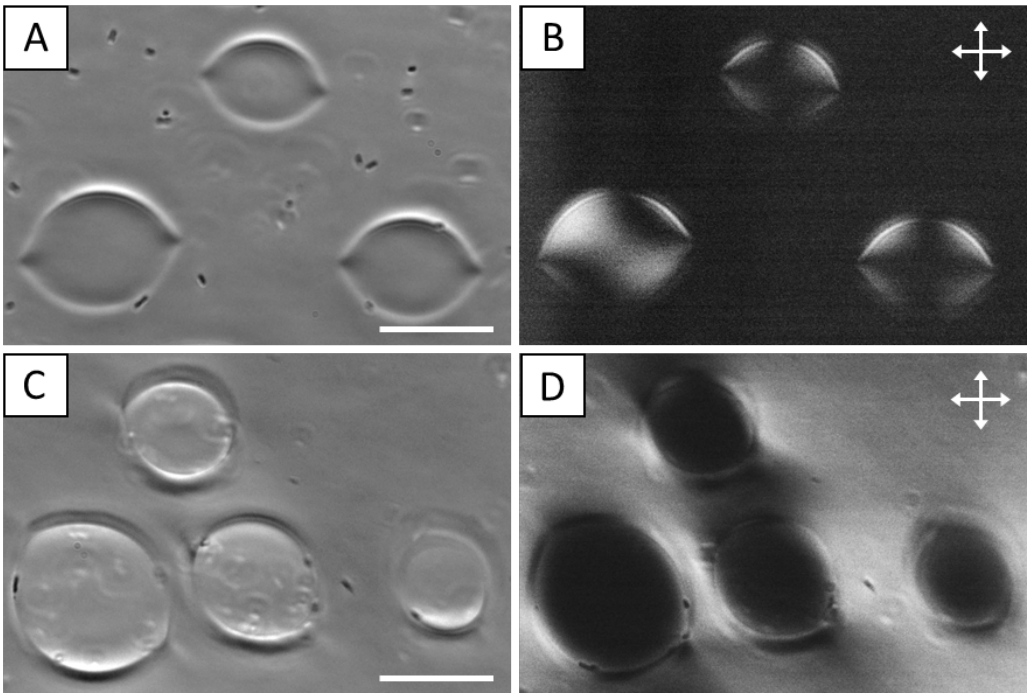


**Fig. S6**

**Table 1 Velocity of *P. mirabilis* in bulk DSCG phases and N-I interfaces.**

| Location | Temperature | Estimated Viscosity (mPa·s) | Velocity (μm/s) |
|---|---|---|---|
| Bulk nematic | 25°C | 700[†] | 8.8 +/- 0.2[*] |
| Bulk nematic | 30°C | 650[†] | 9.5 +/- 0.6 |
| Bulk isotropic | 33°C | 9[‡] | 17.6 +/- 0.7 |
| Bulk isotropic | 42°C | 2[‡] | 8.1 +/- 0.3[*] |
| N-I interface (isotropic tactoid) | 30°C | | 16.7 +/- 0.5 |
| N-I interface (nematic tactoid) | 33°C | | 17.1 +/- 0.4 |

[*] Data taken from (40).

[†] Estimated based on comparison of velocity of *P. mirabilis* cells in 15 wt% DSCG to previous measurements (38) of *P. mirabilis* motility in isotropic solutions of known viscosity.

[‡] Estimated based on measurements of the shear viscosity of aqueous solutions of 14 wt% DSCG (46).

**Movie Captions**

**Movie S1**

Bright field optical microscopy movie in which the trajectories of motile *P. mirabilis* cells adsorbed to the N-I interface of a nematic tactoid largely map out the interfacial director profile of the tactoid. Additionally, bacteria can be observed escaping the interface at the cusped poles of the tactoids where a boojum is present. Scale bar = 10 μm.

**Movie S2**

Bright field optical microscopy movie in which a single motile *P. mirabilis* cell adsorbed to the N-I interface of an isotropic tactoid escapes into the continuous nematic phase at the cusped pole of the tactoid, which is adjacent to a boojum defect in the nematic phase. Scale bar = 10 μm.

**Movie S3**

Bright field optical microscopy movie that shows accumulation of motile *P. mirabilis* adsorbed to the N-I interface of an isotropic tactoid at the cusp-shaped pole. The large aggregate of cells collectively escape into the continuous nematic phase. Scale bar = 10 μm.

**Movie S4**

Bright field optical microscopy movie that shows the accumulation of motile *P. mirabilis* within and at the N-I interface of a large isotropic domain that spans the entire thickness of the experimental cell. This isotropic domain formed by quenching the 15 wt% DSCG solution from 40°C to 30°C. Scale bar = 20 μm.

**References**


1. Lens, P., A. P. Moran, T. Mahony, P. Stoodley, and V. O'Flaherty editors. 2003. Biofilms in Medicine, Industry and Environmental Biotechnology: Characteristics, Analysis and Control. IWA Publishing, London.

2. Parsek, M. R., and P. K. Singh. 2003. Bacterial biofilms: an emerging link to disease pathogenesis. Annu. Rev. Microbiol. 57: 677–701.

3. Hall-Stoodley, L., J. W. Costerton, and P. Stoodley. 2004. Bacterial biofilms: from the natural environment to infectious diseases. Nat. Rev. Microbiol. 2: 95–108.

4. Hallam, N. B., J. R. West, C. F. Forster, and J. Simms. 2001. The potential for biofilm growth in water distribution systems. Water Res. 35: 4063–4071.

5. Oostdijk, E. A. N., A. M. G. A. de Smet, H. E. M. Blok, E. S. Thieme Groen, G. J. van Asselt, R. F. J. Benus, S. A. T. Bernards, I. H. M. E. Frénay, A. R. Jansz, B. M. deJongh, J. A. Kaan, M. A. Leverstein-van Hall, E. M. Mascini, W. Pauw, P. D. J. Sturm, S. F. T. Thijsen, J. A. J. W. Kluytmans, and M. J. M. Bonten. 2010. Ecological effects of selective decontamination on resistant gram-negative bacterial colonization. Am. J. Respir. Crit. Care Med. 181: 452–457.

6. Chmielewski, R. A. N., and J. F. Frank. 2003. Biofilm formation and control in food processing facilities. Compr. Rev. Food Sci. Food Saf. 2: 22–32.

7. Shi, X., and X. Zhu. 2009. Biofilm formation and food safety in food industries. Trends Food Sci. Technol. 20: 407–413.

8. Johansson, J. F., L. R. Paul, and R. D. Finlay. 2004. Microbial interactions in the mycorrhizosphere and their significance for sustainable agriculture. FEMS Microbiol. Ecol. 48: 1–13.

9. Evans, F. F., A. S. Rosado, G. V Sebastián, R. Casella, P. L. O. A. Machado, C. Holmström, S. Kjelleberg, J. D. van Elsas, and L. Selding. 2004. Impact of oil contamination and biostimulation on the diversity of indigenous bacterial communities in soil microcosms. FEMS Microbiol. Ecol. 49: 295–305.

10. Guarner, F., and J.-R. Malagelada. 2003. Gut flora in health and disease. Lancet. 361: 512–519.

11. Flint, H. J., S. H. Duncan, K. P. Scott, and P. Louis. 2007. Interactions and competition within the microbial community of the human colon: links between diet and health. Environ. Microbiol. 9: 1101–1111.

12. DiLuzio, W. R., L. Turner, M. Mayer, P. Garstecki, D. B. Weibel, H. C. Berg, and G. M. Whitesides. 2005. Escherichia coli swim on the right-hand side. Nature. 435: 1271–1274.

13. Lauga, E., W. R. DiLuzio, G. M. Whitesides, and H. A. Stone. 2006. Swimming in circles: motion of bacteria near solid boundaries. Biophys. J. 90: 400–412.

14. Berke, A., L. Turner, H. Berg, and E. Lauga. 2008. Hydrodynamic attraction of swimming microorganisms by surfaces. Phys. Rev. Lett. 101: 038102.

15. Lauga, E., and T. R. Powers. 2009. The hydrodynamics of swimming microorganisms. Reports Prog. Phys. 72: 096601.

16. Lemelle, L., J.-F. Palierne, E. Chatre, and C. Place. 2010. Counterclockwise circular motion of bacteria swimming at the air-liquid interface. J. Bacteriol. 192: 6307–6308.

17. Morse, M., A. Huang, G. Li, M. R. Maxey, and J. X. Tang. 2013. Molecular adsorption steers bacterial swimming at the air/water interface. Biophys. J. 105: 21–28.

18. Flemming, H.-C. 2002. Biofouling in water systems – cases, causes and countermeasures. Appl. Microbiol. Biotechnol. 59: 629–640.

19. del Pozo, J. L., and R. Patel. 2007. The challenge of treating biofilm-associated bacterial infections. Clin. Pharmacol. Ther. 82: 204–209.

20. Høiby, N., T. Bjarnsholt, M. Givskov, S. Molin, and O. Ciofu. 2010. Antibiotic resistance of bacterial biofilms. Int. J. Antimicrob. Agents. 35: 322–332.

21. Shaw, T., M. Winston, C. J. Rupp, I. Klapper, and P. Stoodley. 2004. Commonality of elastic relaxation times in biofilms. Phys. Rev. Lett. 93: 098102.

22. Flemming, H.-C., and J. Wingender. 2010. The biofilm matrix. Nat. Rev. Microbiol. 8: 623–633.

23. Madoff, L. C., S. J. Thaler, and J. H. Maguire. 2005. Infectious arthritis. *In*: Harrison's Principles of Internal Medicine, 16th ed. A. S. Fauci, D. L. Kasper, S. L. Hauser, D. L. Longo, and J. L. Jameson editors. McGraw-Hill, New York. 2050–2055.

24. Rey, A. D. 2010. Liquid crystal models of biological materials and processes. Soft Matter. 6: 3402–3429.

25. Mudd, S., and E. B. H. Mudd. 1924. The penetration of bacteria through capillary spaces. IV. A kinetic mechanism in interfaces. J. Exp. Med. 40: 633–645.

26. Mudd, S., and E. B. H. Mudd. 1924. Certain interfacial tension relations and the behavior of bacteria in films. J. Exp. Med. 40: 647–660.

27. Rosenberg, M., D. Gutnick, and E. Rosenberg. 1980. Adherence of bacteria to hydrocarbons: a simple method for measuring cell-surface hydrophobicity. FEMS Microbiol. Lett. 9: 29–33.

28. Rosenberg, M. 1984. Bacterial adherence to hydrocarbons: a useful technique for studying cell surface hydrophobicity. FEMS Microbiol. Lett. 22: 289–295.

29. Kang, Z., A. Yeung, J. M. Foght, and M. R. Gray. 2008. Hydrophobic bacteria at the hexadecane-water interface: examination of micrometre-scale interfacial properties. Colloids Surf. B. Biointerfaces. 67: 59–66.

30. Lin, I.-H., G. M. Koenig, J. J. de Pablo, and N. L. Abbott. 2008. Ordering of solid microparticles at liquid crystal-water interfaces. J. Phys. Chem. B. 112: 16552–16558.

31. Koenig, G. M., I.-H. Lin, and N. L. Abbott. 2010. Chemoresponsive assemblies of microparticles at liquid crystalline interfaces. Proc. Natl. Acad. Sci. USA. 107: 3998–4003.

32. Smalyukh, I., S. Chernyshuk, B. I. Lev, A. B. Nych, U. Ognysta, V. G. Nazarenko, and O. D. Lavrentovich. 2004. Ordered droplet structures at the liquid crystal surface and elastic-capillary colloidal interactions. Phys. Rev. Lett. 93: 117801.

33. Nazarenko, V. G., A. B. Nych, and B. I. Lev. 2001. Crystal structure in nematic emulsion. Phys. Rev. Lett. 87: 075504.

34. Gharbi, M. A., M. Nobili, M. In, G. Prévot, P. Galatola, J.-B. Fournier, and C. Blanc. 2011. Behavior of colloidal particles at a nematic liquid crystal interface. Soft Matter. 7: 1467–1471.

35. Abras, D., G. Pranami, and N. L. Abbott. 2012. The mobilities of micro- and nano-particles at interfaces of nematic liquid crystals. Soft Matter. 8: 2026–2035.

36. Mondiot, F., X. Wang, J. J. de Pablo, and N. L. Abbott. 2013. Liquid crystal-based emulsions for synthesis of spherical and non-spherical particles with chemical patches. J. Am. Chem. Soc. 135: 9972–9975.

37. Whitmer, J. K., X. Wang, F. Mondiot, D. S. Miller, N. L. Abbott, and J. J. de Pablo. 2013. Nematic-field-driven positioning of particles in liquid crystal droplets. Phys. Rev. Lett. 111: 227801.

38. Tuson, H. H., M. F. Copeland, S. Carey, R. Sacotte, and D. B. Weibel. 2013. Flagella density regulates Proteus mirabilis swarmer cell motility in viscous environments. J. Bacteriol. 195: 368–377.

39. Kumar, A., T. Galstian, S. K. Pattanayek, and S. Rainville. 2013. The motility of bacteria in an anisotropic liquid environment. Mol. Cryst. Liq. Cryst. 574: 33–39.

40. Mushenheim, P. C., R. R. Trivedi, H. H. Tuson, D. B. Weibel, and N. L. Abbott. 2014. Dynamic self-assembly of motile bacteria in liquid crystals. Soft Matter. 10: 88–95.

41. Zhou, S., A. Sokolov, O. D. Lavrentovich, and I. S. Aranson. 2014. Living liquid crystals. Proc. Natl. Acad. Sci. USA. 111: 1265–1270.

42. Kim, Y.-K., S. V Shiyanovskii, and O. D. Lavrentovich. 2013. Morphogenesis of defects and tactoids during isotropic-nematic phase transition in self-assembled lyotropic chromonic liquid crystals. J. Phys. Condens. Matter. 25: 404202.

43. Prinsen, P., and P. van der Schoot. 2003. Shape and director-field transformation of tactoids. Phys. Rev. E. 68: 021701.

44. Nastishin, Y. A., H. Liu, T. Schneider, V. Nazarenko, R. Vasyuta, S. V. Shiyanovskii, and O. D. Lavrentovich. 2005. Optical characterization of the nematic lyotropic chromonic liquid crystals: light absorption, birefringence, and scalar order parameter. Phys. Rev. E. 72: 041711.

45. Van Bijnen, R. M. W., R. H. J. Otten, and P. van der Schoot. 2012. Texture and shape of two-dimensional domains of nematic liquid crystals. Phys. Rev. E. 86: 051703.

46. Nastishin, Y. A., H. Liu, S. V. Shiyanovskii, O. D. Lavrentovich, A. F. Kostko, and M. A. Anisimov. 2004. Pretransitional fluctuations in the isotropic phase of a lyotropic chromonic liquid crystal. Phys. Rev. E. 70: 051706.

47. Champion, J. V, and G. H. Meeten. 1973. Conformation of sodium cromolyn in aqueous solution using light scattering and magnetic birefringence. J. Pharm. Sci. 62: 1589–1595.

48. Luk, Y.-Y., M. L. Tingey, D. J. Hall, B. A. Israel, C. J. Murphy, P. J. Bertics, and N. L. Abbott. 2003. Using liquid crystals to amplify protein−receptor interactions: design of surfaces with nanometer-scale topography that present histidine-tagged protein receptors. Langmuir. 19: 1671–1680.

49. Kaznacheev, A. V, M. M. Bogdanov, and S. A. Taraskin. 2002. The nature of prolate shape of tactoids in lyotropic inorganic liquid crystals. J. Exp. Theor. Phys. 95: 57–63.

50. Kaznacheev, A. V, M. M. Bogdanov, and A. S. Sonin. 2003. The influence of anchoring energy on the prolate shape of tactoids in lyotropic inorganic liquid crystals. J. Exp. Theor. Phys. 97: 1159–1167.

51. Volovik, G. E., and O. D. Lavrentovich. 1983. Topological dynamics of defects: boojums in nematic drops. Sov. Phys. JETP. 58: 1159–1166.

52. Nastishin, Y. A., K. Neupane, A. R. Baldwin, O. D. Lavrentovich, and S. Sprunt. 2008. Elasticity and viscosity of a lyotropic chromonic nematic studied with dynamic light scattering. Electronic-Liquid Crystal Communications. arXIV.org/abs/0807.2669.

53. Prinsen, P., and P. van der Schoot. 2004. Parity breaking in nematic tactoids. J. Phys. Condens. Matter. 16: 8835–8850.

54. Tortora, L., and O. D. Lavrentovich. 2011. Chiral symmetry breaking by spatial confinement in tactoidal droplets of lyotropic chromonic liquid crystals. Proc. Natl. Acad. Sci. USA. 108: 5163–5168.

55. Chen, W., and D. G. Gray. 2002. Interfacial tension between isotropic and anisotropic phases of a suspension of rodlike particles. Langmuir. 18: 633–637.

56. Binks, B. P., and T. S. Horozov. 2006. Colloidal particles at liquid interfaces: An introduction. *In*: Colloidal Particles at Liquid Interfaces. Binks, B. P., and T. S. Horozov editors. Cambridge University Press, Cambridge. 1-15.

57. Smalyukh, I. I., J. Butler, J. D. Shrout, M. R. Parsek, and G. C. L. Wong. 2008. Elasticity-mediated nematiclike bacterial organization in model extracellular DNA matrix. Phys. Rev. E. 78: 030701.

58. West, J. L., A. Glushchenko, G. Liao, Y. Reznikov, D. Andrienko, and M. P. Allen. 2002. Drag on particles in a nematic suspension by a moving nematic-isotropic interface. Phys. Rev. E. 66: 012702.

# CHAPTER 5

## Bacterial transport of colloids in liquid crystalline environments.

Adapted from

Trivedi, R.R., Maeda, R., Abbott, N.L., Spagnolie, S.E. and Weibel, D.B., 2015. Bacterial transport of colloids in liquid crystalline environments. *Soft matter*, *11*(43), pp.8404-8408.

**Abstract**

We describe the controlled transport and delivery of non-motile eukaryotic cells and polymer microparticles by swimming bacteria suspended in nematic liquid crystals. The bacteria push reversibly attached cargo in a stable, unidirectional path (or along a complex patterned director field) over exceptionally long distances. Numerical simulations and analytical predictions for swimming speeds provide a mechanistic insight into the hydrodynamics of the system. This study lays the foundation for using cargo-carrying bacteria in engineering applications and for understanding interspecies interactions in polymicrobial communities.

## Introduction

The manipulation of microscale structures is an unsolved challenge in microengineering and microtechnology. One approach has been to harness the mechanical work performed by cells, which takes advantage of their metabolism and motility machinery to convert chemical energy to motion in a wide range of chemical and physical environments[1]. Extracellular sensors enable cells to adapt and navigate through different environments, thereby providing mechanisms to control their motion and the objects they are moving. The earliest examples of research in this area include the movement of polymer structures with length scales of hundreds of microns by bacterial cells adsorbed on the polymer surface[2], and the guided transport and release of polymer colloids by individual phototactic, motile algae[3]. Related efforts have included magnetically-driven transport of cargo by synthetic swimmers with possible applications in targeted drug delivery[4].

Bacteria have been the source of additional studies on microstructure transport as they are fast (velocities approaching $\approx$100 $\mu$m/sec) and adaptable, genetic tools are widely available for engineering their properties and behavior, and a range of mechanisms can be exploited to control their motion, including: concentration gradients of ions and chemicals, magnetic fields, light, heat, oxygen, and redox potential[5,6]. Many rod-shaped bacteria swim through fluids by rotating their flagella in a counterclockwise direction to form a bundle and 'run'. Rotating a flagellum in the clockwise direction alters the structure of the bundle and reorients cells, which creates an event referred to as a 'tumble'. Controlling the motion of many flagellated bacteria is complicated by run and tumble dynamics[7]; accordingly, bacteria-based motility of microscale objects is highly challenging, as it is difficult to place objects on cells without disrupting and inhibiting normal cell behavior. Applications relying on chemotaxis to move small cargo pose similar challenges due to

spatial and temporal instability of chemical gradients[8]. Confined domains such as microfluidic channels can also influence particle trajectories[9].

A new method for directing bacterial motion without channels or gradients was recently developed, in which motile bacteria are suspended in solutions of nematic, lyotropic liquid crystals (LCs) consisting of disodium cromoglycate (DSCG)[10,11]. In nematic LCs, bacteria were found to align with and swim along the nematic director field[10–12], which suggests a new way to harness microorganisms as biological engines. A recent paper demonstrated that a bacterial cell swimming in a nematic LC can influence the position of polymer microspheres through long-range hydrodynamic interactions[13].

In this study we describe the environmental relevance of the controlled transport and delivery of microparticles by swimming bacteria. We show that freely swimming *P. mirabilis* bacteria can push non-motile fungal cells in a a stable, unidirectional path over long distances. By patterning a complex director profile in the fluid, the bacteria and cargo may be guided along a predefined path. Experiments with polymer microparticles, numerical simulations based on isotropic viscous flow, and analytical predictions for swimming speeds of cargo-pushing bacteria provide mechanistic insight and emphasize the importance of hydrodynamic interactions in the system. This study lays the foundation for using cargo-carrying bacteria in unique ways, from the bottom-up assembly of mesoscopic materials to the study of interspecies interactions in polymicrobial communities in anisotropic biological environments such as mucus and biofilms.

## Materials and Methods

### Materials

DSCG (>95%) was from Sigma. Polystyrene microparticles with diameters of 1, 1.75 (fluorescent), 2, and 3 $\mu$m were from Polysciences. We rinsed microparticles with motility buffer [0.01 M $KPO_4$, 0.067 M NaCl, $10^{-4}$ M EDTA (pH 7.0)] before performing experiments.

### Bacterial and yeast strains and cell culture

*P. mirabilis* strain HI4320 over-expressing the pflhDC plasmid was used in this study. HI4320 is a clinical strain isolated from a patient with urinary catheter-associated bacterial infection. The pflhDC plasmid contains the flhDC genes encoding the expression of FlhD and FlhC, and was inserted into pACYC184. pflhDC plasmid was transformed into wild- type strain HI4320 by electroporation and transformants were selected on lysogeny broth (LB) (1% [w/v] tryptone, 0.5% [w/v] yeast extract, and 1% [w/v] NaCl) agar plates (3% [wt/vol]) containing chloramphenicol (34 $\mu$g mL$^{-1}$). Overnight culture of *P. mirabilis*-flhDC cells were grown in nutrient rich medium consisting of 1% (wt/vol) peptone (Becton, Dickinson, Sparks, MD), 0.5% (wt/vol) yeast extract (Becton, Dickinson), and 1% (wt/vol) NaCl (Fisher Scientific, Fairlawn, NJ) with 34 $\mu$g mL$^{-1}$ of chloramphenicol for 12-16 h at 30 °C with agitation (200 rpm). Saturated overnight culture was diluted (1:100) in fresh growth media containing 34 $\mu$g mL$^{-1}$ of chloramphenicol, incubated at 30 °C with agitation (200 rpm) for 4 h until the absorbance ($\lambda$=600 nm) reached 3.0 to harvest cells at their peak motility. Colonies of *Candida albicans* cells were grown LB agar plates, picked directly, and suspended in liquid for experiments.

**Lyotropic LC preparation**

Disodium cromoglycate (DSCG) was purchased from Sigma-Aldrich (Milwaukee, WI) and used as received. Lyotropic LCs containing DSCG were prepared by mixing 15.3 wt% of DSCG with 84.7 wt% of aqueous motility buffer. The mixture was shaken for at least 12 h to ensure complete solubility and homogeneity. Prior to experimentation, the DSCG solution was heated at 65°C for 10 min to avoid possible time dependence of the properties of the mixture by melting the LC solution homogeneously. After cooling the solution to 25°C, a small volume of motility buffer containing bacteria and microparticles was added to the DSCG mixture to get final 15.0 wt% DSCG concentration for all experiments.

**Measuring the velocity of cells pushing microparticles**

We measured the velocity of individual *P. mirabilis* cells (in $\mu$m s$^{-1}$) using the ImageJ manual tracking plugin[S1]. A 1 mL aliquot of a suspension of cultured cells (absorbance of 3.0-3.5, $\lambda$ = 600 nm) was concentrated by centrifugation for 5 min at 1000 rpm at 25 °C, and the cell pellet was gently resuspended in 50 $\mu$L of motility buffer containing 0.1 M glucose and 0.001% (w/v) Brij-35. 40$\mu$L stock solution of microparticles were washed twice in the motility buffer and resuspended in 200$\mu$L of motility buffer. Microparticles and cell suspension were added in 1:1 ratio in 15.3 wt% DSCG stock solution. After gently mixing LC, microparticles and bacteria, 1 $\mu$L of the solution was spotted on a pre-cleaned slide glass with two spacers (18-$\mu$m thick). The experimental chamber was covered with a 1.5 mm glass coverslip and sealed with Epoxy. We imaged cell motility using a Nikon Eclipse Ti equipped with a Photometrics CoolSNAP HQ2 CCD camera (Photometrics, Tucson, AZ). Images were acquired using a $\times$100 (Nikon Plan APO) oil immersion objective and the NIS-Elements AR microscope imaging software program (Version 4.000.07) (Nikon, Melville,

NY). Videos were collected at 11.05 frames per second with 100ms exposure time and EM gain off.

## Mathematical model

## Numerical simulations

While the fluid anisotropy in the experiments clearly results in alignment and stability of the microorganism/cargo system, we studied a simpler model for the viscous flow, the isotropic Stokes equations, $\nabla p = \mu \nabla^2 \mathbf{u}$ and $\nabla \cdot \mathbf{u} = 0$, where $\mathbf{u}$ is the fluid velocity, $\mu$ is the viscosity, and $p$ is the pressure. The two equations represent conservation of momentum and mass, respectively. A fundamental (Green's function) solution to the Stokes equations is derived by inserting a point force $\mathbf{f}$ at a point $\mathbf{x}_0$ in an infinite fluid and solving $\nabla p = \mu \nabla^2 \mathbf{u} + \mathbf{f}\delta(\mathbf{x}_0)$, where $\delta(\mathbf{x}_0)$ is a Dirac delta function (see [S2]). The resulting velocity field is given by

$$\mathbf{u}(\mathbf{x}) = \mathbf{G}(\mathbf{x}, \mathbf{x}_0) \cdot \mathbf{f}, \tag{1}$$

where

$$\mathbf{G}(\mathbf{x}, \mathbf{x}_0) = \frac{1}{8\pi\mu} \left( \frac{\mathbf{I}}{r} + \frac{\mathbf{RR}}{r^3} \right) \tag{2}$$

is known as the Stokeslet singularity. Here $\mathbf{I}$ the identity operator, $\mathbf{R} = \mathbf{x} - \mathbf{x}_0$, $r = |\mathbf{R}|$, and $\mathbf{RR}$ is a dyadic product.

To compute the flow due to the motion of the cell body and spherical cargo driven by a line distribution of forcing, e employ the method of regularized Stokeslets by Cortez[S3,S4]. A regularized Stokeslet is a smooth approximation to (2), constructed by solving the Stokes equations instead with

a smoothed point force at $\mathbf{x}_0$, resulting in the solution $\mathbf{u}(\mathbf{x}) = \mathbf{G}_\delta(\mathbf{x},\mathbf{x}_0)\cdot\mathbf{f}$, where

$$\mathbf{G}_\delta(\mathbf{x},\mathbf{x}_0) = H_1(r)\mathbf{I} + H_2(r)\mathbf{RR}, \tag{3}$$

$$H_1(r) = \frac{1}{8\pi\mu}\left(\frac{1}{(r^2+\delta^2)^{1/2}} + \frac{\delta^2}{(r^2+\delta^2)^{3/2}}\right), \quad H_2(r) = \frac{1}{8\pi\mu}\frac{1}{(r^2+\delta^2)^{3/2}}, \tag{4}$$

where $\delta$ is a small regularization parameter.

We compute the fluid flow on the microswimmer/cargo system by distributing regularized Stokeslet singularities on the surface of the cargo $D_c$, the surface of the cell body $D_b$, and along the length of the flagellum, $D_f$. The strengths $\mathbf{f}(\mathbf{x})$ of the singularities at each position are determined by the boundary conditions. Namely, the velocity is assumed to satisfy a no-slip condition on the cell body and cargo surfaces, so that $\mathbf{u} = \mathbf{U} + \boldsymbol{\Omega}\times\mathbf{x}$ there, with $\mathbf{U}$ the (as yet unknown) swimming speed and $\boldsymbol{\Omega}$ is a rotation rate. On the flagellum, however, we specify the force distribution directly there with a strength $f$ per unit length. With the symmetric system aligned with $\hat{\mathbf{x}}$, this results in a slip velocity $u_s(s)\hat{\mathbf{x}}$ along the flagellum (see[S5]) where $s$ is an arc-length parameter. To close the system we require there to be zero net force and zero net torque on the system. To summarize, we must invert the following system to determine the force distribution $\mathbf{f}$ on the load, the slip velocity $u_s$ on the flagellum, the swimming speed $\mathbf{U}$ and the rotation rate $\boldsymbol{\Omega}$:

$$\mathbf{U} + \boldsymbol{\Omega}\times\mathbf{x} = \sum_{k=1}^{N}\mathbf{G}_\delta(\mathbf{x},\mathbf{y}_k)\cdot\mathbf{f}(\mathbf{y}_k) \quad \mathbf{x}\in D_b\cup D_c, \tag{5}$$

$$\mathbf{U} + \boldsymbol{\Omega}\times\mathbf{x} + u_s(s)\hat{\mathbf{x}} = \sum_{k=1}^{N}\mathbf{G}_\delta(\mathbf{x},\mathbf{y}_k)\cdot\mathbf{f}(\mathbf{y}_k) \quad \mathbf{x}\in D_f, \tag{6}$$

$$\mathbf{f}(\mathbf{x}) = -hf\hat{\mathbf{x}} \quad \mathbf{x}\in D_f, \tag{7}$$

$$\sum_{k=1}^{N}\mathbf{f} = \mathbf{0}, \quad \sum_{k=1}^{N}\mathbf{x}\times\mathbf{f} = \mathbf{0}. \tag{8}$$

The $N$ points $\mathbf{y}_k$ are evenly distributed around the cell body, cargo, and flagellum so that the spacing between points, including the spacing between the cargo and the cell body, and the cell body and the flagellum, are equally spaced by a distance $h$. The system is solved by forming the linear matrix problem and inverting directly. Selecting the value of the regularization parameter is an artform; we use a form for $\delta$ used by Cortez et al.[S4] which resulted in acceptable results in various test problems, $\delta = 0.22h^{0.9}$. By symmetry we expect $\mathbf{U} = U\hat{\mathbf{x}}$ and $\mathbf{\Omega} = \mathbf{0}$, which is confirmed in the computations. The value of $N$ is chosen so that increasing $N$ results in a departure from the presented results confined to within 5% of the reported values; generally this requires $N \approx 1000$.

In order to match the experiments we choose a cell body with aspect ratio $B/A = 0.4$, relative flagellum lengths $L/A$ ranging from 2 to 8, and relative cargo sizes $A_c/A$ ranging from 0 to 2. The swimming speed of *P. mirabilis* in the experiments, absent cargo, is approximately $U = 9.6\ \mu$m/s, which we use to calibrate the force per unit length on the flagellum $f$. Using $L/A = 5$, we find approximately $f/\mu = 26.9\ \mu$m/s. The viscosity measured in the experiments, $\mu = 0.7$ Pa·s enters only to scale the force $\mathbf{f}$ and as such we neglect its inclusion; it's scale is implicit in the calibration process. The value $f$ is the only fitting parameter used in the model.

**Analytical estimate**

We now describe three analytical estimates, each more accurate than the previous one. To obtain the simplest possible estimate of the swimming speed, we treat the total load (the cell body and cargo) as a single immersed sphere with an effective radius $\rho$, chosen so that the drag on the load moving with speed $U$ (and with no flagellum) is given by $6\pi\mu\rho U$. For $A_c/A \gg 1$ we have $\rho \approx A_c$. For smaller values of $A_c$, we estimate the total drag on the load as the sum total of the drag on each component, neglecting hydrodynamic interactions, so that $\rho = A_c + K_e A$, where $e = \sqrt{1-(B/A)^2}$ is the

eccentricity of the cell body, and

$$K_e = \frac{8e^3}{-6e + 3(1+e^2)\log[(1+e)/(1-e)]}. \tag{9}$$

This is the exact expression for the drag on a prolate spheroid (see[S6]). With $B/A = 0.4$ we have $K_e \approx 0.522$. Neglecting hydrodynamic interactions with the flagellum, this expression may be used as the basis for an estimate of the swimming speed by simply insisting that the total force on the load is the total force generated by the flagellum, $F$, so that

$$U = \frac{F}{6\pi\mu\left(A_c + K_e A\right)}. \tag{10}$$

However, as shown in Fig. S5, where the computed values and estimate above are shown as solid and dashed lines, respectively, it is clear that this is a rather inaccurate estimate.

To obtain a more accurate approximation we include the leading order correction in a far-field expansion, now making the approximation that the cell body and cargo are well-separated. Writing the force on the cell-body as $F_b$ and the force on the cargo as $F_c$, we have

$$F_b = 6\pi\mu A K_e \left(U - u_c(\mathbf{x}_0)\right) + O\left(A^2\nabla^2 u_c\right), \tag{11}$$

$$F_c = 6\pi\mu A_c \left(U - u_b(\mathbf{x}_0 + (A + A_c)\hat{\mathbf{x}})\right) + O\left(A_c^2\nabla^2 u_b\right), \tag{12}$$

where $F_b + F_c = F$, and $u_c$ and $u_b$ are the velocity fields due to the motion of each component of the load separately (in an infinite fluid with no hydrodynamic interactions). The leading order flow field

is given by the Stokeslet, i.e.

$$u_c(\mathbf{x}_0) = \hat{\mathbf{x}} \cdot \mathbf{G}(\mathbf{x}_0, \mathbf{x}_0 + (A + A_c)\hat{\mathbf{x}}) \cdot F_c \hat{\mathbf{x}}, \tag{13}$$

$$u_b(\mathbf{x}_0 + (A + A_c)\hat{\mathbf{x}}) = \hat{\mathbf{x}} \cdot \mathbf{G}(\mathbf{x}_0 + (A + A_c)\hat{\mathbf{x}}, \mathbf{x_0}) \cdot F_b \hat{\mathbf{x}}. \tag{14}$$

Combining the above, we find

$$F_b = \frac{AF(2A - A_c)K_e}{2A(A - 2A_c)K_e + 2A_c(A + A_c)}, \tag{15}$$

$$F_c = \frac{A_c F(2(A + A_c) - 3AK_e)}{2A(A - 2A_c)K_e + 2A_c(A + A_c)}, \tag{16}$$

$$U = \frac{F\left(4(A + A_c)^2 - 9AA_cK_e\right)}{24\pi\mu(A + A_c)(A(A - 2A_c)K_e + A_c(A + A_c))}, \tag{17}$$

matching the drag on a sphere of radius

$$\rho = \frac{4(A + A_c)(A(A - 2A_c)K_e + A_c(A + A_c))}{4(A + A_c)^2 - 9AA_cK_e}. \tag{18}$$

This estimated swimming speed in (17) included as a dot-dashed line in Fig. S5, where it is seen to be a much more accurate approximation than (10).

While the estimate above is acceptable for the drag on the load, in the full swimming problem with flagellar forcing the prediction is inaccurate. As discussed in the main text, and shown in Fig. 4 there, it is important to include the hydrodynamic interaction of the flagellum with the load. Neglecting the flow due to the flagellum results in a considerable overestimate of the swimming speed. We therefore use the same approach as before but now we include the flow due to the nearly

flagellum at leading order in a far-field calculation,

$$F_b = 6\pi\mu A K_e \left(U - u_c(\mathbf{x}_0) - u_f(\mathbf{x}_0)\right), \tag{19}$$

$$F_c = 6\pi\mu A_c \left(U - u_b(\mathbf{x}_0 + (A+A_c)\hat{\mathbf{x}} - u_f(\mathbf{x}_0 + (A+A_c)\hat{\mathbf{x}})\right), \tag{20}$$

where $F_b + F_c = F$ and $u_f$ is a single Stokeslet of strength $F$ placed at the center of the flagellum. This results in

$$\left(\frac{6\pi\mu A}{F}\right) U = \frac{C(\kappa,\lambda)}{D(\kappa,\lambda)}, \tag{21}$$

where

$$C(\kappa,\lambda) = 4(\kappa+1)^2(\lambda+2)(4+\lambda-\kappa) + 3K_e\left\{\kappa\left(4\left(\kappa^2+\kappa-7\right)+2(\kappa-7)\lambda-3\lambda^2\right)-4(\lambda+4)\right\} \tag{22}$$

$$D(\kappa,\lambda) = 4(\kappa+1)(\lambda+2)(2\kappa+\lambda+4)\left(\kappa^2+\kappa-2\kappa K_e+K_e\right), \tag{23}$$

with $\kappa = A_c/A$ and $\lambda = L/A$. Without cargo the swimming speed is given by (taking $\kappa \to 0$),

$$\left(\frac{6\pi\mu A K_e}{F}\right) U = 1 - \frac{3K_e}{2+\lambda}. \tag{24}$$

**Results and Discussion**

It has been suggested that motile microorganisms may transport non-motile cells in different ecological niches to increase their adaptation, fitness, and survival[6,14]. Both *P. mirabilis* and the non-motile fungus *C. albicans* are opportunistic pathogens that are associated with urinary tract infections (UTI) and have been isolated from UTI patients[15]. The urinary tract is lined with a layer of mucus secreted by the urinary epithelium, which under conditions of external flow (i.e., flow of fluid adjacent to the mucus) may align molecules to exhibit orientational order similar to nematic LCs and guide cell motion. Fluid anisotropy has also been reported in cervical mucus due to the ordering of parallel strands of polymers[16], which may guide sperm cells entering the cervical canal to follow the mucus 'director'[17]. We used the nematic LC to mimic the physical properties of the epithelial mucus and study whether *P. mirabilis* cells push *C. albicans* cells in long-range, rectified motion in a simple mechanical model of the mammalian urinary tract.

As a model anisotropic fluid we used aqueous solutions of 15 wt% DSCG due to its biocompatibility with bacteria[18]. DSCG forms nematic-phase LCs at room temperature which is well suited for bacterial growth and motility[19]. An isotropic phase of DSCG was achieved by heating the sample to 30°C. For our studies we used *P. mirabilis* strain HI4320 (with cell body widths ≈0.5 $\mu$m and lengths ≈2-3-$\mu$m), a clinical isolate collected from an elderly patient with a long-term in-dwelling urinary catheter[20]. We engineered cells to overexpress the flhDC operon, which encodes the master regulator of flagella biosynthesis, FlhD4C2 to match the density of flagella expressed by *P. mirabilis* swarmer cells implicated in urinary tract infections (UTIs)[21].

We mixed motile *P. mirabilis* cells with non-motile *C. albicans* cells (5-$\mu$m in diameter) and

suspended them in ≈20$\mu$m-thick nematic LC sandwiched between two rubbed coverslips, and imaged cell behavior using phase contrast microscopy (Fig. S1). Single *P. mirabilis* cells pushed *C. albicans* cells along the far-field director with a speed of ≈1-2 $\mu$m/s, which is fast enough to disperse yeast cells to relatively long distances of ≈5 mm over the course of an hour (Fig. 1a). We then engineered a 'complex' LC director profile by rubbing the glass in a curved pattern and observed motile *P. mirabilis* cells pushing *C. albicans* cells over distances of hundreds of microns that followed the director (Fig. 1b, Fig. S3). In addition to individual *P. mirabilis* cells pushing single *C. albicans* cells, we also observed multiple bacterial cells pushing groups of dividing fungal cells. In these experiments, the nematic LC promotes particle/particle interactions (between *P. mirabilis* and *C. albicans*), active particles provide the mechanical work for movement along the LC director, and passive particles provide a physical barrier that inhibits bacterial cell tumbling that would ordinarily lead to direction reversal. Consequently the pair of *P. mirabilis* and *C. albicans* cells are locked in a long-range motile run in LCs that eclipses the net distance achievable by either of the individual cells.

To better understand cargo transport in a more controlled experiment, we mixed *P. mirabilis* cells and 2-$\mu$m-diameter polystyrene microparticles, and observed many cells pushing microparticles along the far-field nematic director over long distances (Fig. 2). Microparticles were always positioned at the 'front' of (and pushed by) the motile cells. In a typical experiment we used a stoichiometry of 1:1 ratio of cells:particles and observed ≈10-15% of the cells moving particles at a mean velocity of ≈5 $\mu$m/s. In an isotropic LC, individual *P. mirabilis* cells were in contact with 2-$\mu$m-diameter microparticles for a "carry" time (mean run time with the cargo) of 0.18±0.1s, whereas in a nematic LC, the carry time was 460±50 s, corresponding to transport distances of

nearly 2000 body lengths. The elasticity of the LC environment inhibits bacterial reorientation, leading to robust particle transport.

Elastic forces exerted on suspended particles in nematic LCs can explain differences in the carry time in isotropic and nematic phases. Mechanical anisotropy of the nematic LC aligns cells with their long-axis parallel to the far-field director profile. When cells in a nematic LC 'tumble', their swimming direction changes by 180° [10]. We compared the frequency of cell reversals in isotropic and nematic LCs (for 100 cells) and observed 100% of the cells in the isotropic LC tumble multiple times over a 5 minute timeframe compared to 78% cells in a nematic LC (180° reversal). This reduction from 100% to 78% can be rationalized in terms of the extra elastic forces on the flagellum due to the environmental anisotropy [22]: the flagellar bundle is likely unable to splay and cause cell body reorientation in a viscoelastic medium. Reversals in a nematic LC are then primarily driven by the competing activity of two flagellar bundles on opposite sides of the cell body. However, when the bacteria in the nematic LC were pushing 2-$\mu$m-diameter microparticles, we observed a dramatic drop in the number of reversing cells during the same timeframe to only 3% (Fig. 2). This more pronounced decrease may be due to the flagellar bundle positioned at the front of the cell (in contact with the microparticle) becoming non-functional.

We also studied the bacterial transport of microparticles of different sizes to probe the relative flagellar forces and resultant swimming speeds. Fig. 3a shows the swimming speeds using microparticles ranging from 1-3 $\mu$m in diameter (shown as circles with standard error bars). With no microparticle load the mean swimming speed of *P. mirabilis* was 9.6 $\mu$m/s. Upon the addition of microparticles, the speeds decreased monotonically with increasing particle size, to values 7.2, 5.2,

and 1.5 $\mu$m/s for diameters 1, 2, and 3 $\mu$m. Fluctuations in the swimming speed were observed on a short timescale (the normal timescale of tumbling events) and over a longer timescale (time series examples are provided in the Fig S4). Swimming speeds while pushing a 2$\mu$m-diameter microparticle fluctuated with a standard deviation of approximately 1.35 $\mu$m/s, suggesting a time $\approx$ 1s beyond which the distance travelled due to the mean swimming speed dominates the distance travelled due to fluctuations. The nonlinear progression of motion shown in Fig. 2 is associated with such fluctuations.

While the fluid anisotropy in the experiments clearly results in alignment and stability of the system, we studied a mathematical model describing a simpler isotropic viscous flow, the Stokes equations, $\nabla p = \mu\nabla^2\mathbf{u}$, $\nabla\cdot\mathbf{u} = 0$, where $\mathbf{u}$ is the fluid velocity, $\mu$ is the viscosity, and $p$ is the pressure. Inertial forces are dominated by viscous forces in flows relevant to microorganism locomotion[23]. A fundamental (Green's function) solution to these equations, associated with the placement of a point force in an infinite quiescent fluid at a point $\mathbf{x}_0$, is known as the Stokeslet, $8\pi\mu\mathbf{u}(\mathbf{x}) = \mathbf{G}(\mathbf{x},\mathbf{x}_0)\cdot\mathbf{f}$, where $\mathbf{G}(\mathbf{x},\mathbf{x}_0) = \left(r^{-1}\mathbf{I} + r^{-3}\mathbf{rr}\right)$, where $\mathbf{I}$ is the identity, $\mathbf{r} = \mathbf{x} - \mathbf{x}_0$, and $r = |\mathbf{r}|$[24]. The cell body and microparticle are discretized uniformly in space, (see Fig. 3b); to model the flagellum we follow Ref.[25] and represent the averaged forcing as a uniform line distribution of Stokeslets.

To compute the full hydrodynamics we employ the method of regularized Stokeslets[26], wherein smoothed versions of the singular solution are distributed over the surfaces of the model cell body and microparticle, with strengths determined so that the no-slip velocity boundary condition is satisfied. The equations are closed by requiring the net force on the system to be zero, a consequence of neutrally buoyant locomotion at small length scales[23]. Further details about the numerical method

are included in the supplementary material.

We used experimentally motivated parameters: a cell body with length $2A = 2\mu$m, width $2B = 0.8\mu$m, flagellum length $L = 5\mu$m, and microparticle radii $A_c \in [0, 2.5]\mu$m. The model requires a single fitted parameter, the force $F$ generated by the flagellum, which we selected so that the swimming speed of the model microorganism with no microparticle matches the experimentally measured value, $U = 9.6\ \mu\text{m/s}$. Using the measured viscosity, $\mu = 0.7$ Pa·s, this requisite flagellar force is computed to be $F = 134.5$ pN, which is comparable to the elastic forces and flagella-derived forces measured in previous experiments[10].

The results of the numerical simulations are shown as a solid line in Fig 3a, where the model clearly shows the trend of decreasing speed with increasing microparticle sizes. The agreement between the experiments and the numerical simulation, even using the isotropic Stokes equations, is reasonable, save for the notable overestimation of the speed for the cargo of diameter $3\mu$m. The numerical simulations are highly suggestive of the importance of hydrodynamic interactions between the flagellum and the cell body/cargo load. Fig. 4 shows the speed of the total load as driven by an attached flagellum (solid line) and by a very distant flagellum (dashed line). The predicted swimming speed can be remarkably different; similarly, any estimate of the flagellar force imposed onto such a load may be quite inaccurate if hydrodynamic interactions are not included.

The mathematical model also offers the possibility of finding an analytical prediction of the swimming speed for variable cargo sizes, cell body shapes, and flagellum lengths. An estimate which includes the leading order hydrodynamic interactions in a far-field calculation (see

supplementary material) results in the swimming speed $U$ of the model microorganism with no microparticle given by

$$\left(\frac{6\pi\mu A K_e}{F}\right) U = 1 - \frac{3K_e}{2+\lambda}, \tag{25}$$

where $K_e = 8e^3\left(-6e + 3(1+e^2)\log[(1+e)/(1-e)]\right)^{-1}$ and $e = \sqrt{1-(B/A)^2}$. The second term on the right hand side modifies the drag coefficient on the cell body due to the flow from the flagellum. Related techniques have been used to study the hydrodynamics of locomotion near surfaces and colloidal obstacles[25,27]. Using the same geometric parameters as before, we again fit the flagellar force $F$ to match the experimental swimming speed of the cargo-less body, which in the simpler analytical model requires $F = 98.3$ pN. When a microparticle is introduced, we find a more general relation,

$$\left(\frac{6\pi\mu A}{F}\right) U = \frac{C(\kappa,\lambda)}{D(\kappa,\lambda)}, \tag{26}$$

where

$$C(\kappa,\lambda) = 4(\kappa+1)^2(\lambda+2)(4+\lambda-\kappa) + 3K_e\left\{\kappa\left(4\left(\kappa^2+\kappa-7\right)+2(\kappa-7)\lambda-3\lambda^2\right)-4(\lambda+4)\right\}, \tag{27}$$

$$D(\kappa,\lambda) = 4(\kappa+1)(\lambda+2)(2\kappa+\lambda+4)\times\left(\kappa^2+\kappa-2\kappa K_e+K_e\right), \tag{28}$$

with $\kappa = A_c/A$ and $\lambda = L/A$. The analytical prediction from Eq. (26) is included as a dashed line in Fig. 3a, showing a very clear connection to the full numerical simulations. While the isotropic model provides useful predictions in this case, the mathematical investigation of locomotion in anisotropic fluids has only recently seen attention[28] and there is a need for further study in this direction.

## Conclusion

We have demonstrated that motile bacterial cells can transport polymer microparticles and non-motile cells unidirectionally along the far-field director in lytotropic nematic LCs. There are several conclusions to be drawn from this study. 1) The LC facilitates the interaction between bacterial cells and non-motile objects, and brings them into close physical proximity while avoiding irreversible adsorption and attachment. 2) The mechanical anisotropy of a nematic LC guides the cell pushing loads along the far-field director, and the load inhibits cell reversal. 3) Non-motile organisms and cells can catch a ride on motile bacteria, suggesting a possible host invasion strategy exploited by non-motile microorganisms hitchhiking in fluidic environments. 4) Instead of using tethering assays[29], the study suggests a novel means of measuring mechanosensing responses by changing the size and shape of the passive load. 5) This method of microscale transport and manipulation is in principle material independent (e.g., polymers, silica, and cells) and does not require the engineering of cells or materials. 6) Motile bacteria may be useful as a tracer of the complex LC director profile in nematic LCs. 7) In LCs, particles are positioned at the front end of motile bacterial cells, which reduces their interference with the bundle of rotating flagella used to propel bacteria. This study demonstrates an approach for controlling the transport of microscopic objects using motile bacterial cells that may have applications that range from the bottom-up assembly of materials to the study of interspecies interactions in polymicrobial communities that occur in LC-like environments, such as biofilms.

**Acknowledgements**

This work was supported by the National Science Foundation (under awards DMR-1121288 (MRSEC), CBET-0754921, and MCB-1120832), the National Institutes of Health (CA108467 and AI092004), and the United States Department of Agriculture (WIS01594).

**Fig. 1.** (a) A single P. mirabilis cell pushes a single *C. albicans* cell along the far-field nematic LC director (n) (see Movie S1). (b) Multiple P. mirabilis cells pushing a group of *C. albicans* cells along curved path following the director profile, which is indicated by the dashed line (see Movie S2).

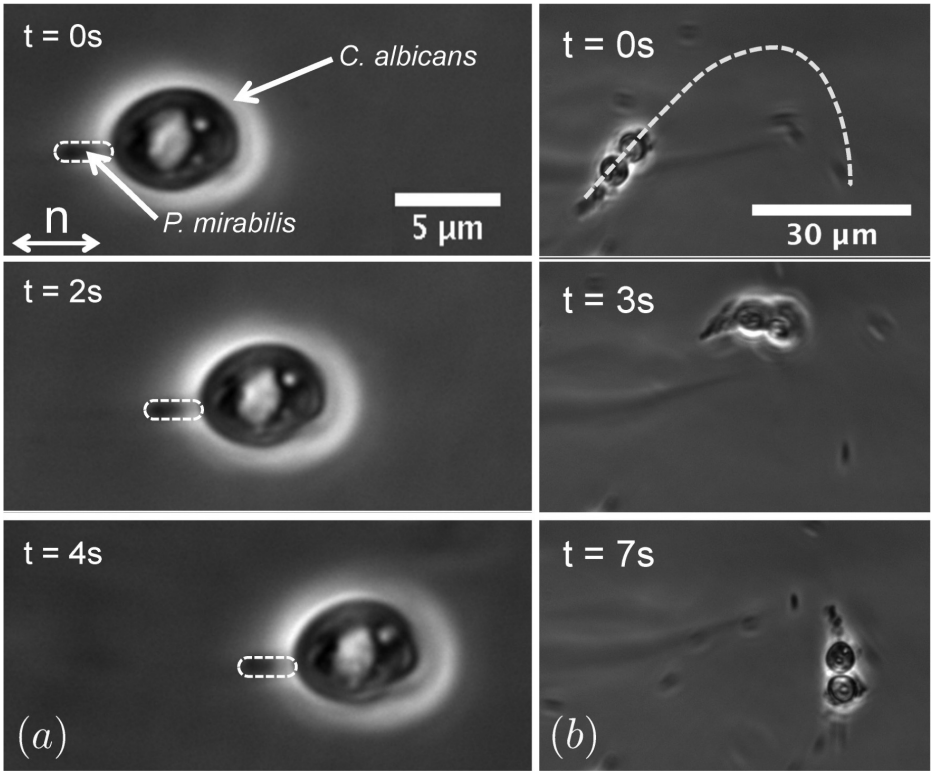


**Fig. 1**

**Fig. 2.** (Left) Timelapse of a single P. mirabilis cell pushing a 2mm-diameter polystyrene microparticle along the far-field nematic LC director (n) (see Movie S3). (Right) Percentage of cells reversing in isotropic and in nematic LC in the absence (-) or presence (+) of microparticles. N.D.: not determined.

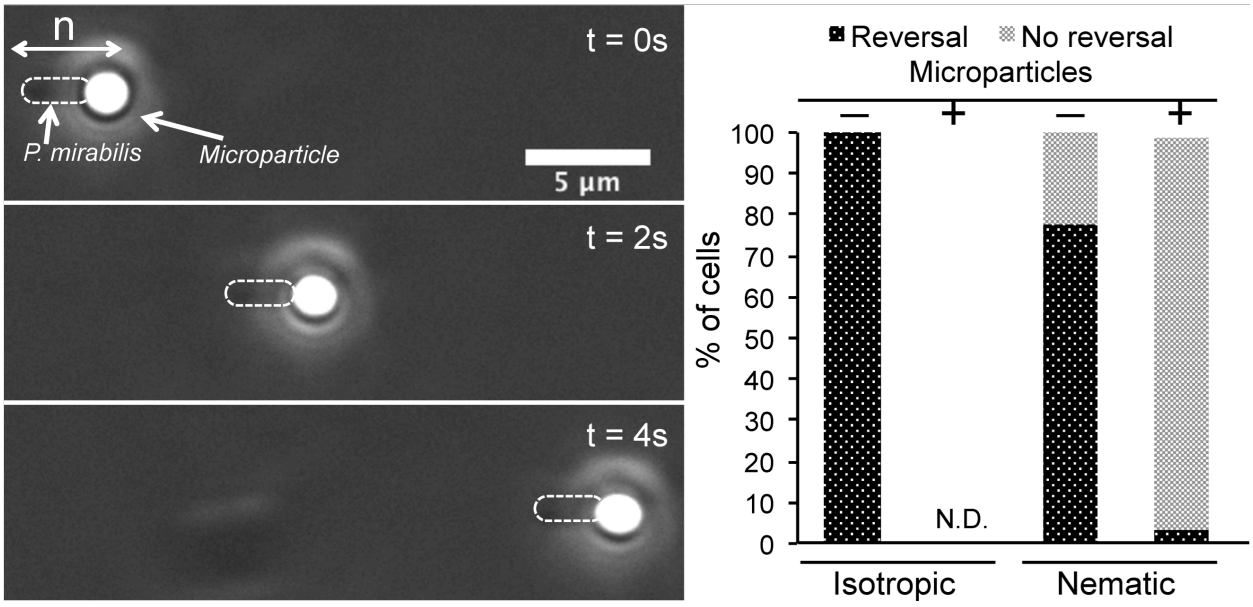


**Fig. 2**

**Fig. 3. (a)** Swimming speed for a range of cargo sizes, from experiments (circles - microbeads; triangle - *C. albicans* cell), numerical simulation (solid line), and analytical prediction (dashed line). **(b)** Model microorganism with spherical cargo.

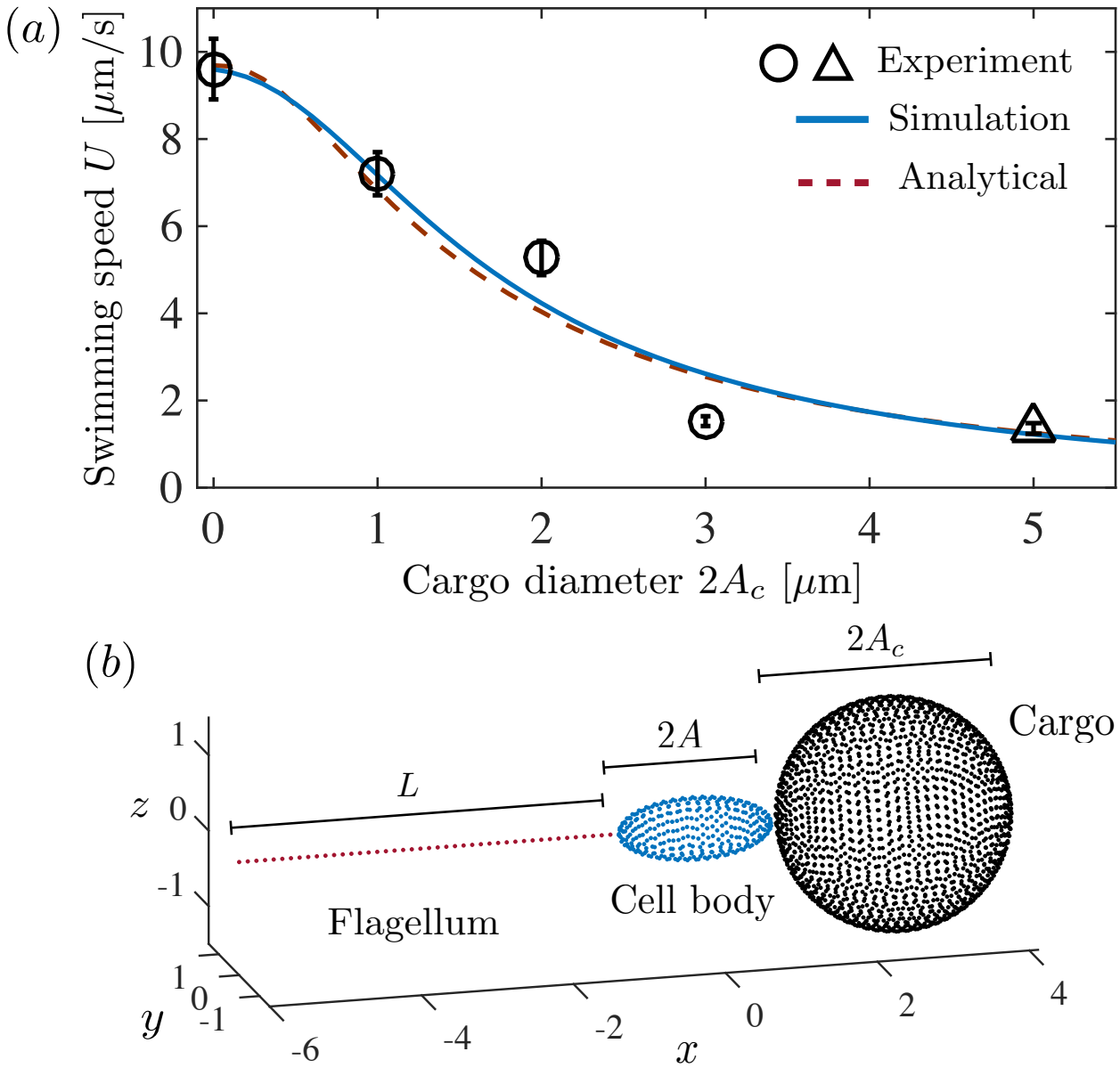


**Fig. 3**

**Fig. 4.** Computed speed of a cell-body and cargo driven by a nearby flagellum (solid line) and a very distant flagellum (dashed line), underscoring the importance of hydrodynamic interactions.

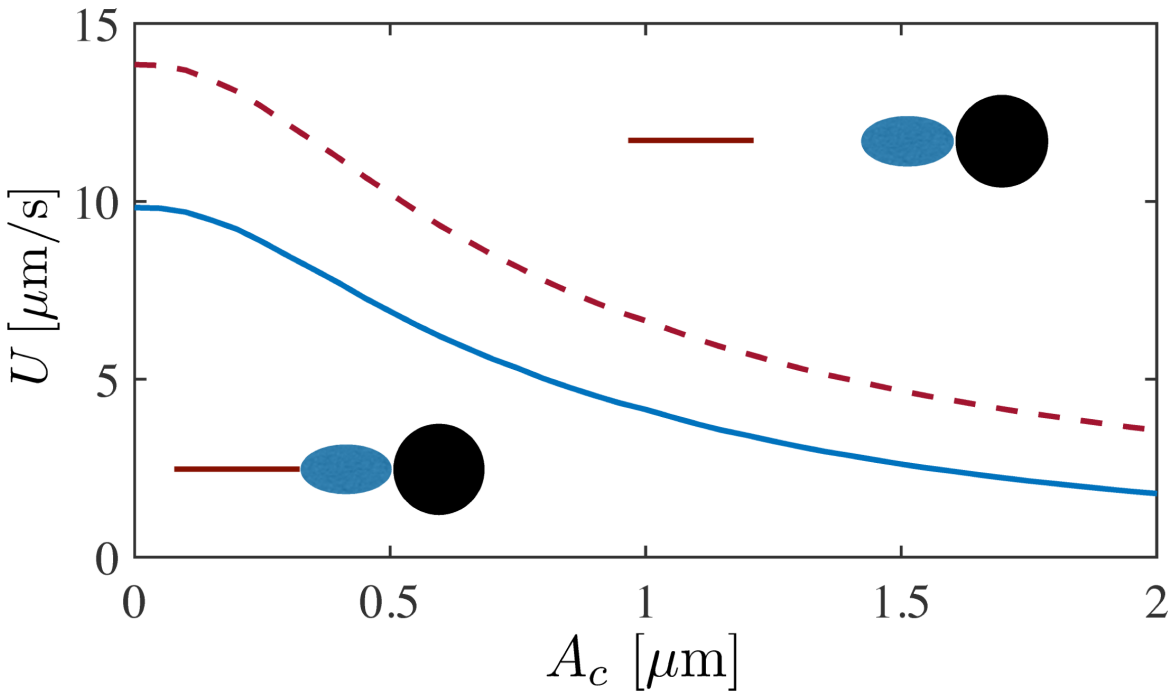


**Fig. 4**

**Fig. S1.** Schematic representation of the experimental chamber used to observe the motility of bacterial cells in LC solutions. The double-headed arrows indicate the direction of rubbing along the surface of the glass slides.

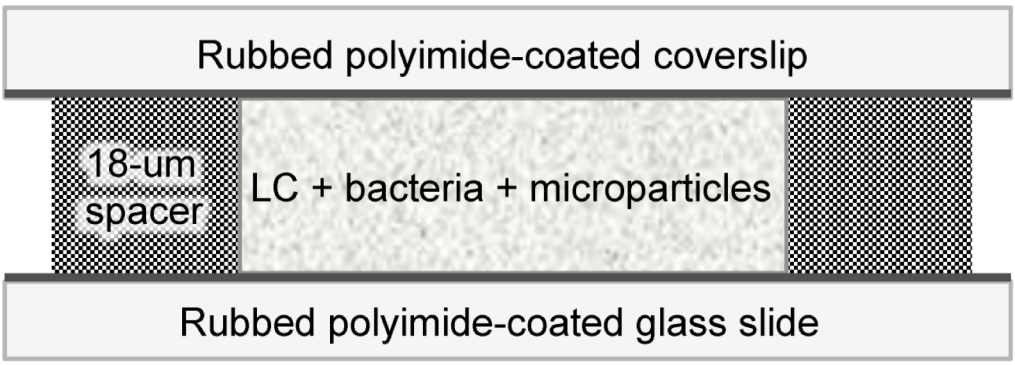


**Fig. S1**

**Fig. S2.** Phase contrast microscope image of a 1- m diameter polystyrene microparticle di using in nematic DSCG at 25°C. The blue line in the image indicates the superimposed trajectory of the drifting microbead recorded every 1 min over 30 min.

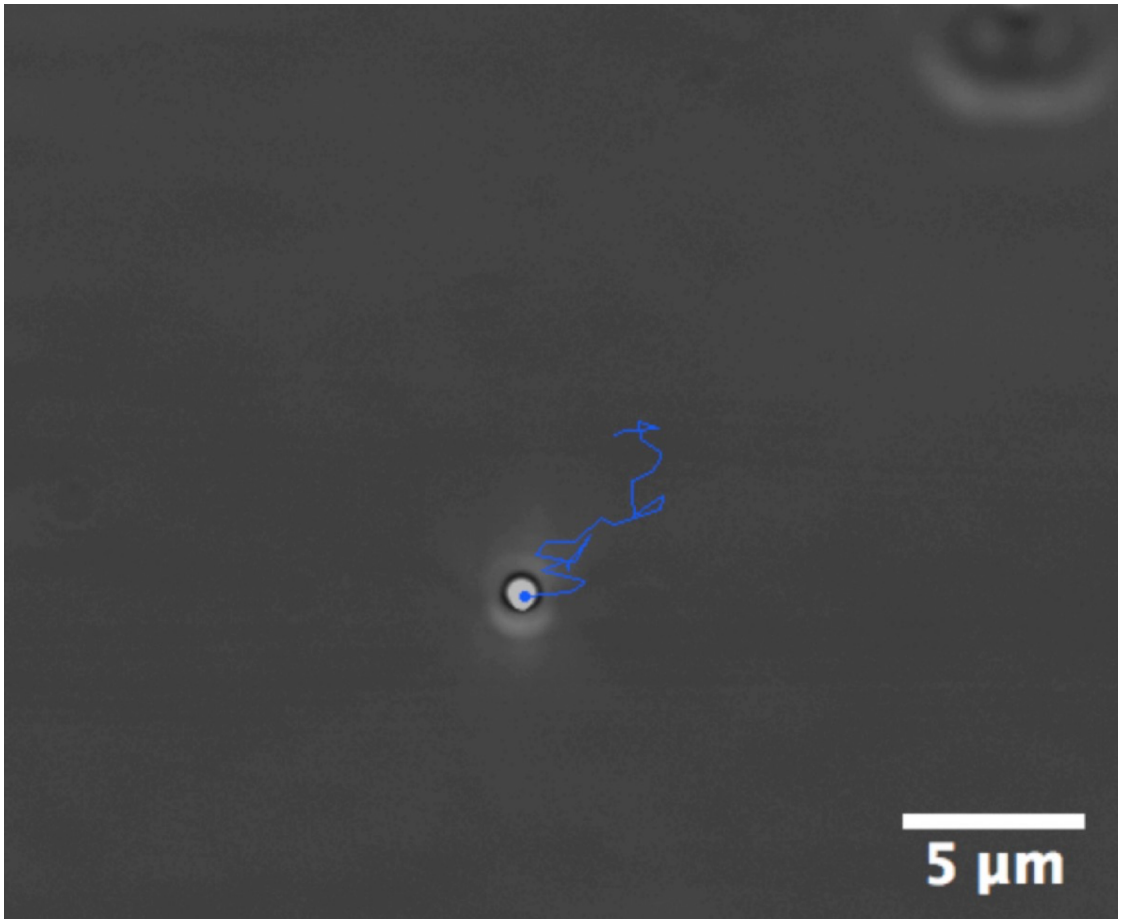


**Fig. S2**

**Fig. S3.** Polarized light micrographs of the experimental chamber aligned (a) parallel and (b) 45° to one of the crossed polarizers. We confirmed that the alignment of the nematic LC was parallel to the direction of rubbing by inserting a quarter wave plate into the optical path of a microscope and analyzing the appearance of the sample between crossed polars. (c) and (d) represent the local alignment of the LCs under crossed polars and bright field respectively. Dotted line represents the complex director profile by using bacteria as a tracer of local director.

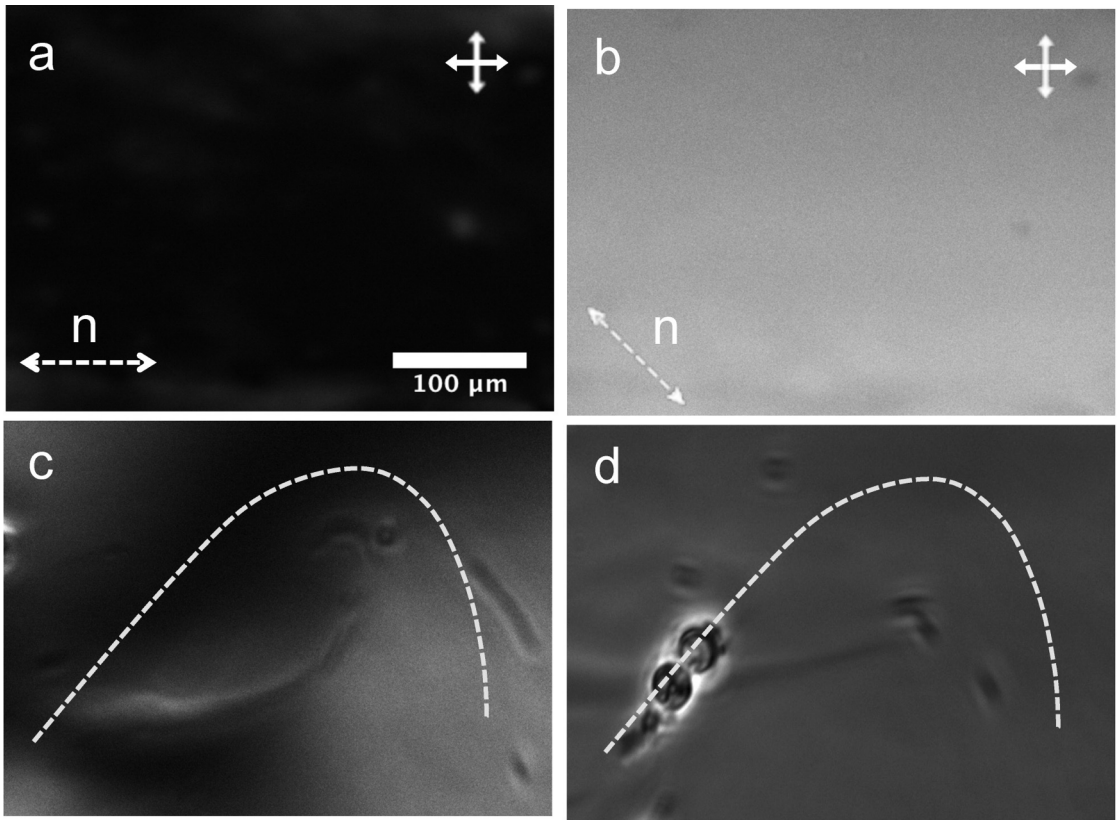


**Fig. S3**

**Fig. S4.** Five timeseries of *P. mirabilis* swimming speeds while pushing 2-µm diameter microparticles.

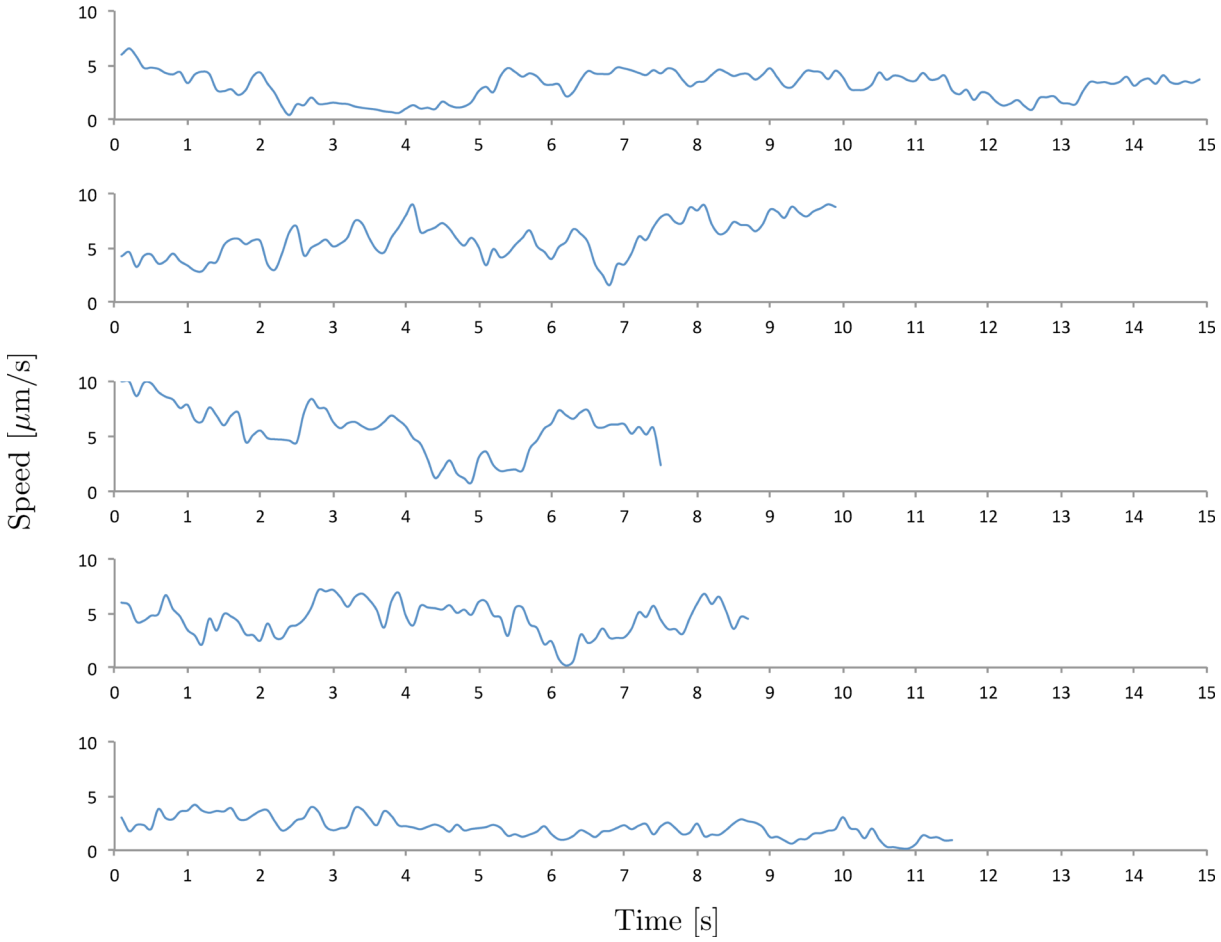


**Fig. S4**

**Fig. S5.** Two analytical estimate of the velocity of the load (assuming no hydrodynamic interactions between the cell body and the cargo) subject to a net force F, compared with the results of the full numerical simulations. Simulated values are shown as a solid line, the simplest estimate (10) is shown as a dashed line, and the improved estimate from (17) is shown as a dot-dashed line.

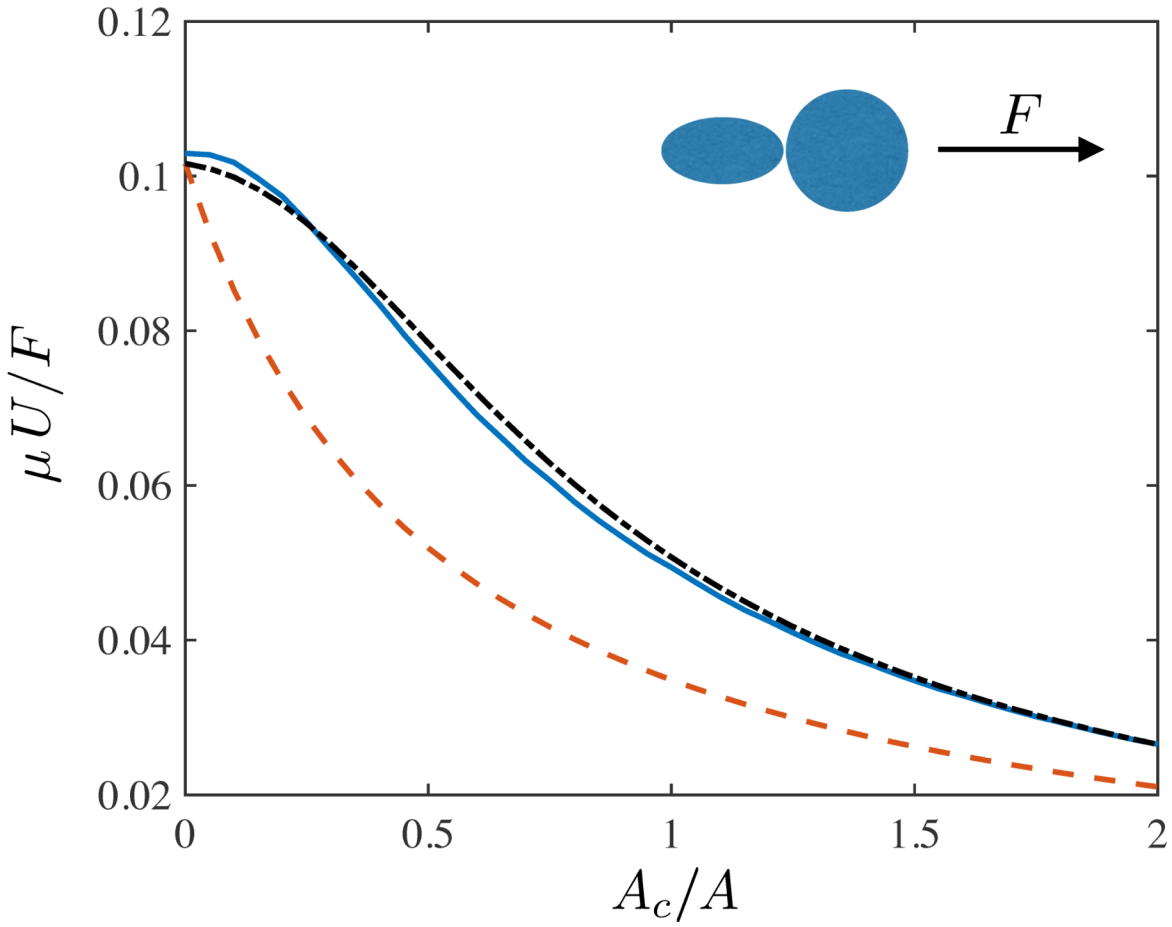


**Fig. S5**

**Movie Captions**

**Movie S1.** Bright field optical microscopy video showing P. mirabilis cells in 15 wt% DSCG at 25circC (nematic phase) carrying yeast cells along the far field LC director (n), aligned in the x-direction (horizontal direction of movie).

**Movie S2.** Bright field optical microscopy video depicting multiple P. mirabilis cells pushing a group of yeast cells (*Candida albicans*) along a curved path following the director profile.

**Movie S3.** Bright field optical microscopy video demonstrating that P. mirabilis cells pushing 2-m microparticle along the LC director (n).

**References**


1. J. G. Mitchell and G. M. Barbara, Aquatic Microbial Ecology, 1999, 18, 227–233.

2. N. Darnton, L. Turner, K. Breuer and H. C. Berg, Biophysical Journal, 2004, 86, 1863–1870.Y. Hiratsuka, M. Miyata, T. Tada and T. Q. P. Uyeda, Proceedings of the National Academy of Sciences of the United States of America, 2006, 103, 13618–13623.

3. B. Weibel, P. Garstecki, D. Ryan, W. R. DiLuzio, M. Mayer, J. E. Seto and G. M. Whitesides, Proceedings of the National Academy of Sciences of the United States of America, 2005, 102, 11963–11967.

4. O. S. Pak, W. Gao, J. Wang and E. Lauga, Soft Matter, 2011, 7, 8169–8181.W. Gao, D. Kagan, O. S. Pak, C. Clawson, S. Campuzano, E. Chuluun-Erdene, E. Shipton, E. E. Fullerton, L. Zhang, E. Lauga and J. Wang, Small, 2012, 8, 460–467.E. E. Keaveny, S. W. Walker and M. J. Shelley, Nano letters, 2013, 13, 531–537.

5. Sokolov, M. M. Apodaca, B. A. Grzybowski and I. S. Aranson, Proceedings of the National Academy of Sciences of the United States of America, 2010, 107, 969–974.R. Fernandes, M. Zuniga, F. R. Sassine, M. Karakoy and D. H. Gracias, Small, 2011, 7, 588–592.

6. Shklarsh, A. Finkelshtein, G. Ariel, O. Kalisman, C. Ingham and E. Ben-Jacob, Interface Focus, 2012, 2, 786–98.

7. H. C. Berg, Random Walks in Biology, Princeton University Press, 1993.

8. Sahari, M. A. Traore, B. E. Scharf and B. Behkam, Biomed Microdevices, 2014, 16, 717–25.

9. W. R. DiLuzio, L. Turner, M. Mayer, P. Garstecki, D. B. Weibel, H. C. Berg and G. M. Whitesides, Nature, 2005, 435, 1271–1274.S. E. Hulme, W. R. DiLuzio, S. S. Shevkoplyas, L. Turner, M. Mayer, H. C. Berg and G. M. Whitesides, Lab on a Chip, 2008, 8, 1888–1895.J. L. Connell, A. K. Wessel, M. R. Parsek, A. D. Ellington, M. Whiteley and J. B. Shear, MBio, 2010, 1, e00202–10.

10. P. C. Mushenheim, R. R. Trivedi, H. H. Tuson, D. B. Weibel and N. L. Abbott, Soft Matter, 2014, 10, 79–86.

11. S. Zhou, A. Sokolov, O. D. Lavrentovich and I. S. Aranson, Proceedings of the National Academy of Sciences of the United States of America, 2014, 111, 1265–1270.

12. Kumar, T. Galstian, S. Pattanayek and S. Rainville, Molecular Crystals and Liquid Crystals, 2013, 574, 33–39.

13. Sokolov, S. Zhou, O. D. Lavrentovich and I. S. Aranson, Phys. Rev. E, 2015, 91, 013009.

14. A. Warmink and J. D. van Elsas, Applied and Environmental Microbiology, 2009, 75, 2820–2830.C. J. Ingham, O. Kalisman, A. Finkelshtein and E. Ben-Jacob, Proc Natl Acad

Sci U S A, 2011, 108, 19731–6.J. A. Warmink, R. Nazir, B. Corten and J. D. van Elsas, Soil Biology & Biochemistry, 2011, 43, 760–765.M. Pion, J. E. Spangenberg, A. Simon, S. Bindschedler, C. Flury, A. Chatelain, R. Bshary, D. Job and P. Junier, Proc Biol Sci, 2013, 280, 20132242.R. Moscaritolo, M. Kinley, A. Raegen, M. Giuliani, R. White, C. Kelly, B. L.L. and D. J.R., Physics in Canada, 2013, 69, 137–139.A. Finkelshtein, D. Roth, E. Ben Jacob and C. J. Ingham, MBio, 2015, 6, e00074–15.

15. R. Orenstein and E. S. Wong, American Family Physician, 1999, 59, 1225–1234.L. E. Nicolle and A. C. G. Committee*, Can J Infect Dis Med Microbiol, 2005, 16, 349–60.

16. Viney, A. E. Huber and P. Verdugo, Macromolecules, 1993, 26, 852–5.L. S. M. A. Fritz, Clinical Gynecologic Endocrinology and Infertility, Lippincott Williams & Wilkins, 8th edn, 2011, p. 1.

17. F. C. Chretien, Acta Obstet Gynecol Scand, 2003, 82, 449–61.

18. N. H. Hartshorne and G. D. Woodard, Molecular Crystals and Liquid Crystals, 1981, 64, 153–154.H. Lee and M. M. Labes, Molecular Crystals and Liquid Crystals, 1983, 91, 53–58.

19. L. Cheng, Y. Y. Luk, C. J. Murphy, B. A. Israel and N. L. Abbott, Biomaterials, 2005, 26, 7173–7182.

20. H. L. T. Mobley and R. Belas, Trends Microbiol., 1995, 3, 280–284.

21. H. H. Tuson, M. F. Copeland, S. Carey, R. Sacotte and D. B. Weibel, Journal of Bacteriology, 2013, 195, 368–77.

22. Musevic, M. Skarabot, U. Tkalec, M. Ravnik and S. Zumer, Science, 2006, 313, 954–958.

23. E. Lauga and T. Powers, Rep. Prog. Phys., 2009, 72, 096601.

24. Pozrikidis, Boundary Integral and Singularity Methods for Linearized Viscous Flow, Cambridge University Press, Cambridge, UK, 1992.

25. S. E. Spagnolie and E. Lauga, J. Fluid. Mech., 2012, 700, 1–43.

26. Cortez, SIAM J. Sci. Comput., 2001, 23, 1204–1225.J. Ainley, S. Durkin, R. Embid, P. Boindala and R. Cortez, J. Comput. Phys., 2008, 227, 4600–4616.

27. A. P. Berke, L. Turner, H. C. Berg and E. Lauga, Phys. Rev. Lett., 2008, 101, 038102.R. Di Leonardo, D. Dell'Arciprete, L. Angelani and V. Iebba, Phys. Rev. Lett., 2011, 106, 038101.D. Lopez and E. Lauga, Phys. Fluids, 2014, 26, 071902.S. E. Spagnolie, G. R. Moreno-Flores, D. Bartolo and E. Lauga, Soft Matter, 2015, 11, 3396–3411.

28. M. S. Krieger, S. E. Spagnolie and T. R. Powers, Phys. Rev. E, 2014, 90, 052503.M. S. Krieger, M. A. Dias and T. R. Powers, arXiv preprint arXiv:1506.01696, 2015.M. S. Krieger, S. E. Spagnolie and T. R. Powers, arXiv preprint arxiv:1507.00776, 2015.

29. P. P. Lele, B. G. Hosu and H. C. Berg, Proc Natl Acad Sci U S A, 2013, 110, 11839–44.

S1. http://rsb.info.nih.gov/ij/plugins/track/track.html.

S2. C. Pozrikidis. Boundary Integral and Singularity Methods for Linearized Viscous Flow. Cambridge University Press, Cambridge, UK, 1992.

S3. R. Cortez. The method of regularized Stokeslets. SIAM J. Sci. Comput., 23:1204–1225, 2001.

S4. J. Ainley, S. Durkin, R. Embid, P. Boindala, and R. Cortez. The method of images for regularized Stokeslets. J. Comput. Phys., 227:4600–4616, 2008.

S5. D. Saintillan and M. J. Shelley. Orientational order and instabilities in suspensions of self-locomoting rods. Phys. Rev. Lett., 99:058102, 2007.

S6. S. Kim and S. J. Karrila. Microhydrodynamics: Principles and Selected Applications. Dover Publications, Inc., Mineola, NY, 1991.

# CHAPTER 6

## Conclusions and Significance

**Conclusions and Significance**

The bacterial cell envelope consists of lipid bilayers and cell wall, and plays a central role in the establishment and maintenance of cell size and shape. The cell wall is composed of a peptidoglycan macromolecule currently believed to be the most important element for mechanical properties of bacteria (1-3).

The cell wall is continuously remodeled during growth through the partial degradation of peptidoglycan by autolysins and the insertion and assembly of cell-wall precursors via glycosyltransferases (4). Transpeptidases form cross-linking peptide bonds between adjacent pentapeptides that decorate the polysaccharide backbone (3, 4). A growing body of evidence suggests that cytoskeletal proteins control the orientation of peptidoglycan growth in replicating bacteria, which regulates cell shape and dimensions. The identification of proteins that participate in peptidoglycan assembly, degradation, and remodeling is still underway and may shed light on other families and classes of proteins that are currently uncharacterized (5-7). Furthermore, the biochemical details underlying the mechanisms responsible for the spatial and temporal control of peptidoglycan insertion are still emerging and the relationship between this process and the mechanical properties of the cell wall are virtually unknown. In the first part of thesis we focused on finding novel cell stiffness regulators in *P. aeruginosa* by screening a genome-wide collection of transposon mutants from a non-redundant transposon library of *P. aeruginosa* PA14 strain.

*P. aeruginosa,* a ubiquitous Gram-negative bacterium, is an opportunistic human pathogen and causes persistent respiratory infections in cystic fibrosis patients (8). 73% of the genes in *P.*

*aeruginosa genome* have either hypothetical or unknown functions (9). In Chapter 2, we described GRABS (General Regulators Affecting Bacterial Stiffness), a high-throughput screening method that enabled us to characterize the mechanical contribution of all non-essential genes in *P. aeruginosa* (10). The GRABS assay is a microplate reader-based assay designed to monitor changes in growth of bacterial mutants embedded in 1% agarose and in liquid nutrient broth and to facilitate very large scale experiments of stiffness in thousands of different strains (6). By embedding bacteria in agarose, we are able to apply a sufficient amount of force to inhibit the growth of mutants with stiffness defects, while simultaneously monitoring their liquid growth to compensate for any growth based defect inherent to the genetic mutant. We identified 42 mutants that had a significantly lower stiffness (-20%) compared to wild type *P. aeruginosa* PA14. We found that genes involved in amino acid transport and metabolism pathway and coenzyme transport and metabolism pathway account for the highest number of mechanical modulators (6 mutants each). From these, we established and characterized the role of D-Ala dehydrogenase, DadA in cell stiffness using microfluidic-based flexural rigidity measurements. Our experiments with a *dadA*::Tn mutant also revealed the importance the D-Ala metabolism in maintaining cell mechanical properties as increase in D-Ala levels reduce cell stiffness.

This study will play a fundamental role in decoding bacterial cell biology and developing new and potent antibiotics against gram-negative pathogens, such as *P. aeruginosa.* The discovery of the molecular underpinnings of peptidoglycan biosynthesis will lead to the identification of biochemical factors that regulate cellular mechanical properties and will play a central role in understanding bacterial physiology by characterizing the relationships among peptidoglycan assembly, remodeling, and mechanics.

The second part of the thesis describes the motion of motile bacterial cells in anisotropic environments in which the physical properties are not identical in all directions and dependent upon the direction to which it is measured. In the first study, we investigated how the elasticity of anisotropic environment affects bacterial motility. Using nematic liquid crystals (LC) phase of disodium chromoglycate (DSCG) as a model anisotropic medium, we found that motile, hyper-flagellated *P. mirabilis* cells orient and move along the direction of LC alignment when dispersed in nematic uniformly aligned DSCG films (11). Moreover, the elasticity of the LC generates inter-bacterial forces that drive the formation of bacteria into linear multi-cellular assemblies. These assemblies form reversibly due to the interplay of forces generated by the flagella of bacteria and the elasticity of the LC, both of which are comparable in magnitude (tens of pN) for motile *P. mirabilis* cells.

The second study revealed the behavior of motile bacteria at interfaces where one LC phase exhibits anisotropic properties (i.e., nematic) and a second LC phase (of the same LC) is isotropic (12). Motile bacterial cells adsorb to the interfaces—formed at temperatures where nematic and isotropic DSCG phases coexist—and orient and move parallel to the local director due to the influence of the nematic elasticity. We observed that adsorption of cells to the nematic-isotropic interfaces was reversible, as individual bacteria generated sufficient propulsive forces to escape from nematic microdomains formed within isotropic phase. Interestingly, we did not find single bacteria escaping isotropic microdomains, instead, in these cases, assemblies of bacteria escaped through a cooperative, multicellular phenomenon also mediated by defects. In

this study, we also demonstrated that the combined effects of nematic elasticity and topological defects can be thermally tuned to dynamically corral and release bacteria from isotropic domains. In the third study, we demonstrate controlled transport and delivery of microscale objects and non-motile cells by motile bacteria suspended in nematic LC phases of DSCG, which may have applications for the bottom-up assembly of materials structures and the study of interspecies interactions in polymicrobial communities that occur in LC-like environments (e.g., biofilms) (13).

Together, our results present a new class of active and anisotropic soft matter formed by dispersing motile bacteria (here, *Proteus mirabilis*, however in principal other motile bacteria should be applicable, as long as they generate sufficient force) within a biocompatible nematic lyotropic chromonic LC phases. The fundamental insights developed in these studies suggest methods and approaches for the manipulation of bacteria in ways that are not possible in isotropic fluids.

**References**


1. Höltje, J.V., 1998. Growth of the stress-bearing and shape-maintaining murein sacculus of Escherichia coli. *Microbiology and Molecular Biology Reviews*, *62*(1), pp.181-203.

2. Gan, L., Chen, S. and Jensen, G.J., 2008. Molecular organization of Gram-negative peptidoglycan. *Proceedings of the National Academy of Sciences*, *105*(48), pp.18953-18957.

3. Vollmer, W. and Bertsche, U., 2008. Murein (peptidoglycan) structure, architecture and biosynthesis in Escherichia coli. *Biochimica et Biophysica Acta (BBA)-Biomembranes*, *1778*(9), pp.1714-1734.

4. Typas, A., Banzhaf, M., Gross, C.A. and Vollmer, W., 2012. From the regulation of peptidoglycan synthesis to bacterial growth and morphology. *Nature Reviews Microbiology*, *10*(2), pp.123-136.

5. Tuson, H.H., Auer, G.K., Renner, L.D., Hasebe, M., Tropini, C., Salick, M., Crone, W.C., Gopinathan, A., Huang, K.C. and Weibel, D.B., 2012. Measuring the stiffness of bacterial cells from growth rates in hydrogels of tunable elasticity. *Molecular microbiology*, *84*(5), pp.874-891.

6. Auer, G.K., Lee, T.K., Rajendram, M., Cesar, S., Miguel, A., Huang, K.C. and Weibel, D.B., 2016. Mechanical genomics identifies diverse modulators of bacterial cell stiffness. *Cell Systems*, *2*(6), pp.402-411.

7. Janmey, P.A. and McCulloch, C.A., 2007. Cell mechanics: integrating cell responses to mechanical stimuli. *Annu. Rev. Biomed. Eng.*, *9*, pp.1-34.

8. Wood, R.E., 1976. Pseudomonas: the compromised host. *Hospital practice*, *11*(8), p91-100.

9. Lee, D.G., Urbach, J.M., Wu, G., Liberati, N.T., Feinbaum, R.L., Miyata, S., Diggins, L.T., He, J., Saucier, M., Déziel, E. and Friedman, L., 2006. Genomic analysis reveals that Pseudomonas aeruginosa virulence is combinatorial. *Genome biology*, *7*(10), p.R90.

10. Liberati, N.T., Urbach, J.M., Miyata, S., Lee, D.G., Drenkard, E., Wu, G., Villanueva, J., Wei, T. and Ausubel, F.M., 2006. An ordered, nonredundant library of Pseudomonas aeruginosa strain PA14 transposon insertion mutants. *Proceedings of the National Academy of Sciences of the United States of America*, *103*(8), pp.2833-2838.

11. Mushenheim, P.C., Trivedi, R.R., Tuson, H.H., Weibel, D.B. and Abbott, N.L., 2014. Dynamic self-assembly of motile bacteria in liquid crystals. *Soft Matter*, *10*(1), pp.88-95.

12. Mushenheim, P.C., Trivedi, R.R., Weibel, D.B. and Abbott, N.L., 2014. Using liquid crystals to reveal how mechanical anisotropy changes interfacial behaviors of motile bacteria. *Biophysical journal*, *107*(1), pp.255-265.

13. Trivedi, R.R., Maeda, R., Abbott, N.L., Spagnolie, S.E. and Weibel, D.B., 2015. Bacterial transport of colloids in liquid crystalline environments. *Soft matter*, *11*(43), pp.8404-8408.

# APPENDIX 1

## Studying the role of Mic27 in maintaining inner mitochondrial membrane morphology

**Abstract**

Mitochondria are the central energy-producing organelles in eukaryotes. The morphology of mitochondria varies widely in different cell types and with changing environmental conditions. The morphology of the inner mitochondrial membrane (IMM) is also dramatically altered in the development of many human diseases, such as diabetes, obesity, cancer, and neurodegeneration. The mechanisms by which IMM morphology is maintained and the consequences of IMM morphology alterations are not well understood. I am particularly interested in how the localization of specific mitochondrial proteins and lipids are affected by changes in IMM ultrastructure. Recent studies in bacteria have proposed a complex interplay between membrane curvature and biomolecule distribution; however, this phenomenon remains unexplored in the context of mitochondria.

To understand the relationship between IMM morphology and biomolecule localization, I studied the localization of Mic27, a putative IMM transmembrane protein which resides in highly-curved regions of the IMM. Mic27 is a subunit of mitochondrial contact site and cristae organizing system (MICOS), a complex that is responsible for maintenance of IMM ultrastructure. Localization of MICOS at highly curved regions of the IMM seems to be critical for its function, however the underlying molecular mechanisms are unknown. Mic27 has been reported to interact specifically with the anionic phospholipid cardiolipin (CL). CL is a signature lipid of IMMs and constitutes about 20% of the total lipid composition. *I hypothesize that the interaction of Mic27 and CL is critical for maintaining IMM morphology in healthy mitochondria.*

This project contributes to our understanding of how protein-lipid interactions play a role in localizing proteins that are important in the maintenance of the mitochondrial membrane.

**Introduction**

Mitochondrial organization and dynamics, as well as their interactions with other intracellular organelles, are crucial for energy production, redox homeostasis, and apoptosis in eukaryotic cells[1]. Mitochondria are descended from α-proteobacteria and have a distinct structure arising from the shape and organization of the outer and inner mitochondrial membrane (IMM) [1-3]. The IMM is extensively folded and separates the mitochondrial matrix from the intermembrane space[1]. The numerous invaginations of the IMM are called cristae and are connected to the peripheral inner membrane through crista junctions (CJs)[1]. The peripheral IMM also forms *contact sites* where the IMM and OMM are in close physical proximity. Contact sites promote transport of metabolites, pre-proteins, and lipids between the mitochondrial matrix and the cytosol. Thus, contact sites are uniquely positioned to communicate structural information between the IMM and OMM[1, 4].

Healthy respiring mitochondria exhibit a tubular and networked morphology with well-formed cristae, CJs, and contact sites in the IMM[1, 4]. In many human pathologies (e.g., diabetes, obesity, cardiovascular diseases, cancer, and neurodegeneration), mitochondria display spherical and fragmented morphologies[5-14]. The morphology of the IMM changes dramatically with the development of these diseases (Fig 1) [9, 11-14]. However, the molecular mechanisms that are responsible for regulating IMM ultrastructure are poorly understood.

There is evidence that suggests that localization of proteins within the mitochondrion affects mitochondrial membrane architecture[4-8]. A number of recent studies have identified a large protein complex, MICOS, that localizes to the highly-curved regions of the IMM[5-8]. The

localization of the MICOS complex is key to its function in maintaining CJs, IMM architecture, and forming contact sites between the IMM and OMM. Alteration of MICOS complex expression and/or localization lead to a variety of human disease conditions[4] (Table 1). However, the processes responsible for positioning MICOS at CJs are not known[4].

Recently, a subunit of the human MICOS complex called Mic27 (formerly called APOOL) was found to interact specifically with the anionic phospholipid cardiolipin (CL) [4-8, 19]. CL is the third most abundant lipid in mitochondria and constitutes about 20% of the total lipid composition (Table 2). CL plays important roles in bioenergetics, membrane integrity, and apoptosis [20-24]. The unique physiochemical properties of CL cause it to form microdomains in regions of large negative membrane curvature in order to release the surface energy potential associated with mechanical strain (Fig 1) [25-27]. In bacteria, these CL microdomains have been suggested to provide guiding cues for localization of certain proteins at highly curved regions of the membrane (e.g., poles and division septa), but any potential role for CL microdomains in mitochondrial protein localization remains unknown[25-28]. In mitochondria, the highly curved regions of IMM located at CJs are enriched in CL. Localization of the MICOS complex at CJs and the CL-specific interaction of the subunit protein Mic27 provides an opportunity to test whether CL microdomains can recruit proteins at highly curved region in mitochondria. I used Mic27 as a candidate protein to determine how alterations in one of the MICOS subunits affects the overall morphology of mitochondria. CL microdomains may provide nucleation sites for the assembly of the MICOS complex by positioning Mic27 at the CJs and recruiting other MICOS subunits to maintain IMM ultrastructure.

## Material and Methods

### 2.2.1. Cell culture and transfection

HeLa cells were cultured in Dulbecco's modified eagle medium (DMEM) supplemented with 10% fetal bovine serum and antibiotic–antimycotic mix in a 5% $CO_2$ humidified incubator at 37ºC. Following the manufacturer's instructions, X-tremeGene HP DNA Transfection Reagent (Sigma-Aldrich) was used to transfect cells with *FLAG-mic27* cDNA at 65–70% confluency on 35 mm coverslips. Briefly, transfection was done by mixing 2µg of the DNA with 3µL transfection reagent in 200 µL OptiMEM and cells were incubated for 16-24 hr post transfection.

### Immunostaining and confocal microscopy

Transfected cells were fixed with 3% paraformadehyde (PFA) for 10 min at room temperature. Cells were washed with 1X phosphate-buffered saline (PBS) (10 mM $Na_2HPO_4$, 1.8 mM $KH_2PO_4$, 137 mM NaCl, 2.7 mM KCl, pH 7.4) three times for 5 min each to remove PFA. Cells were permeabilized with 0.2% Triton X-100 for 15 min and blocked with 10% normal goat serum (NGS) for 90 min. Next, cells were incubated in saturating concentration of primary antibody solution followed by multiple washes with PBS. To visualize stained proteins, cells were incubated in secondary antibody solution conjugated with Alexa Fluor fluorophores and imaged with confocal laser scanning microscopy (CLSM). Five different primary antibodies were used in this study: rabbit polyclonal ✔-APOOL antibody (Sigma-Aldrich), rabbit polyclonal ✔-Tom20 (FL-145) (Santa Cruz Biotechnology), mouse monoclonal ✔-Tom20 (Abcam), mouse monoclonal ✔-FLAG M2 (Sigma-Aldrich), and ✔-VDAC1 / porin (20B12AF2) (Abcam). Secondary antibodies (Alexa Fluor 568, Alexa Fluor 488, and Alexa Fluor 647) were purchased from Invitrogen.

**Preparation of liposomes.**

We used lipids from Avanti Polar Lipids (Alabaster, AL): DOPC; herein referred to as PC, and cardiolipin (CL). To create liposomes, we dried aliquots of the mixtures of the lipids dissolved in chloroform in a glass vial under argon, and removed traces of solvent by incubating in a vacuum chamber for 12‑15 h at 25 °C. We resuspended the dried lipid fractions in R buffer (20 mM Tris-HCl, 0.1 mM EDTA, pH 7.4) and sonicated the suspensions for 20 min in a Branson 2510 bath sonicator. We immersed the vials containing the lipids in liquid nitrogen for ~2 min and sonicated for 20 min. We repeated freezing followed by sonication cycle 3 times. To prepare liposomes of the lipid mixtures, we extruded sonicated suspensions of lipids using a mini extruder (Avanti Polar Lipids) through a membrane containing 0.1μm pores. We used the following compositions of liposomes in this study: 100% PC, and 80:20% PC:CL. All ratios reflect weight percentages unless otherwise mentioned.

**Co-flotation assays of Mic27 and liposomes**

We incubated purified Mic27 (17.3 μM) for 5 min at 37 °C with liposomes containing one of three different PL compositions: buffer, 0.5 mM PC (100% PC); 0.42 mM PC and 55.1 μM CL (80:20% PC:CL). We mixed reactions with an 80% solution of Accudenz (Accurate Chemical and Scientific Corporation) in 125 mM HEPES, 500 mM KCl, and 50% glycerol. We pipetted the resulting mixture (40% Accudenz) into a 500 μL Beckman Coulter polycarbonate ultracentrifuge tube. We created a density gradient by successively layering 35%, 30%, and 0% Accudenz solutions and centrifuged the tubes at 281,227 x g at 4 °C for 2 h using a Beckman Coulter Optima Max-XP tabletop ultracentrifuge with a TLA 120.1 rotor. After centrifugation, we harvested 20 μL of liquid from the top layer, performed electrophoresis of equal volumes of the harvested material on a denaturing polyacrylamide gel (SDS-PAGE), and stained the gel

using the SilverQuest Silver Staining Kit (Life Technologies). We imaged gels using a FOTODYNE Gel Documentation system and quantified the intensity of the bands in ImageJ (version 1.43u).

**Mitochondrial surface rendering**

Specifically, I subtracted the background of immune-stained mitochondria and applied Gaussian smoothing parameters to smoothen the fluorescence signal. After setting up thresholding parameters on absolute fluorescence intensity, Surfaces were rendered on the mitochondria using rendering tool provided by image analysis software Imaris and surface area (A) and volume (V) information were extracted. S and V were used to calculate mito-sphericity ($\psi$), a parameter that is a measure of how closely the shape of a mitochondria approaches that of a mathematically perfect sphere.

$$\psi = \frac{\pi^{\frac{1}{3}} (6V_P)^{2/3}}{A_P}$$

$\Psi$ = Mito-sphericity
$V_p$ = Volume of the particle
$A_p$ = Surface area of the particle

## Results and Discussion

### Purified Mic27 has higher affinity to cardiolipin-containing liposomes

Mic27 is 27-kDa protein subunit of the MICOS complex. Using a lipid strip assay, a qualitative experimental method, it has been suggested to interact specifically with CL[19]. In collaboration with the UW-Madison Center for Eukaryotic Structural Genomics, I successfully purified recombinant Mic27 using a wheat germ-based cell free translation system. To confirm and quantify the Mic27-CL interaction, I performed a co-floatation experiment in which I measured the binding of Mic27 to liposomes containing different phospholipid ratios.

Purified Mic27 was incubated with liposomes containing 100% phosphatidylcholine (PC) and no CL or 80% PC and 20% CL. These Mic27-liposome mixtures were then loaded onto a sucrose density gradient and centrifuged to separate Mic27 bound to liposomes from unbound Mic27. The Mic27 fraction that associated with liposomes was isolated and quantified using SDS-PAGE followed by densitometry measurement. This analysis revealed that the amount of Mic27 bound to CL-containing liposomes was 2-fold higher than pure PC liposomes (Fig 2).

### Mic27 localizes to mitochondria and over-expression of Mic27 leads to altered mitochondria morphology

We tested the localization of endogenous Mic27 in vivo using HeLa cells as a model cell line. We performed live cell antibody staining using a Mic27 specific antibody and visualized Mic27 via CLSM with an Alexa-647 conjugated secondary antibody. We also stained the cells with mitochondrial marker Tom20 and found that Mic27 co-localizes with Tom20, confirming mitochondria-specific localization of Mic27 (Fig 3).

To understand if Mic27 plays a key role in maintaining mitochondrial shape, I compared mito-morphology in cells with endogenous Mic27, cells overexpressing Mic27, and Mic27 knockdown cells. For the over-expression studies, I constructed a FLAG-tagged translational fusion of wildtype Mic27 and confirmed Mic27 over-expression using Western blot analysis. I expressed wildtype and Mic27 mutants followed by immunofluorescence with ✔-FLAG antibody in HeLa cells to confirm the mitochondrial localization of wildtype Mic27 (Fig 4). Confocal microscopy data reveals that mito-morphology is significantly altered in cells over-expressing Mic27 and mitochondria have become more spherical compared to the normal tubular morphology (Fig 4A, 4B). Current methods for quantifying mito-morphology are subjective, less quantitative, and insensitive at a single organelle level[19, 31, 32]. I developed an analysis method based on 3D surface rendering of confocal image stacks. Comparing mitochondrial sphericity, surface area, and volume enabled me to quantify mito-morphology at the level of single mitochondria (Fig 4D). Our analysis revealed that Mic27 over-expression leads to fragmentation of mitochondria. Transmission electron microscopy images also confirmed that upon Mic27 over-expression, IMM is disorganized and CJs disappear (Fig 4F) compared to control cells expressing endogenous Mic27 (Fig 4E).

To study if lower levels of Mic27 expression affects mito-morphology, I treated HeLa cells with Mic27 specific siRNA. I quantified the knockdown efficiency using Western blotting and observed a 70% decrease in the endogenous Mic27 level (Fig. 5C). Our 3D surface rendering based quantitative analysis method revealed that mito-mprphology remains unaltered upon Mic27 knockdown in HeLa cells (Fig 5D). Together, these results demonstrate that Mic27 over-

expression severely affects mito-morpholgoy, supporting my hypothesis that Mic27 plays an important role in maintaining mitochondrial morphology.

**Over-expressed Mic27 diffuses into IMM and alters mito-morphology**

Mic27 plays an important role in maintaining CJs and contact sites as a part of the MICOS complex. CJs are uniformly spaced regions of IMM where the cristae membrane is connected to peripheral IMM. I hypothesized that Mic27 localization would be punctate as it is localized at the CJ. I used super-resolution microscopy (Stochastic Optical Reconstruction Microscopy, STORM[33]) to study Mic27 localization in the IMM. By expressing FLAG-tagged Mic27 in HeLa cells and immunostaining with a photoswitchable fluorescent probe attached to the secondary antibody, I achieved ~30 nm resolution with STORM. STORM images reveal punctate localization of Mic27 in mitochondria, suggesting Mic27 localizes to the cristae regions (Fig. 6). In contrast, mitochondria from HeLa cells over-expressing Mic27 show a uniform distribution of Mic27, suggesting that IMM topology changes upon fragmentation. These results suggest that over-expressed Mic27 diffuses in the IMM and leads to changes in the overall shape of mitochondria. It will be very interesting to further explore if Mic27 is important for the localization of other sub-units of the MICOS complex, e.g. Mic60. Specifically, labeling Mic27 and Mic60 with a pair of photoswitchable fluorophores (Alexa Fluor 647 and Alexa Fluor 568) to perform co-localization experiments using STORM microscopy will inform us if Mic27 localization acts as a nucleation site for the assembly of the MICOS complex at the regions of CJs.

**Conclusion**

This study will be the first to correlate protein-lipid interaction with maintenance of mitochondrial ultrastructure. Novel insights developed in this project will be transformative in several ways: 1) they will contribute to our understanding of the localization of proteins at the highly-curved regions of IMM; 2) they will provide evidence that protein-lipid interactions play important roles in maintaining mitochondrial membrane morphology; and 3) they will guide future studies aimed at understanding molecular mechanisms leading to alterations in mitochondrial shape that are dependent on Mic27 expression. Altogether, this study may define the molecular mechanisms responsible for localization of proteins at highly curved regions of membrane, and further elucidates the role of protein-lipid interactions in regulating mitochondrial ultrastructure in normal and diseased-states.

**Fig. 1.** The IMM is highly curved in healthy mitochondria (A). Mitochondria fragmentation has been observed in numerous diseases, which in turn alters IMM morphology (B). In this cartoon, CL is depicted in red. Red boxes in (A) and (B) are shown at higher magnification in (C) & (D) respectively, to highlight the hypothesis of the Mic27—CL interaction is maintaining IMM morphology.

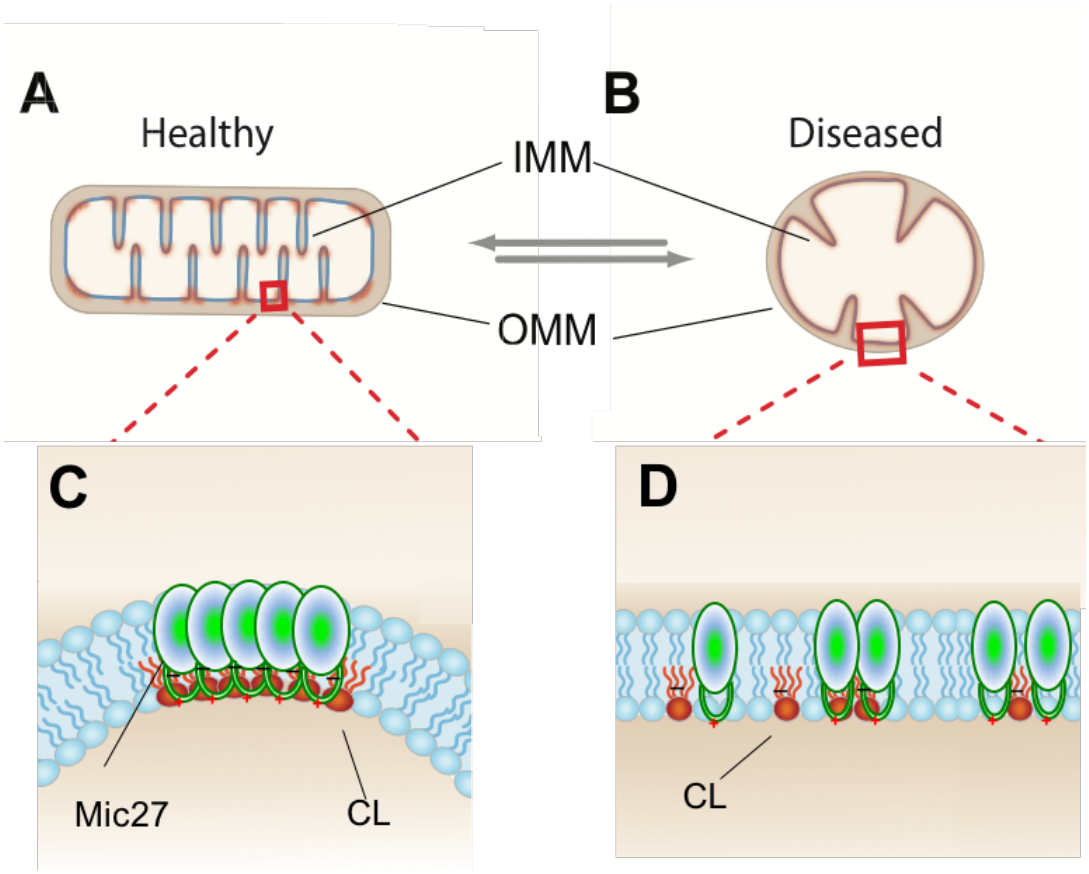


**Fig. 1**

**Fig. 2.** Silver-stained denatured PAGE gel representing that Mic27 has increased affinity to liposomes with CL. The 'no lipid' control shows that Mic27 does not float by itself in the co-floatation experiment.

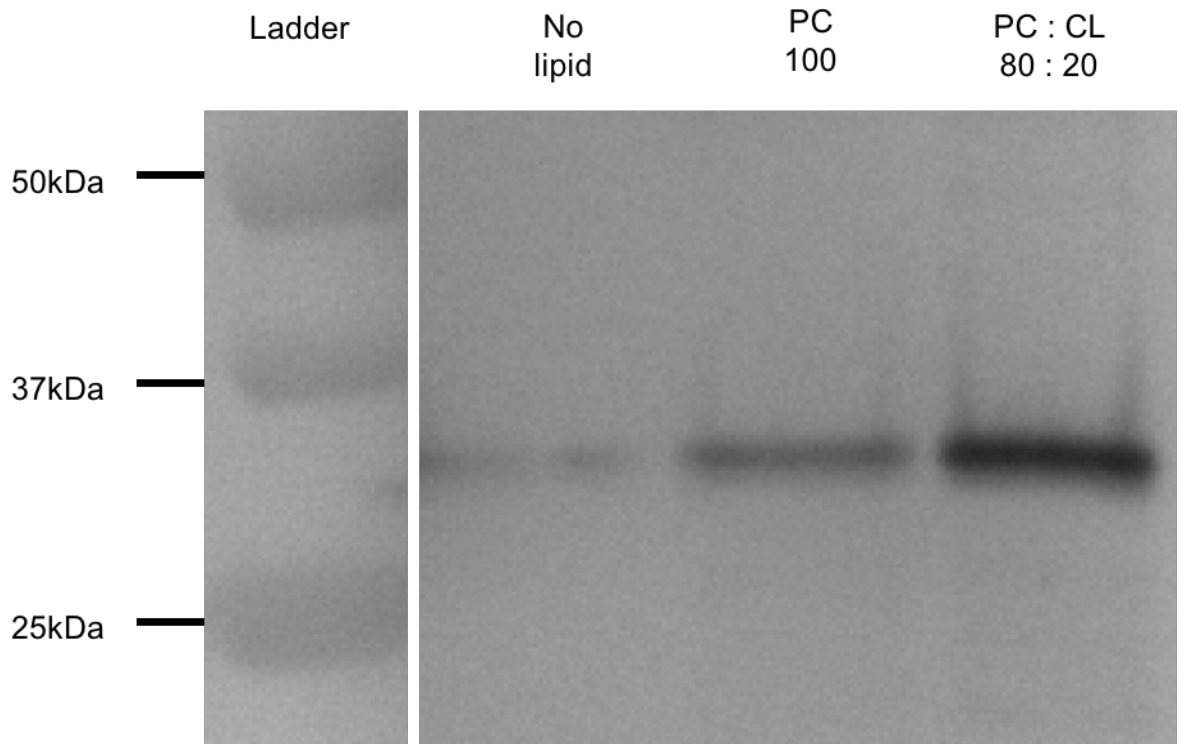


**Fig. 2**

**Fig. 3.** Representative confocal microscopy images of mitochondrial localization of Mic27. **(A)** Outer mitochondrial membrane protein Tom20 was used to visualize mitochondria and was stained with mouse anti-Tom20 primary antibody followed by Alexa-568 goat anti-mouse secondary antibody in **(A).** Mic27 was stained with rabbit anti-Mic27 antibody and Alexa-647 was used as secondary antibody in **(B). (C)** shows the co-localization of Tom20 (in red) and Mic27 (in green) fluorescence signal giving yellow color. It is very interesting to observe green encircled by red in some of the mitochondria in **(C)**, suggesting that Mic27 is indeed present inside the outer membrane.

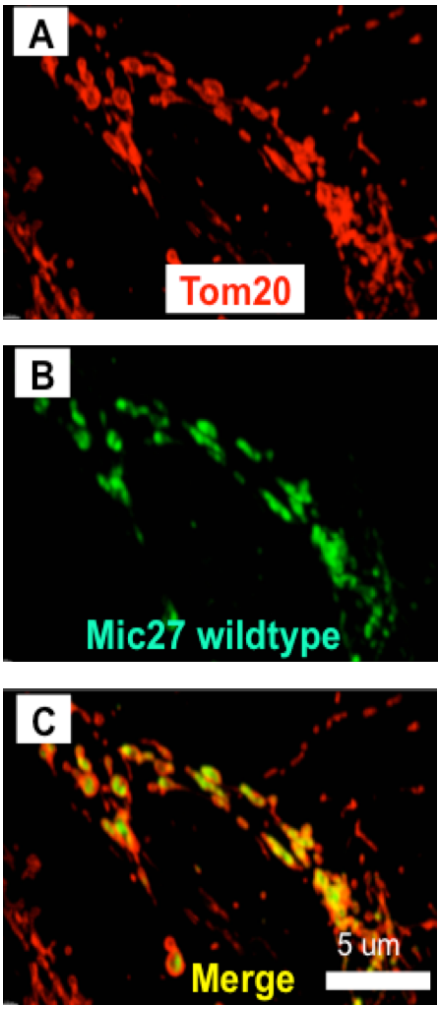


**Fig. 3**

**Fig. 4. (A)** Representative confocal microscopy images of mitochondria in HeLa cells with endogenous Mic27 expression **(A)** and Mic27 over-expressing HeLa cells **(B)**. **(C)** Western blot confirms that HeLa cells are over-expressing Mic27 after 16 h of transfection. VDAC was used as loading control. To quantitate the changes in the mitochondria morphology, I have calculated the sphericity of each individual mitochondrion in from 100 cells. If the mitochondria are spherical, they will get the value one, while really long tubular mitochondria will get values close to zero. **(D)** Histogram shows that Mic27 over-expression cells have mitochondria that are primarily spherical while wildtype mitochondria distribution is significantly different, suggesting that Mic27 over-expression alters mito-morphology significantly. **(E)** & **(F)** are representative TEM images of mitochondria showing IMM morphology in control HeLa cells **(A)**, and Mic27 over-expressing cells **(B)**. In **(E)** IMM is very well organized while CJs disappears in **(F)**.

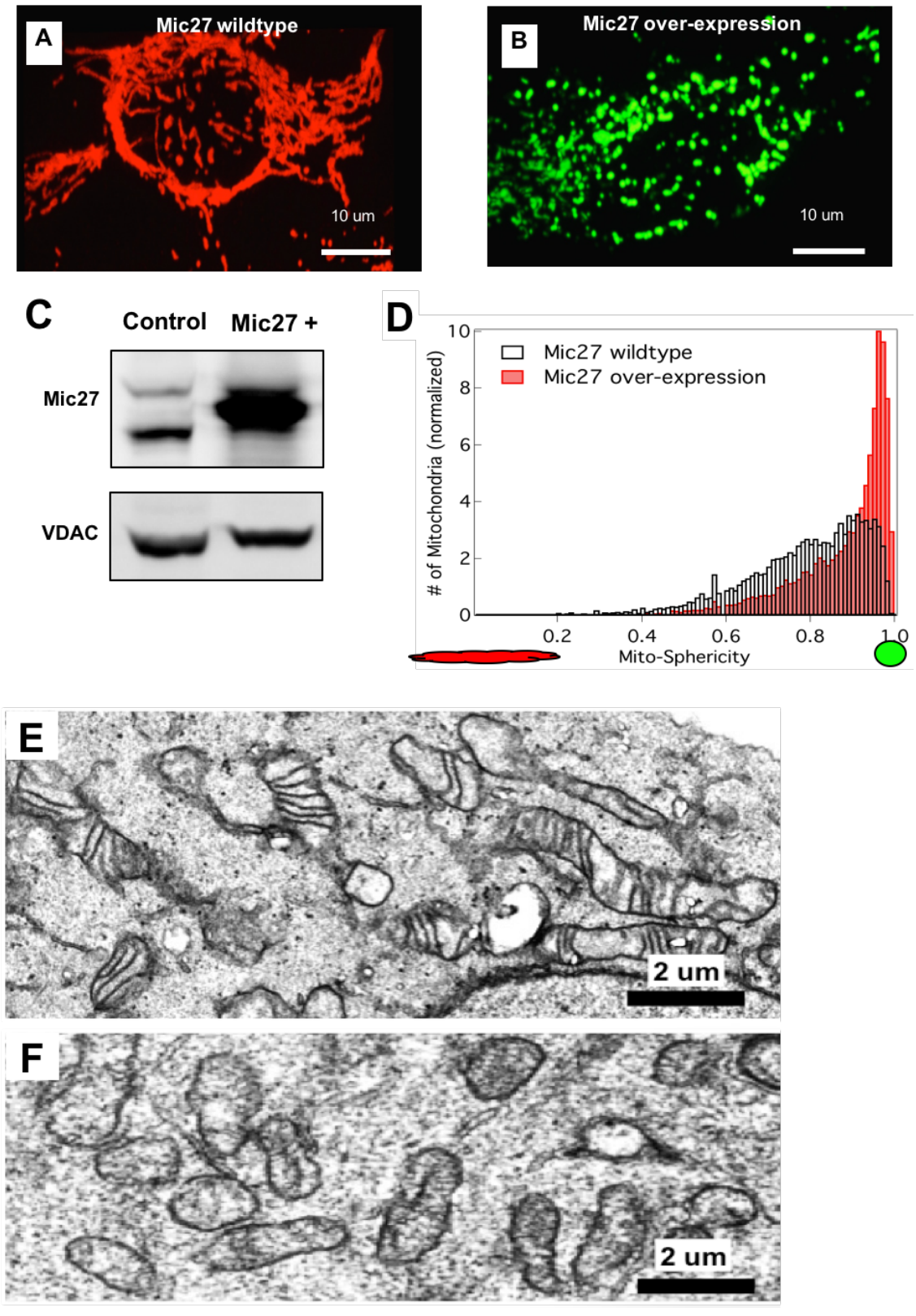
A
Mic27 wildtype
10 um
B
Mic27 over-expression
10 um
C
Control
Mic27 +
Mic27
VDAC
D
Mic27 wildtype
Mic27 over-expression
# of Mitochondria (normalized)
Mito-Sphericity
0
2
4
6
8
10
0.2
0.4
0.6
0.8
1.0
E
2 um
F
2 um

**Fig. 4**

**Fig. 5.** Representative confocal microscopy images of mitochondria in HeLa cells with control siRNA (A) and SMARTpool siRNA downregulating Mic27 expression levels in HeLa cells (B). (C) HeLa cells were treated with SMARTpool siRNA for 72 h and cell homogenate was run on the denaturing gel to detect the knockdown efficiency. Quantitation of the blot confirmed 65% knockdown of endogenous Mic27. VDAC was used as loading control. (D) Histogram quantitating mito-morphology for control and Mic27 knockdown cells. Mic27 downregulation does not affect the mito-morphology significantly.

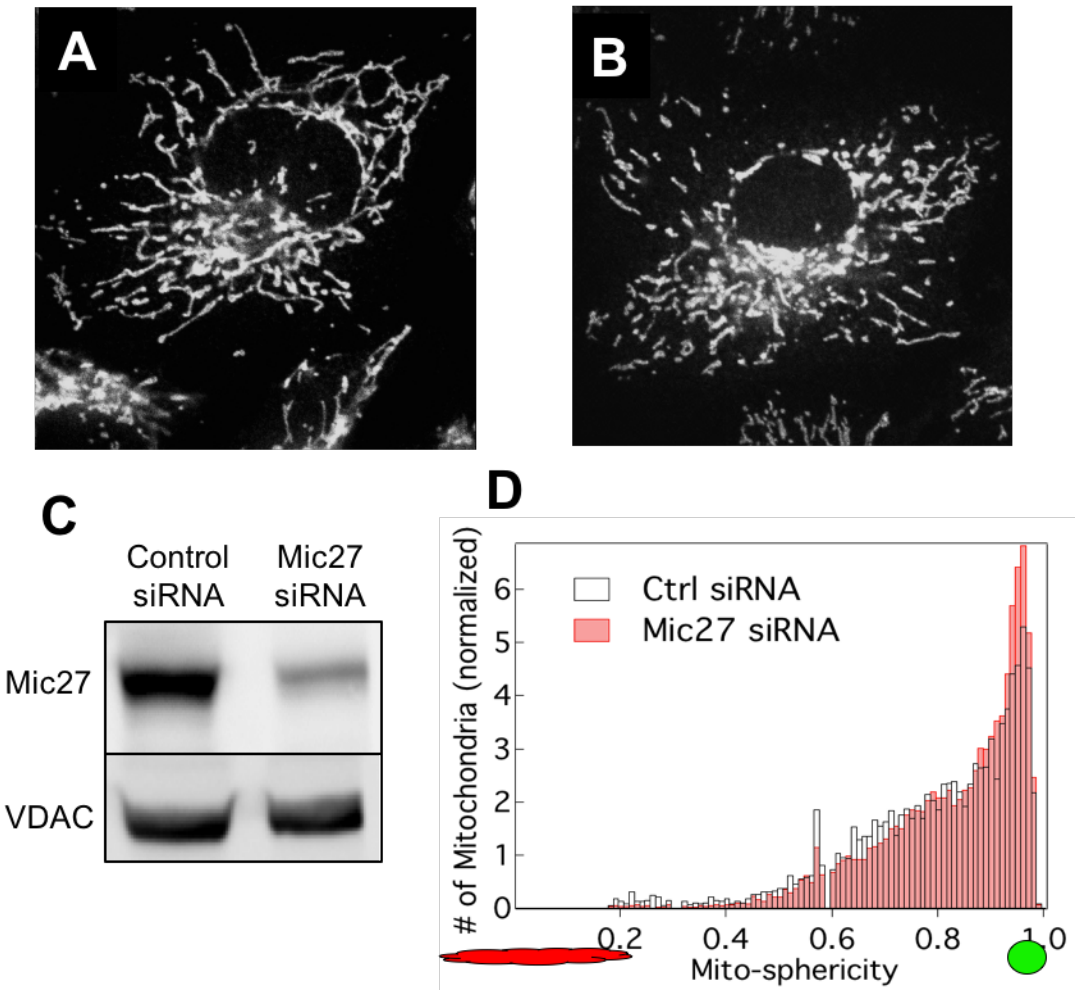


**Fig. 5**

**Fig. 6. (A)** & **(B)** are representative confocal microscopy images of mitochondria morphology in wildtype HeLa cells and Mic27 over-expressing cells respectively. **(C)** is a representative STORM images of Alexa 647 labeled Mic27 in control HeLa cells suggesting punctate localization in the IMM. Upon Mic27 over-expression **(D)**, the IMM morphology changes that results in the diffused localization pattern.

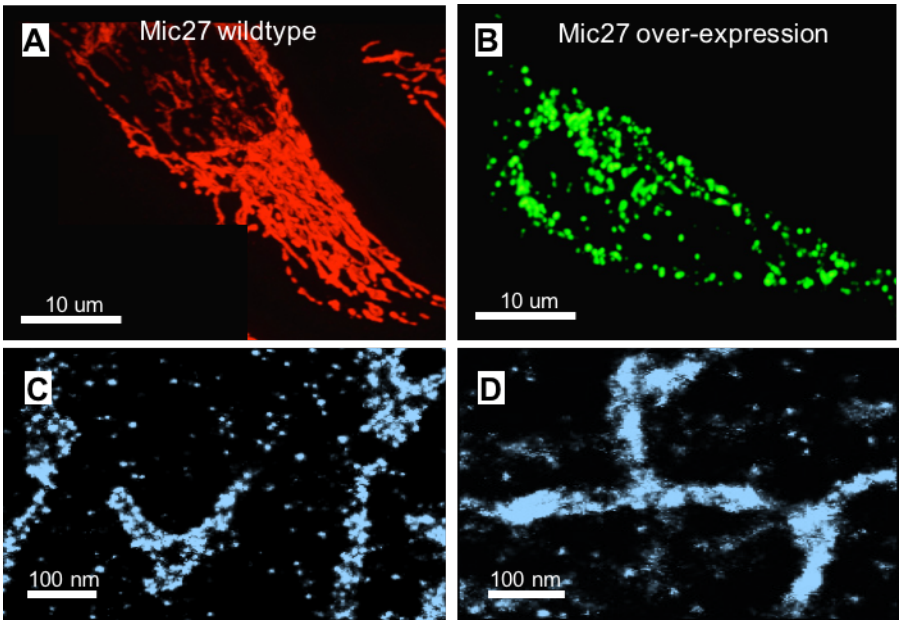


**Fig. 6**

**Table 1**

| Human diseases | MICOS alterations | Model systems | References |
|---|---|---|---|
| Epilepsy | Amino acid substitution in Mic60 | Animal model systems | Omori et al., 2002 |
| Down syndrome | Mic60 levels decreased | Human patient (fetal brain) | Bernert et al., 2002; Myung et al., 2003 |
| Parkinson's disease | Mic60 levels decreased | Cellular model systems | Van Laar et al., 2007; Van Laar et al., 2009 |
| Amyloidosis | Mic60 & Mic19 sequestered into amyloid fibrils | Cellular model system | Olzscha et al., 2011 |
| Cancer | Mic60 and Mic25 levels decreased in response to anticancer therapy | Cellular model system | Magi et al., 2004; An et al., 2012 |
| Diabetic cardiomyopathy | Mic60 levels decreased and Mic27 levels increased | Animal model system | Baseler et al., 2011 |

**Table 2**

| **Phospholipids** | **Mammalian Mitochondria Lipid composition (%)** | |
|---|---|---|
| | **Inner membrane** | **Outer membrane** |
| Phosphatidylethanolamine (PE) | 35 | 26 |
| Phosphatidylcholine (PC) | 40 | 50 |
| Cardiolipin (CL) | 18 | 7 |
| Phosphatidylinositol (PI) | 5 | 15 |
| Phosphatidylserine (PS) | <1 | <1 |
| Phosphatidic acid (PA) | 1 | <1 |
| Phosphatidylglycerol (PG) | <1 | <1 |

**References**


1. Scheffler, I. (2008) Mitochondria, 2nd ed., Wiley-Liss

2. Benard, G. & Rossignol, R. Ultrastructure of the mitochondrion and its bearing on function and bioenergetics. *Antioxid. Redox Signal.* **10,** 1313–42 (2008).

3. Rafelski, S. M. Mitochondrial network morphology: building an integrative, geometrical view. *BMC Biol.* **11,** 71 (2013).

4. Pfanner, N. *et al.* Uniform nomenclature for the mitochondrial contact site and cristae organizing system. *J. Cell Biol.* **204,** 1083–1086 (2014).

5. Hoppins, S. *et al*. A mitochondrial-focused genetic interaction map reveals a scaffold like complex required for inner membrane organization in mitochondria. *J. Cell Biol.* 195:323–340 (2011).

6. Von der Malsburg, K. *et al*. Dual role of mitofilin in mitochondrial membrane organization and protein biogenesis. *Dev. Cell.* 21:694–707 (2011).

7. Alkhaja, A.K. *et al.* MINOS1 is a conserved component of mitofilin complexes and required for mitochondrial function and cristae organization. *Mol. Biol. Cell.* 23:247–257. (2012).

8. Harner, M. *et al.* The mitochondrial contact site complex, a determinant of mitochondrial architecture. *EMBO J.* 30:4356–4370. (2011).

9. Arnoult, D. Mitochondrial fragmentation in apoptosis. *Trends Cell Biol.* **17,** 6–12 (2007).

10. Knott, A. B., Perkins, G., Schwarzenbacher, R. & Bossy-Wetzel, E. Mitochondrial fragmentation in neurodegeneration. *Nat. Rev. Neurosci.* **9,** 505–18 (2008).

11. Jayashankar, V. & Rafelski, S. M. Integrating mitochondrial organization and dynamics with cellular architecture. *Curr. Opin. Cell Biol.* **26,** 34–40 (2014).

12. Ma, Z. A. Zhao Z., & Turk J. Mitochondrial Dysfunction and β-Cell Failure in Type 2 Diabetes Mellitus. *Exp. Diab. Res.* **2012**, Article ID 703538 (2012).

13. Baloyannis, S. J. Alterations of Mitochondria and Golgi Apparatus Are Related to Synaptic Pathology in Alzheimer ' s Disease. *Neurodegener. Dis.* (2013). doi:10.5772/56079

14. Chen, H. & Chan, D. C. Mitochondrial dynamics-fusion, fission, movement, and mitophagy in neurodegenerative diseases. *Hum. Mol. Genet.* **18,** R169–76 (2009).

15. Duncan, J. G. Mitochondrial dysfunction in diabetic cardiomyopathy. *Biochim. Biophys. Acta* **1813,** 1351–1359 (2011).

16. Trudeau, K., Molina, A. J. a, Guo, W. & Roy, S. High glucose disrupts mitochondrial morphology in retinal endothelial cells: implications for diabetic retinopathy. *Am. J. Pathol.* **177,** 447–455 (2010).

17. Yang, X., Borg, L. a H. & Eriksson, U. J. Altered mitochondrial morphology of rat embryos in diabetic pregnancy. *Anat. Rec.* **241,** 255–267 (1995).

18. Ravelli, R.B., Kalicharan, R.D., Avramut, M.C., Sjollema, K.A., Pronk, J.W., Dijk F., Koster, A.J., Visser, J.T., Faas, F.G., Giepmans, B.N. Destruction of tissue, cells and organelles in type 1 diabetic rats presented at macromolecular resolution. *Sci Rep.* **3**, 1804 (2013).

19. Weber, T. a *et al.* APOOL is a cardiolipin-binding constituent of the Mitofilin/MINOS protein complex determining cristae morphology in mammalian mitochondria. *PLoS One* **8,** e63683 (2013).

20. Schlame, M., Ren, M. The role of cardiolipin in the structural organization of mitochondrial membranes. *Biochim. Biophys. Acta.* **1788** 2080–2083 (2009).

21. Houtkooper, R. H. & Vaz, F. M. Cardiolipin, the heart of mitochondrial metabolism. *Cell. Mol. Life Sci.* **65,** 2493–2506 (2008).

22. Schlame, M. Cardiolipin synthesis for the assembly of bacterial and mitochondrial membranes. *J. Lipid Res.* **49,** 1607–20 (2008).

23. Shi, Y. Emerging roles of cardiolipin remodeling in mitochondrial dysfunction associated with diabetes, obesity, and cardiovascular diseases. *J. Biomed. Res.* **24,** 6–15 (2010).

24. Chu, C. T. *et al.* Cardiolipin externalization to the outer mitochondrial membrane acts as an elimination signal for mitophagy in neuronal cells. *Nat. Cell Biol.* **15,** 1197–205 (2013).

25. Mileykovskaya, E. & Dowhan, W. Cardiolipin membrane domains in prokaryotes and eukaryotes. *Biochim. Biophys. Acta* **1788,** 2084–91 (2009).

26. Renner, L. D. & Weibel, D. B. Cardiolipin microdomains localize to negatively curved regions of Escherichia coli membranes. *Proc. Natl. Acad. Sci. U. S. A.* **108,** 6264–9 (2011).

27. Huang, K. C., Mukhopadhyay, R. & Wingreen, N. S. A curvature-mediated mechanism for localization of lipids to bacterial poles. *PLoS Comput. Biol.* **2,** e151 (2006).

28. Mukhopadhyay, R., Huang, K. C. & Wingreen, N. S. Lipid localization in bacterial cells through curvature-mediated microphase separation. *Biophys. J.* **95,** 1034–49 (2008).

29. Gaffaney J.D., Dunning F.M., Wang Z., Hui E., Chapman E.R. (2008) Synaptotagmin C2B domain regulates $Ca^{2+}$-triggered fusion in vitro: critical residues revealed by scanning alanine mutagenesis. *J Biol Chem* **283**:31763–31775.

30. Freyer, M.W. & Lewis, E.A. Isothermal titration calorimetry: experimental design, data analysis, and probing macromolecule/ligand binding and kinetic interactions. *Methods Cell Biol* 84, 79-113 (2008).

31. Loson O.C., Song Z., Chen H., Chan D.C. (2013). Fis1, Mff, MiD49, and MiD51 mediate Drp1 recruitment in mitochondrial fission. Mol Biol Cell 24, 659–667.

32. Montessuit, S. *et al*. Membrane remodeling induced by the dynamin-related protein Drp1 stimulates Bax oligomerization. *Cell*, *142*(6), 889-901 (2010).

33. Rust, M. J., Bates, M. & Zhuang, X. imaging by stochastic optical reconstruction microscopy (STORM). *Nat. Methods* **3,** 793–795 (2006).